

1-1-2012

Flexural Behaviour Of ECC Coupling Slab In Coupled Shear Wall Structure

Rizwan A. Issani
Ryerson University

Follow this and additional works at: <http://digitalcommons.ryerson.ca/dissertations>



Part of the [Civil Engineering Commons](#)

Recommended Citation

Issani, Rizwan A., "Flexural Behaviour Of ECC Coupling Slab In Coupled Shear Wall Structure" (2012). *Theses and dissertations*. Paper 1432.

This Thesis is brought to you for free and open access by Digital Commons @ Ryerson. It has been accepted for inclusion in Theses and dissertations by an authorized administrator of Digital Commons @ Ryerson. For more information, please contact bcameron@ryerson.ca.

FLEXURAL BEHAVIOUR OF ECC COUPLING SLAB IN COUPLED SHEAR WALL STRUCTURE

by

Rizwan Ahmed Issani

B.E. (Civil Engineering)

Mehran University of Engineering & Technology, Jamshoro, Pakistan

A Thesis

Presented to Ryerson University

in partial fulfillment of the

requirements for the

Degree of Master of Applied Science

in the Program of

Civil Engineering

Toronto, Ontario, Canada, 2012

© Rizwan Issani, 2012

Author's Declaration

I hereby declare that I am the sole author of this thesis.

I authorize Ryerson University to lend this thesis to other institutions of individuals for the purpose of scholarly research.

Authors' Signature _____

Date _____

I further authorize Ryerson University to reproduce this thesis by photocopying or by other means, in total or in part, at the request of other institutions or individuals for the purpose of scholarly research.

Authors' Signature _____

Date _____

Acknowledgements

I would like to express my sincere gratitude to my supervisor Dr. Khandaker M. Anwar Hossain, without whom this research could not be accomplished. His persistent support, encouragement and valuable suggestions have guided me through all the steps from the beginning to completion of my graduate study. My knowledge on the specialized subject of the research study has enhanced significantly from his vast experience, and sophisticated understanding for which I am deeply indebted to him. His countless proof readings, corrections and support made this document possible.

I would like to thank Mr. Nidal Jaalouk, Mr. Min Yao and Mr. Mohammad Aldardari and all other lab staffs who assisted me in fabrication and performing physical tests in the Structures and Concrete Labs. Their assistance and brilliant ideas made it possible to carry out successfully the complex experimental tests.

Thanks are extended to the Research Assistants of the Civil Engineering Department notably, Muhammed Anwar, Mahmoud Al-Fayez and Muaawia Janoudy for their great help in casting and testing of model specimens. I also acknowledge the support of my colleagues Faisal Siddiqui, Antonio Toramina, M. Sherir, M. Mavani and Md. Kayes for their assistance.

I would like to acknowledge the financial support from the National Science and Engineering Research Council (NSERC) of Canada. I also like to thank industrial partners for providing concrete materials.

I also extend my special thanks to examining committee members: Dr. Khaled Sennah and Dr. Ahmed Shaker.

Finally, I am deeply and forever indebted to my parents, my wife and my children for their love, encouragement and supports throughout my entire life.

Abstract

FLEXURAL BEHAVIOUR OF ECC COUPLING SLAB IN COUPLED SHEAR WALL STRUCTURE

Rizwan Ahmed Issani, B.E. Engineering

A thesis presented to Ryerson University in partial fulfillment of the requirements for the degree of
Master of Applied Science in the program of Civil Engineering

Toronto, Ontario, Canada, 2012

© Rizwan Ahmed Issani, 2012

Flexural stiffness or effective width of floor slab acting as coupling beam is very important for the analysis of Coupled Shear Wall (CSW) systems. New generation of high performance concretes provide an alternative to conventional concrete to enhance the performance of coupling slabs. This research investigates the flexural behaviour of coupling slabs incorporating Engineered Cementitious Composite (ECC) compared to conventional Self-Consolidating Concrete (SCC). The high strain capacity and low crack width makes ECC an ideal material for coupling slab. Non-linear coupling action of ECC slabs is investigated experimentally with small-scale models having variable geometric parameters under monotonic loading. The performance is judged based on moment-rotation response, flexural stiffness/effective width, deflection, cracking, strain development and failure modes. Design charts for flexural stiffness/effective width of coupling slabs are presented in pre-cracking/cracking/post-yielding stages. CSW systems with ECC are found stronger and ductile than their SCC counterparts confirming the viability of constructing such structures.

Table of Contents

Author's Declaration	ii
Acknowledgements	iii
Abstract	iv
Table of Contents.....	v
List of Figures	ix
List of Tables	xii
List of Notation	xiii
Abbreviations and Units	xvi

CHAPTER 1

INTRODUCTION

1.0 General.....	1
1.1 Significance of the Research	4
1.2 Objectives of the Research	5
1.3 Scope of the Research.....	6
1.4 Thesis Outline.....	7

CHAPTER 2

LITERATURE REVIEW

2.0 General.....	9
2.1 Behaviour of Slabs in Coupled Shear Wall Structures.....	9
2.1.1 Bending or Flexural Stiffness of Coupling Slab in Shear Wall Structure	11
2.1.2 Effective Width of the Coupling Slab	14
2.2 Non-linear Analysis of Reinforced Concrete Coupled Shear Wall Structures.....	15
2.3 Cracking and Failure of Coupling Slabs in Shear Wall Structures	19

2.4 Modes of Failure of Coupled Shear Wall Structure	20
2.5 Analysis of Coupled Shear Wall Structures	22
2.5.1 Continuous Medium Method.....	25
2.5.1.1 Analysis for Uniformly Distributed Load	25
2.5.1.2 Analysis for Distributed, Triangular and Point Loading	33
2.5.1.3 Analysis of Shear Walls with Multiple Bay of Opening	38
2.5.1.4 Physical Interpretation of Design Parameters	41
2.6 Role of Reinforced Concrete in the Coupled Shear Wall Structures	43
2.6.1 Self-Consolidating Concrete (SCC)	44
2.6.2 Engineered Cementitious Composites (ECC)	45
2.6.2.1 Applications of ECC.....	49
2.7 Summary and Conclusion.....	52

CHAPTER 3

EXPERIMENTAL SETUP, MODEL PROPERTIES, INSTRUMENTATION AND TESTING

3.0 Introduction	53
3.1 Simulation of Non-linear Flexural Behaviour of Coupling Slab and Working Principle of Test Set-up.....	53
3.2 Geometry of Model Test Specimens	55
3.3 Material Properties and HPC Mix Design.....	57
3.3.1 Tests on Mechanical Properties of Concrete	57
3.3.1.1 Compressive Strength.....	57
3.3.1.2 Flexural Strength	58
3.3.2 Modulus of elasticity of ECC and SCC.....	59
3.3.3 Reinforcing Steel Properties	61
3.3.4 HPC Mix Design	63

3.3.4.1 Self-Consolidating Concrete (SCC)	63
3.3.4.2 Engineered Cementitious Composite (ECC)	65
3.4 Design of Reinforcement for Models and Reinforcement Details	66
3.5 Analytical Moment and Shear Capacities of Coupling Slabs in Model Specimens	69
3.6 Casting of Model Specimens	71
3.7 Experimental Set-up, Instrumentation and Testing	72
3.8 Chapter Summary	77

CHAPTER 4

ANALYSES OF EXPERIMENTAL RESULTS

4.0 Introduction	78
4.1 Experimental Results	78
4.1.1 Behaviour of Reinforcement in Slab based on Strain Development	78
4.1.2 Strain Development in Concrete and Proof of Theory	80
4.1.3 Load-Displacement Response, Crack Development and Failure Modes	84
4.1.3.1 Models with L/X of 0.3 (ECC350 and SCC350).....	84
4.1.3.2 Models with L/X of 0.4 (SCC300 and ECC300).....	87
4.1.3.3 Models with L/X of 0.6 (ECC200 and SCC200).....	88
4.2 Comparison of Experimental and Theoretical Load Capacity	91
4.3 Chapter Conclusions	93

CHAPTER 5

BENDING STIFFNESS AND EFFECTIVE WIDTH OF COUPLING SLAB

5.0 Introduction	94
5.1 Determination of Bending Stiffness and Effective Width of Coupling Slab.....	94
5.1.1 Calculation of Bending Stiffness and Effective Width.....	95

5.2 Design Curves for Effective Width and Bending Stiffness	101
5.3 Relationship Between Bending Stiffness in Various Stages	106
5.4 Comparison of Bending Stiffness and Effective Width	107
5.4.1 Comparison Pre-cracking Stiffness/Effective Width and Effect of Concrete Types	107
5.4.2 Comparison Cracking (k_o)/Post-yielding (k_p) and Effect of Concrete Types	109
5.5 Chapter Summary	110

CHAPTER 6

ANALYSIS OF COUPLED SHEAR WALL BUILDING IN PRE-CRACKING, CRACKING AND POST-YIELDING STAGES BY CONTINUOUS MEDIUM METHOD

6.0 General.....	111
6.1 Full-scale Prototype 20-storey Coupled Shear Wall Building with Geometric Dimensions and other Specifications	111
6.2 Load, Stress and Deflection Analysis of 20-Storey Building.....	113
6.2.1 Stresses in Shear Walls.....	113
6.2.2 Moments in Shear Walls.....	115
6.2.3 Shear Flow Development	117
6.2.4 Lateral Deflection of the Building.....	119
6.3 Wind Load and Deflection Capacity Analyses of Yielded Coupled Shear Wall Building	121
6.4 Chapter Conclusion	125

CHAPTER 7

CONCLUSIONS

7.0 Introduction	126
7.1 Conclusions	127
7.2 Recommendations for Future Research.....	128

REFERENCES	129
-------------------------	------------

List of Figures

Figure 1.1: (a) Schematic view with structural components (b) layout plan of coupled shear wall structure (Hossain 2003).....	1
Figure 1.2: (a) Building forced under lateral load (b) Structural action due to shear forces (Hossain 2003)	2
Figure 1.3: Rotation caused by bending due to vertical deflection (Hossain 2003).....	3
Figure 2.1: Isometric view of coupled shear wall storey panel	10
Figure 2.2: The reaction of coupled shear wall under lateral loading	11
Figure 2.3: The reaction of coupled shear wall under simulated vertical loading	12
Figure 2.4: The plan of finite element model of slab (Coull and Wong 1983).....	17
Figure 2.5: The plan of different T and L shaped coupled flanged shear wall system	17
Figure 2.6 Crack pattern and failure of coupling slabs (Hossain 2003)	20
Figure 2.7: Failure modes of coupled shear wall under lateral load (Subedi 1991).....	21
Figure 2.8: (a) Coupled shear wall with equivalent continuous of laminae under lateral loadings (b) Coupled shear wall showing laminar shear flow and (c) Showing laminar shear force and moments (Hossain 2003)	24
Figure 2.9: Plan of walls with stress distribution (Coull and Choudhury 1967a).....	28
Figure 2.10: Variation of K_2 with x/H (Coull and Choudhury 1967a)	30
Figure 2.11: Variation of K_3 with the αH and x/H (Coull and Choudhury 1967a)	31
Figure 2.12: Curves showing the variation of K_4 with the αH and μ (Coull and Choudhury 1967a)	32
Figure 2.13: Coupled shear wall under uniform loading, triangular and point loading.....	33
Figure 2.14: Curves showing the variation of K_1 and K_2 for point load at the top.....	36
Figure 2.15: Curves showing the variation of K_1 and K_2 for triangularly distributed load	36
Figure 2.16: Curves showing the variation of deflection factor K_4 for point load at top and triangular loading (Coull and Choudhury 1967b).....	38
Figure 2.17: Building with Shear wall with two band openings	39
Figure 2.18: Coefficient of maximum shear force K_1 for uniformly distributed load	40
Figure 2.19: Coefficient of maximum shear force K_1 for uniformly distributed load	41
Figure 2.20: Extreme flexure capabilities of ECC under a large bending load (Li 2011)	46
Figure 2.21: Typical tensile stress-strain curve and crack width development of ECC	47
Figure 2.22: Left Overview of Mihara Bridge (Mitamura et al. 2005) and right labour repairing Mitaka Dam with ECC for water-proofing (Kojima et al. 2004).....	49
Figure 2.23: Surface preparation with high-pressure water jet repair of concrete retaining wall .	50
Figure 2.24: (a) The Nabeaure Tower in Yokohoma, Japan building with pre-cast coupling beams and (b) Schematics view showing coupling beams (in yellow) on each floor (Maruta et al. 2005).....	51

<i>Figure 3.1: Working principle of test-set-up and behaviour of coupling slab</i>	<i>54</i>
<i>Figure 3.2: Isometric view of coupled shear wall, showing geometric parameters</i>	<i>55</i>
<i>Figure 3.3: Three different assemblies showing geometric parameter</i>	<i>56</i>
<i>Figure 3.4: The result of the first test for the modulus of elasticity (Average $E = 24,500$ MPa)</i>	<i>59</i>
<i>Figure 3.5: The result of the second test for the modulus of elasticity (Average $E=24,980$ MPa)..</i>	<i>60</i>
<i>Figure 3.6: Tensile test results of steel bar # 3941</i>	<i>61</i>
<i>Figure 3.7: Tensile test results of steel bar # 3939</i>	<i>62</i>
<i>Figure 3.8: Mixing the SCC ingredients; (a) Slag and cement (b) Sand and coarse aggregate</i>	<i>64</i>
<i>Figure 3.9: Making ECC</i>	<i>66</i>
<i>Figure 3.10: Reinforcements in the slab</i>	<i>67</i>
<i>Figure 3.11: Reinforcements in the 300 mm wide types of Walls</i>	<i>68</i>
<i>Figure 3.12: Rectangular stress block of rectangular slab.....</i>	<i>69</i>
<i>Figure 3.13: Formwork/mould ready with steel reinforcements for casting CSW model specimens</i>	<i>71</i>
<i>Figure 3.14: Casting of highly flowable ECC mixture into the mould.....</i>	<i>71</i>
<i>Figure 3.15: (a) Front view (b) Side-View of experimental setup.....</i>	<i>73</i>
<i>Figure 3.16: Laboratory test setup (instrumentation).....</i>	<i>74</i>
<i>Figure 3.17: Laboratory test setup (supports)</i>	<i>75</i>
<i>Figure 3.18: Laboratory test setup exhibiting desired deformed behaviour of coupled shear wall</i>	<i>76</i>
 <i>Figure 4.1: Locations of strain gauges at slab reinforcements.....</i>	 <i>79</i>
<i>Figure 4.2: Load-strain relationship of reinforcements in the slab of SCC300.....</i>	<i>80</i>
<i>Figure 4.3: Placement of strain gauges in concrete.....</i>	<i>81</i>
<i>Figure 4.4: Diagram showing the locations of strain gauges.....</i>	<i>81</i>
<i>Figure 4.5: Strain relationship of all 3 strain gauges, showing point of contra-flexure form at the center of ECC300</i>	<i>82</i>
<i>Figure 4.6: Comparison of load-concrete strain relationship of ECC and SCC (L/X 0.4).....</i>	<i>83</i>
<i>Figure 4.7: Experimental load-displacement responses of ECC and SCC specimens (L/X 0.3)</i>	<i>85</i>
<i>Figure 4.8: Crack development and crack propagations in ECC350 specimen at inner edges of the fixed wall</i>	<i>86</i>
<i>Figure 4.9: Crack development and crack propagations in SCC 350 specimen at the inner edges of the wall</i>	<i>86</i>
<i>Figure 4.10: Experimental load-displacement responses of ECC and SCC specimens (L/X 0.4) ...</i>	<i>88</i>
<i>Figure 4.11: Experimental load-displacement responses of ECC and SCC specimens (L/X 0.6) ...</i>	<i>89</i>
<i>Figure 4.12: Shows small crack propagations of ECC200 slab at near inner edges at upper side of the slab on loading side.....</i>	<i>89</i>
 <i>Figure 5.1: Idealized load-displacement and moment rotation cure</i>	 <i>95</i>

Figure 5.2: Idealized load-displacement and moment-rotation curves of ECC and SCC models ...	97
Figure 5.3: Idealized load-displacement and moment-rotation curves of ECC and SCC models ...	97
Figure 5.4: Idealized load-displacement and moment-rotation curves of ECC and SCC models ...	98
Figure 5.5: Comparison of effective width of ECC/ SCC slab at pre-cracking stage as function of L/X	101
Figure 5.6: Comparison of effective width of ECC/ SCC slab at cracking and post-yielding stages as function of L/X	102
Figure 5.7: Comparison of effective width of ECC/SCC slab at pre-cracking stage as function of L/Y	102
Figure 5.8: Comparison of effective width of ECC/ SCC slab at cracking and post-yielding stages as function of L/Y	103
Figure 5.9: Comparison of flexural stiffness at pre-cracking stage (Y/X 0.6)	104
Figure 5.10: Comparison of flexural stiffness at pre-cracking stage ($Y/X=0.6$)	104
Figure 5.11: Bending stiffness and effective width of ECC coupling slab compared with SCC	105
Figure 5.12: Relationship between k_o , k_{cr} and k_p in ECC and SCC specimens	106
Figure 5.13: Comparison of pre-cracking stiffness of coupling slabs with normal concrete, ECC and SCC.....	108
Figure 5.14: Comparison of pre-cracking effective width for different concrete types	108
Figure 5.15: Comparison of cracking and post-yielding stiffness and effect of concrete types.....	109
Figure 6.1: (a) Side view of the 20 storey building with uniformly distributed static wind load (b) Cross-section floor plan of the building	112
Figure 6.2: Stresses at inner edges of the shear walls at each storey (ECC, $L/X = 0.3$).....	114
Figure 6.3: Stresses at inner edges of the shear walls at each storey (SCC, $L/X = 0.3$)	115
Figure 6.4: Moment developed at walls 1 and 2 at each storey (ECC: $L/X = 0.3$)	116
Figure 6.5: Moment developed at walls 1 and 2 at each storey (SCC: $L/X = 0.3$).....	116
Figure 6.6: Laminar shear flow (q) at each storey (ECC: $L/X = 0.3$)	117
Figure 6.7: Laminar shear flow at each storey (SCC: $L/X = 0.3$)	118
Figure 6.8: Comparison of shear flow at each storey for ECC and SCC ($L/X = 0.3$)	118
Figure 6.9: Lateral deflection along the height of building at each stage (ECC: $L/X= 0.3$).....	119
Figure 6.10: Lateral deflection along the height of building at each stage (SCC: $L/X= 0.3$)	120
Figure 6.11: Post-yielding lateral deflection of ECC and SCC building with different L/X	121
Figure 6.12: Required wind load for yielding and the top deflection at yielding	123
Figure 6.13: Comparative performance of ECC and SCC building in terms of load and deflection capacity	124
Figure 6.14: Deflection of buildings under calculated design wind load by different L/X	124

List of Tables

<i>Table 2.1: Variation of parameter αH for shear wall structure (Coull and Choudhury 1967b)</i>	43
<i>Table 2.2: Engineered cementitious composite typical mix design proportions (Nawy 2008)</i>	48
<i>Table 2.3: Material charging sequence into ready-mix trucks (Nawy 2008).....</i>	48
<i>Table 3.1: Geometrical parameters of model test specimens.....</i>	57
<i>Table 3.2: Type and strength of concrete for each specimen (28 days).....</i>	58
<i>Table 3.5: Modulus of elasticity (E) for the ECC and SCC</i>	60
<i>Table 3.6: Table showing results of tensile test of steel bars</i>	62
<i>Table 3.5: Mixture proportions of SCC.....</i>	63
<i>Table 3.6: Mixture properties of ECC.....</i>	65
<i>Table 3.7: Analytical moment and shear load resistance of coupling slab.....</i>	70
<i>Table 4.1: Load and concrete tensile strain in cracking, yielding and ultimate stages</i>	84
<i>Table 4.2: Summary of test results from load-displacement response and also ductility values of all CSW model specimens.....</i>	91
<i>Table 4.3: Comparison of experimental and theoretical load capacity of coupling slab</i>	92
<i>Table 5.1: Multiplication factors.....</i>	96
<i>Table 5.2: Bending stiffness in pre-cracking, cracking and post-yielding stages</i>	99
<i>Table 5.3: Summary of geometric parameters, bending stiffness and effective width</i>	100
<i>Table 6.1: Geometrical parameters of full-scale prototype coupled shear wall building</i>	113
<i>Table 6.2: Geometrical parameters and results of wind load capacity & deflection at yielded point</i>	122

List of Notation

x	=	Distance measured from top of the building
y	=	Deflection of the building
H	=	Total Height of the building
h	=	Storey height
l	=	Distance between centroidal axis of walls
b or L	=	Clear distance between walls (opening for corridor)
W	=	Width of wall
X	=	Length of slab
A_1, A_2	=	Area of walls
A_s	=	Area of steel
t	=	Thickness of the slab
t_w	=	Thickness of walls
I_1, I_2	=	Moment of inertia of walls
I_p	=	Moment of inertia of a connecting beam or slab
I_b	=	Second moment of inertia of a connecting beam or slab
I'	=	Moment of inertia of composite cantilever
Y_e	=	Effective width of slab
Y_{eo}	=	Effective width of slab in pre-cracking
Y_{ecr}	=	Effective width of slab in cracking
Y_{ep}	=	Effective width of slab in post-yielding
Y	=	Actual width of slab
D	=	Flexural rigidity of the slab

ν	=	Poisson's ratio of material
Q or V	=	Storey shear force
M	=	Bending moment
w	=	Maximum intensity of triangular or uniformly distributed load
w_o	=	Maximum wind load intensity in pre-cracking
w_{cr}	=	Maximum wind load intensity in cracking
w_p	=	Maximum wind load intensity in post-yielding
p	=	Point load
T	=	Integral shear force in connecting medium
M_0	=	Total moment
M_1, M_2	=	Bending moment in walls
M_r	=	Resisting moment
M_f	=	Factored moment
q	=	Shear flow or shear force intensity per unit length in connecting medium
K_1, K_2	=	Wall bending stress factors
K_3	=	Connecting beam stress factors
K_4	=	Deflection factors
k_δ	=	Translational stiffness factor
k	=	Rotational stiffness factor
k_o	=	Rotational bending stiffness factor in pre-cracking
k_{cr}	=	Rotational bending stiffness factor in cracking
k_p	=	Rotational bending stiffness factor in post-yielding
μ, β & α	=	Design parameters
δ	=	Deflection of walls

$\sigma_A, \sigma_B, \sigma_C, \sigma_D$	=	Stresses in the walls at different points
θ	=	Angle of deflection of walls or rotation of the walls
E	=	Modulus of elasticity of material used
E _c	=	Modulus of elasticity of Concrete
E _s	=	Modulus of Elasticity of Steel
f_r	=	Flexural resistance of beam or flexural strength (Modulus of Rupture)
f_c'	=	Compressive strength of concrete
f_{cu}	=	Cubical Compressive strength of Concrete
f_y	=	Yield strength of steel
Ψ	=	Relative ductility

Abbreviations and Units

AEA	=	Air-Entraining Admixture
CSW	=	Coupled Shear Wall
FA	=	Fly Ash
FEM	=	Finite Element Modeling
HRWRA	=	High Range Water reducing Agent/Admixture
PVA	=	Poly-Vinyl Alcohol
HPC	=	High Performance Concrete
W/cm, W/C	=	Water Cement Ratio
kN	=	kilo Newton
LVDT	=	Linear Variable Displacement Transducer
MPa	=	Mega Pascal
GPa	=	Gega Pascal
m	=	Meters
mm	=	Millimeters
μm	=	Micro-meter
FRC	=	Fiber Reinforced Concrete
R/ECC	=	Reinforced Engineered Cementitious Composite
RCC	=	Reinforced Cement Concrete
R/SCC	=	Reinforced Self Consolidated Concrete
NC	=	Normal Concrete
SP	=	Super Plasticizer

CHAPTER 1

INTRODUCTION

1.0 General

In any multi-story building, an efficient structural system should resist lateral forces due to wind, earthquake and must prevent excessive deflections. Coupled Shear Wall (CSW) system is a popular form of high rise structure and is suitable for 20 to 30 stories. In this system, generally two or more walls in the same plane are connected at the floor levels by means of stiff slabs. Fig. 1.1(a) shows a perspective view of CSW system with two walls and coupling floor slab. Fig. 1.1(b) shows a typical floor plan of CSW building.

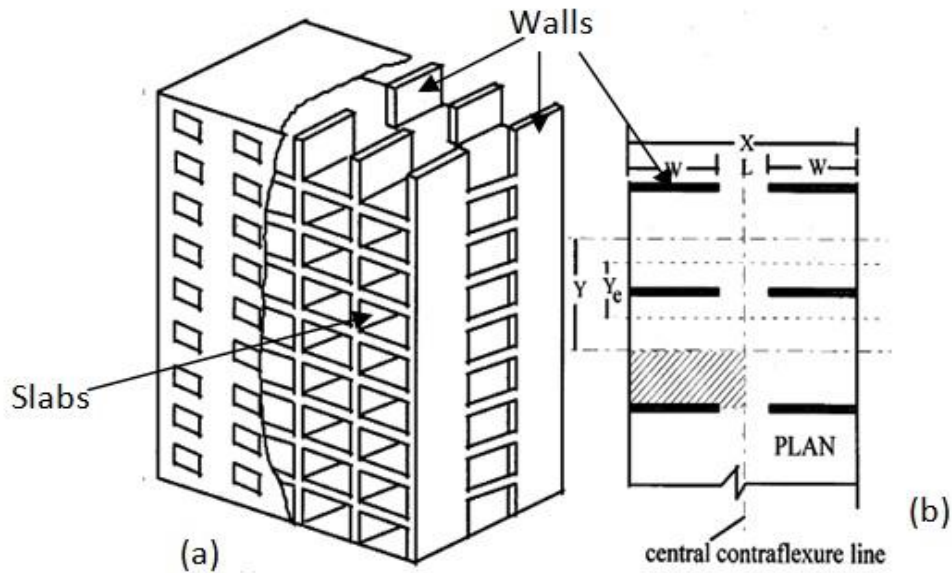


Figure 1.1: (a) Schematic view with structural components (b) layout plan of coupled shear wall structure (Hossain 2003)

The special features of this type of building are that the two rows of apartments are connected by a common corridor and the partition walls are treated as shear walls. As no projecting

system of beams run across the corridor, there is no need for false ceilings and the height of the building is appreciably reduced thus accommodating more floors in the same height of the building. In the plan view of coupled shear wall (Fig. 1.1b), the two walls of width (W) having a corridor opening of width (L) between them are placed symmetrically along the width of the building (X). The centre to centre distance between rows of shear walls are denoted by (Y).

Coupled shear wall resists lateral loads by cantilever bending action, which results in rotation (Θ) of the wall cross-sections (Fig. 1.2a). The free bending of a pair of shear wall is resisted by the floor slabs, which are forced to rotate and bend out of plane where they are connected rigidly to the walls. Due to large width of the wall, considerable differential shearing action is imposed on the connecting slab, which develops transverse reactions to resist the wall deformations and induces axial tensile and compressive forces (V or Q) into the walls (Fig. 1.2b). Due to large lever arm involved, relatively small axial forces can give rise to substantial moment of resistance (M), thereby reducing greatly the wind moments in the walls. Therefore, the lateral stiffness of the structure is increased.

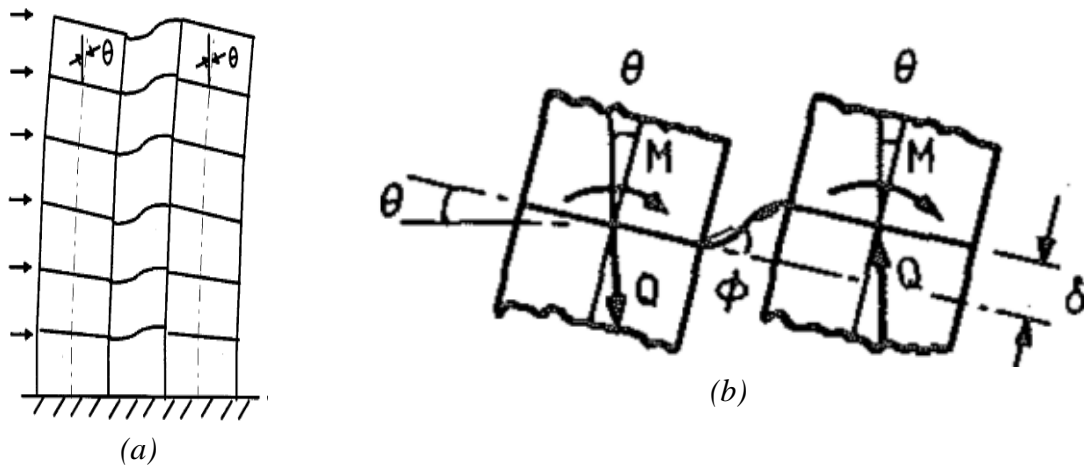


Figure 1.2: (a) Building forced under lateral load (b) Structural action due to shear forces
(Hossain 2003)

Similarly, the bending of the coupling slab can also be caused by vertical deformation (δ) due to seismic reaction and foundation settlement of the structure as described in Fig. 1.3 resulting in moment (M), rotation (Θ) and axial tensile/compressive forces (V or Q) into the walls.

Analysis of coupled shear wall structures can be performed using existing techniques if the bending stiffness and effective width of coupling slab is known (Rossman 1964; Hossain 2003). The width of the slab plays a very effective role in strength and stiffness of the coupled shear wall system. The width of the floor slab actively resisting wall moment as a connecting beam under lateral loading is known as effective width (Y_e) as shown in as shown in Fig. 1.1b. Previous research studies concentrated on finding the stiffness and effective width of coupling slab (Hossain 2003; Coull and Wong 1981, 1983, 1984, 1990; Qadeer and Smith 1969; Bari 1987; Barnard and Schwaighofer 1967; Tso and Mahmoud 1977; Coull and El-Hag 1975).

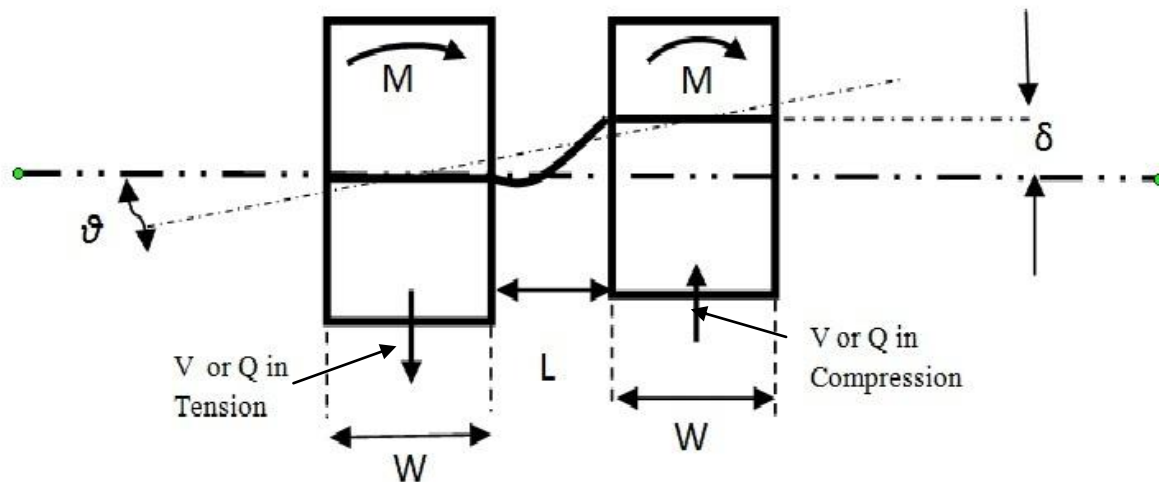


Figure 1.3: Rotation caused by bending due to vertical deflection (Hossain 2003)

Most of the previous research studies concentrated on the linear behaviour of reinforced concrete (RC) coupling slabs and developed equations and design aids for prediction of bending stiffness and effective width. RC is a non-linear material and the flexural stiffness and effective width of floor slabs will be affected by concrete cracking and yielding of steel. Very few studies, however, concentrated on the flexural behaviour of coupling slab considering non-linear behaviour of RC and predicted stiffness and effective width of coupling slab in pre-cracking, cracking and post-yielding stages (Hossain 2003).

Over the last few years new generation of high performance concrete (HPC) such as Self-Consolidating Concrete (SCC) and Engineered Cementitious Composites (ECC) with improved strength, durability, ductility and energy absorbing capacity has been developed. SCC is very flowable, achieves good consolidation, and can flow into place between congested reinforcement without vibration and without defects due to bleeding or segregation (Khayat 1999; Hossain and Lachemi 2010).

Self-consolidating ECC was reported to have superior workability, ductility and durability, which translates to speedy construction, reduced maintenance and a longer life span for the structure (Li and Kanda 1998; Wang et al. 2006; Şahmaran et al. 2009). Micromechanical design allows optimization of ECC for high performance, resulting in extreme tensile strain capacity while minimizing the amount of reinforcing fibres, typically less than 2% by volume. Unlike ordinary cement-based materials, ECC strain hardens after first cracking and demonstrates a strain capacity 300 to 500 times greater than normal concrete through the use of incorporating fibers. Even at large imposed deformation, crack widths of ECC remain small, less than 60 μm .

The use of HPCs in Coupled Shear Wall (CSW) system can significantly improve the performance in construction and service stages. Self-consolidation properties of SCC and ECC will help pour concrete with ease without consolidation into the heavily reinforced walls and slab components and ensure concrete quality. The knowledge of the behaviour of CSW systems incorporating new generation of HPCs is very important for implementation of this new HPC technology to construct high rise buildings.

1.1 Significance of the Research

For decades, comprehensive research has been conducted on the ordinary reinforced concrete based CSW system. To the author's knowledge, no research has been conducted on coupled shear wall system with Reinforced Engineered Cementitious Composites (R/ECC) to date. The innovative technology of R/ECC based CSW system can significantly improve the performance in terms of strength, stiffness, ductility, energy absorbing capacity and durability. Design specifications are also not available in current Codes and existing analysis techniques to accommodate the high strain hardening capacity of ECC and its effect on stresses and deflection characteristics of CSW system.

The findings and recommendations of this research will surely be beneficial for engineers, builders and local authorities engaged in designing/constructing innovative high performance shear wall buildings using ECC technology.

1.2 Objectives of the Research

The main objective of the research is to study the bending/flexural performance of ECC coupling slabs in the shear wall structures by testing small scale model specimens having varying geometric parameters under monotonic loading through experimental and analytical investigations. It is expected that the application of ECC will greatly enhance the strength, stiffness and ductility of the CSW system. The secondary objectives include:

- The performance study of ECC coupling slab compared with the conventional concrete (SCC) counterpart based on load deflection response, moment-rotation response, flexural stiffness, ductility enhancement, cracking pattern, and failure modes.
- The study of the strength, stiffness and ductility of the overall system as well as bending stiffness/ effective width of coupling slab based on experimental behaviour.
- The development of design aids/guidelines CSW system with ECC coupling for use in practical applications. Formulation of design charts for the determination of flexural stiffness and effective width of coupling slab are presented as functions of geometric parameters in pre-cracking, cracking and post-yielding stages of non-linear material response based on experimental and theoretical analyses. Such design charts can be used in the analysis and design of coupled shear wall structures with ECC floor slabs in practical construction.
- The implementation of bending stiffness and effective width of coupling slabs to analyze the strength, stress, deflection, force distribution and wind load resistance of CSW system using commonly used Continuous Medium Approach (Coull and Choudhury 1967a, 1967b; Hossain 2003).

1.3 Scope of the Research

Coupled shear walls provide lateral rigidity to the structure due to the coupling slab and for analysis of any CSW system, the non-linear flexural behaviour of slab must be known. Flexural stiffness of slabs can be derived as a function of geometric parameters such as L/X , Y/X and L/Y as well as material parameters in the pre-cracking, cracking and post-yielding stages of the CSW system.

Six small-scale one story models of approximately $1/12^{\text{th}}$ scale of the CSW prototype having four different L/X (with constant Y/X) made of reinforced SCC (R/SCC) and ECC (R/ECC) (three models for each type) were tested under monotonic loading simulating the actual lateral behaviour of the system. The heavily instrumented model tests have provided information on strength, stiffness, load-displacement response, moment-rotation response, cracking/crack patterns, stress-strain characteristics and failure modes of the system. The scope of the research can be summarized as follows:

- Carryout a comprehensive literature review on coupled shear wall systems and high performance concrete.
- Design and construct a test set-up for model tests to carryout testing simulating actual non-linear behaviour of CSW system under lateral load.
- Perform small-scale model tests on CSW systems made of R/ECC and R/SCC to obtain comprehensive information on strength, stiffness, stress-strain characteristics, failure modes and ductility of the system. Compare the results of both types of concrete (SCC and ECC) and investigate the possible advantages of using ECC versus SCC.
- Analyze experimental data to compare the performance of ECC based coupling slabs compared to their SCC counterparts based on strength, stiffness, ductility and failure modes. Compare experimental strength and theoretical strength of the coupling slabs derived from Code based approach.
- Derive flexural stiffness and effective width of coupling slabs in pre-cracking, cracking and post yielding stages of the CSW systems based on experimental and theoretical analyses. Compare performance of ECC and SCC coupling slabs in terms of flexural

stiffness and effective width as well as study the effect of geometric parameters. Compare and validate the results with those of previous research studies.

- Develop design charts for flexural stiffness and effective width of coupling slab in pre-cracking, cracking and post-yielding stages of CSW systems as function of geometric parameters based on experimental and analytical studies.
- Analyze prototype full-scale ECC/SCC CSW buildings using continuous medium method to study the influence of variable effective width at various stages of loading (pre-cracking, cracking, post-yielding) on stress, deflection and other aspects such as development of shear flow and wind load resistance of CSW systems.
- Derive conclusions and make recommendations for future research studies on ECC coupled shear wall structures.

1.4 Thesis Outline

This thesis comprises of seven main chapters. Chapter 1 provides the motivation behind the need for this research and summarizes research significance, objectives and scope.

Chapter 2 provides a comprehensive literature review on behaviour and analysis of coupled shear wall systems under various loading. It also includes a review of high performance concrete concentrating on SCC and ECC illustrating some practical applications. Review conclusion also justifies the need for current research.

Chapter 3 describes the development of test set-up and its working principle, instrumentation, test procedures, steel and SCC/ECC properties, details of models including geometric dimensions, design procedures and reinforcement details. It also describes the specimen preparation process including formwork, concrete making/casting and specimen curing as well as control specimens.

Chapter 4 provides an analysis and discussion of test results based on load-deflection response, strain development in concrete and steel reinforcement and failure modes. The influence on geometric parameters and concrete types (SCC or ECC) is also presented based on strength, ductility and energy absorbing capacity.

Chapter 5 presents calculation of bending stiffness and effective of coupling slabs from model tests using theoretical models. Design charts for bending stiffness and effective width of coupling slabs in pre-cracking, cracking and post-yielding stages are presented and compared with previous research studies. The influence of geometric parameters and concrete types (ECC and SCC) on bending stiffness and effective width is also critically analyzed.

Chapter 6 presents full-scale analysis of 20-storey ECC/SCC coupled shear wall buildings using continuous medium method illustrating variation of stress/moment in shear walls, laminar shear flow and deflection along the height of the building in pre-cracking, cracking and post-yielding stages of the building. Wind load carrying capacity and ultimate deflection of ECC and SCC full-scale buildings at yielding stage are determined to illustrate superior performance of ECC building in terms of strength and ductility.

Chapter 7 summarizes the conclusions and findings of this research. This chapter also provides directions for future research studies.

CHAPTER 2

LITERATURE REVIEW

2.0 General

In any tall building consisting of Coupled Shear Wall System (CSWS), it is important to analyze the behaviour of the connecting/coupling slab. It is necessary to determine the stresses developed in the slab which is not throughout constant across the width, and the forces interacting at inner edges of the walls. In this chapter, a review of previous research studies on CSWS is provided concentrating on various aspects such as method of analysis under various lateral loads and behaviour of coupling slabs highlighting stress development, modes of failure, bending/flexural stiffness and effective width as well as methods to determine bending stiffness and effective width of coupling slabs. In addition, the properties of high performance of concrete namely Self-Consolidating Concrete (SCC) and Engineered Cementitious Composite (ECC) are described. The potential of using SCC and ECC in CSWS is also described based on structural performance illustrating practical case studies.

2.1 Behaviour of Slabs in Coupled Shear Wall Structures

Analysis of coupled shear wall structures can be performed using existing techniques if the bending stiffness and effective width of coupling slab is known. Previous research studies concentrated on finding the effective width (Y_e) and the bending stiffness of the slab (Choudhury 1968; Coull and Choudhury 1967a,b; Coull and Irwin 1969; Coull and Wong 1981, 1983, 1984; Coull and El-Hag 1975; Huq 1974 and Hossain 2003). A typical storey of a slab coupled shear wall system is shown in Fig. 2.1.

Barnard and Schwaighofer (1967) used Rossman (1964) theory to solve the stresses in slabs connected to shear walls, with assumption to take whole width of the slab as effective width, and validated the results through theoretical analysis and model tests. But after discussion of the same paper, Choudhury (1968) concluded that by taking whole width effective into the account may lead

to some errors in calculation of stresses and also concluded that Rossman's theory cannot be applied to the analysis in general.

Choudhury (1968) tested wall-coupling slab models with asbestos cement and found that only 25% width is effective and validated the results through finite element modeling.

Qadeer and Smith (1969) analyzed slab with finite difference method and validated through experimental results. A set of curves were developed by relating geometric parameters (Fig. 2.1) such as slab width (Y), length of the slab (X), corridor opening width (L) and the effective width (Y_e). It is revealed that the ratios L/X and Y/X have significant effect on the Y_e . By taking this research outcome into account, Michael (1969) presented a single curve for Y_e .

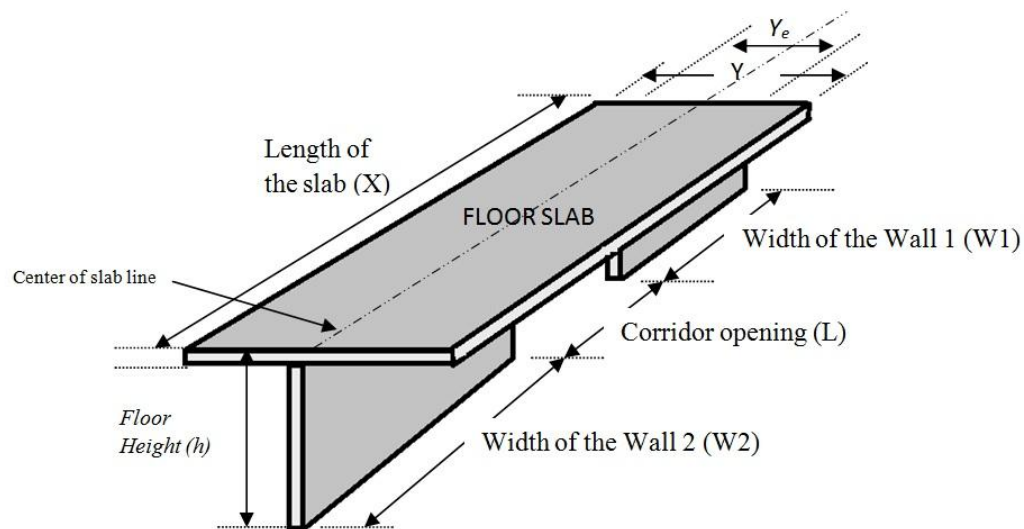


Figure 2.1: Isometric view of coupled shear wall storey panel

Huq (1974) attempted to prepare sets of suitable design curves for effective width of coupling slab in flat plate steel structures. The effective width of the slab was evaluated as a function of corridor opening and it was found that the effective width increases with the increase of L/X . A model specimen made of micro-concrete was tested. It was found that the strain and consequently, the stress across the slab were not consistent under lateral load. It was also concluded that the effective width decreases with the increase of load.

Tso and Mahmoud (1977) used finite element techniques to analyze the stresses with coupled planar, T-section and box core walls to obtain the stiffness of the slab coupled shear wall system. It was noted that the additional stiffening effect from the coupling slab is significant only when the wall opening (corridor width) is small compared with the width of the wall (W).

2.1.1 Bending or Flexural Stiffness of Coupling Slab in Shear Wall Structure

Figs. 2.2 and 2.3 shows the simulated bending behaviour of slab coupled shear wall system subjected to lateral loads (Coull and Wong 1981; Hossain 2003). The resistance against lateral load is simulated by both Figs. Coupled shear wall resists lateral loads due to bending deformation of slabs and rotation (θ) or vertical displacement (δ) of walls that generate resisting moment (M) through tensile/compressive forces (V or Q) in the walls (Fig. 2.2). Moment distribution in the slab is illustrated in Fig. 2.2 through M/EI diagram where E and I represent the modulus of elasticity of the material and second moment of area of the slab, respectively. It is noted that the moment is decreased to zero at the point of contra-flexure in the centre of corridor opening from maximum value at the centre of the wall.

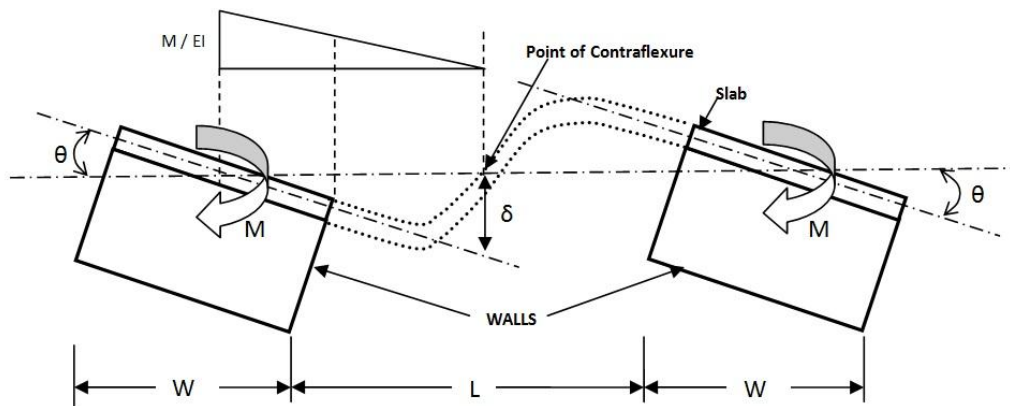


Figure 2.2: The reaction of coupled shear wall under lateral loading

(Coull and Wong 1981; Hossain 2003)

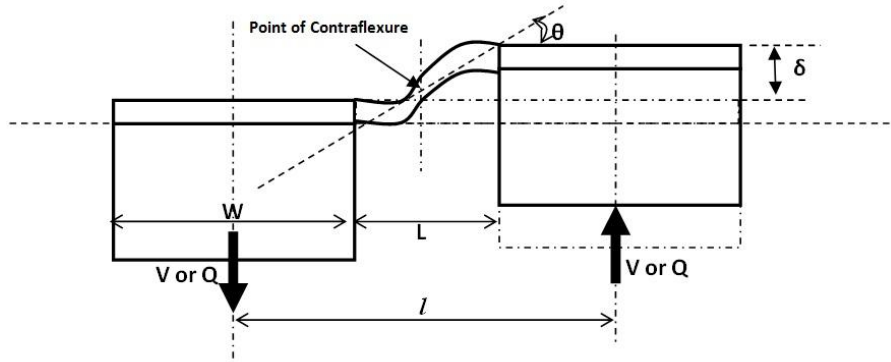


Figure 2.3: The reaction of coupled shear wall under simulated vertical loading

(Coull and Wong 1981; Hossain 2003)

Coull and Wong (1981) and Hossain (2003) analyzed distribution of bending stress across the slab width and $Q-\delta / M-\theta$ response of the system by finite element modeling supported by experimental investigations simulating both Figs. 2.2 and 2.3. Hossain (2003) found that the slab behaviour was similar in both cases in pre-cracking, cracking and post-yielding stages of Reinforced Concrete (RC) coupled shear wall system.

The bending/flexural stiffness of the coupling slab may be defined as a rotational stiffness (M/θ) or as a translational stiffness (Q/δ) as the two are related. For convenience the non-dimensional rotational stiffness factor (k) and translational stiffness factor (k_δ) can be defined as (Hossain 2003 and Coull and Wong 1981):

$$k = \frac{M}{\theta D} \quad (2.1)$$

And,

$$k_\delta = \frac{V L^2}{\delta D} \quad (2.2)$$

Where, D is the flexural rigidity of the slab $\frac{Et^3}{12(1-\nu^2)}$, t is the thickness of slab and ν is the Poisson's ratio for slab material.

From Fig: 2.2,

$$\theta = \frac{\delta}{\left(\frac{L+W}{2}\right)} = \frac{2\delta}{L+W} \quad (2.3a)$$

By taking slab as an equivalent beam section,

$$\delta = \frac{M}{12 EI} \frac{L^3}{L+W} \quad (2.3b)$$

Referring Figs. 2.2 and 2.3, storey shear force = $Q = \frac{M}{L+W}$.

By substituting the value of V or Q in Eq. 2.3b;

$$\frac{\delta}{L^3} \frac{12 EI}{L+W} = \frac{M}{L+W} = V$$

Or;

$$\frac{V}{\delta} = \frac{12 EI}{L^3} \quad (2.4)$$

By using Eq. 2.4 in Eq. 2.2;

$$k_{\delta} = \frac{12 EI}{L^3} \frac{L^2}{D} = \frac{12 EI}{L D} \quad (2.5)$$

And

$$\frac{M}{\theta} = \frac{6 EI (L+W)^2}{L^3} \quad (2.6)$$

By substituting these values in Eq. 2.1, we get;

$$k = \frac{6 EI (L+W)^2}{L^3 D} \quad (2.7)$$

Where, I is the second moment of area of the coupling slab beam expressed as $\frac{Y_e t^3}{12}$,

and t is the thickness of the slab.

2.1.2 Effective Width of the Coupling Slab

The effective width of the coupling slab can be expressed in terms of geometrical and material characteristics of coupled shear wall system as an equivalent beam, by equating Eqs. 2.1 and 2.2 in terms of rotational and translational stiffness as follows (Hossain 2003; Coull and Wong 1981).

For rotational stiffness:

$$\frac{Y_e}{Y} = \frac{k}{6(1 - \nu^2)} \left(\frac{L}{Y} \right) \left(\frac{L}{L + W} \right)^2 \quad (2.8)$$

For translational stiffness:

$$\frac{Y_e}{Y} = \frac{k_\delta}{12(1 - \nu^2)} \left(\frac{L}{Y} \right) \quad (2.9)$$

Eqs. 2.8 and 2.9 were used in finding effective width by many researchers in the past and also will be used in the current research. The influence of wall and slab geometry on the effective width of coupling floor slab was the subject matter of many research studies (Hossain 2003; Coull and Wong 1981, 1983, 1984; Qadeer and Smith, 1969; Tso and Mahmoud 1977; Coull and El-Hag 1975). Effective width (Y_e) is normalized with respect to the slab width (Y) and the Y_e / Y is expressed as a function of L/Y and $L/(L+W)$. The effective width increases with the increase of slab width, as wider slab should provide more restraint than the narrower ones against the bending action of the coupled shear wall structure. The resulting influence of slab is stronger when Y/X is smaller than L/X . When Y/X is greater than L/X , the influence of slab width becomes less. When Y/X reaches three times L/X , the width of slab has no effect on the effective slab width.

Hossain (2003) presented curves to evaluate Y_e/Y and concluded that the influence of slab width is strong when Y/X is smaller than L/X , but when Y/X is larger than L/X , the influence decreases rapidly. It was further concluded that the influence of external wall flanges may be ignored. Hossain (2003) extensively investigated the non linear behaviour of the coupling slab through finite element modeling for Reinforced Cement Concrete (RCC), by using micro-concrete properties from small scale tests. A non-linear finite element program was developed and its performance was validated through small scale model test results. RC is a non-linear material and

the flexural stiffness and effective width of floor slabs will be affected by cracking of concrete and yielding of steel. Therefore, flexural stiffness of floor slab determined based on linear analysis cannot be used throughout the loading history.

Hossain (2003) formulated design curves for the determination of flexural stiffness and effective width as functions of geometric parameters in the pre-cracking, cracking and post-yielding stages of non-linear material response. The bending stiffness (k_o) in pre-cracking stage was not affected by the amount of reinforcement in the slab. At cracking stage, stiffness increased by 6% when reinforcements were 25% higher, and gradually decreased with the increase of the loads. It is concluded from the study that the ratio of the cracking to pre-cracking stiffness ranges between 0.25 and 0.45 and the ratio of post-yielding to pre-cracking stiffness ranges between 0.08 and 0.22. Effective width gradually decreases with increase in load. The stiffness of coupling slabs is influenced by the geometric and non-linear material parameters of the structural component. Numerical and experimental results suggested that the design curves are reliable and can be used for the analysis and design of shear wall structure in practical situations.

2.2 Non-linear Analysis of Reinforced Concrete Coupled Shear Wall Structures

Non-linear analysis of reinforced concrete needs suitable modeling of its behaviour in pre-cracking and cracking stages as well as modeling of reinforcement. Although the steel behaviour is better defined and generally agreed upon, concrete behaviour shows considerable statistical scatter. A reinforced concrete model should handle suitably the cracking of concrete, crack propagation and yielding of steel.

Kotsovos et al. (1977, 1979 and 1984) provided mathematical expressions for deformational as well as strength properties of concrete suitable for use in non-linear computer based methods to analyze concrete structures after doing comprehensive investigations.

Kabir (1986), by numerical treatment of post-cracking behaviour of concrete, proposed that after the formation of crack, the stress normal to the crack should be reduced gradually to account for the tension stiffening effect. Reducing the crack normal stress to zero soon after formation of the crack may significantly underestimate the actual behaviour. Treating concrete as a no tension material is perhaps not numerically desirable especially in the context of smeared cracking model.

The conventional tension stiffening schemes are based on uni-axial stress relaxation procedures which depend on the strains normal to crack. The adoption of biaxial stress criterion for cracking and uni-axial stress decay for tension stiffening may lead to a mathematically inadmissible state of stress at a cracked point. To overcome this difficulty, an alternative scheme had been postulated by Kabir, which performed well. It should be noted that while this alternative scheme continuously decreases the crack normal stress in every subsequent iteration, and it fails to correlate the strain normal to crack with the corresponding stress. Considering the complex nature of crack propagation, such co-relation is not essential.

Coull and Wong (1983) described a finite element elastic analysis of the induced bending moments and shear forces in a slab coupled with shear wall to determine the best form of element to use in the computation of the model, and concluded that most suitable element was the simple rectangular element. The slab panel was divided into an assembly of plate bending elements using a suitable mesh pattern, as shown in Fig. 2.4. As a result of the conditions of symmetry and anti-symmetry, only one quarterly quadrant of the full panel needed to be analyzed. The displacements prescribed for the wall nodes were due either to a unit wall rotation or a unit relative vertical wall movement, the slab being subjected to the same form of deformation, relative to the wall, in each case. This solution furnished the displacements and stress-resultant values at all nodes, and also the slab reactions at the reserved nodes. The reactions at the wall nodes provide the static equivalent wall moment, M , and the total shear force, Q , transferred from the wall to the slab when the wall underwent the unit relative displacements assumed. Evaluation of the appropriate load-displacement relationship gave the coupling stiffness of the slab as illustrated in Fig. 2.2.

Coull and Wong (1984) further investigated coupled shear wall system walls of various configuration such as plane, T-shaped and L-shaped as shown in Fig. 2.5. The distributions of bending moments and shear forces induced in a slab coupling a pair of laterally loaded shear walls of any shape was evaluated and design method was proposed for checking punching shear failure in the slab.

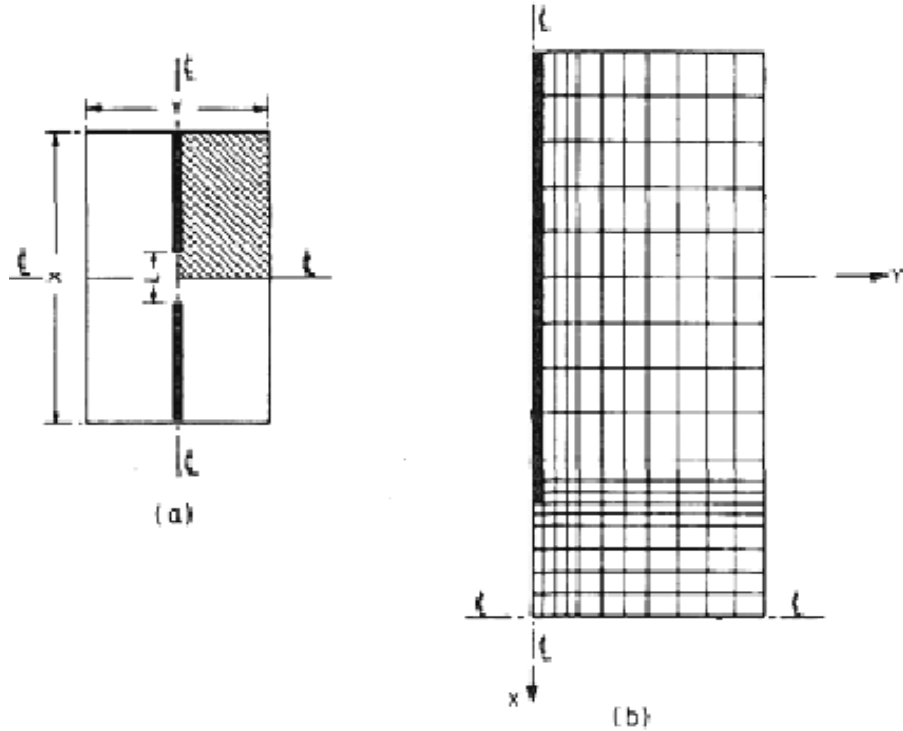


Figure 2.4: The plan of finite element model of slab (Coull and Wong 1983)

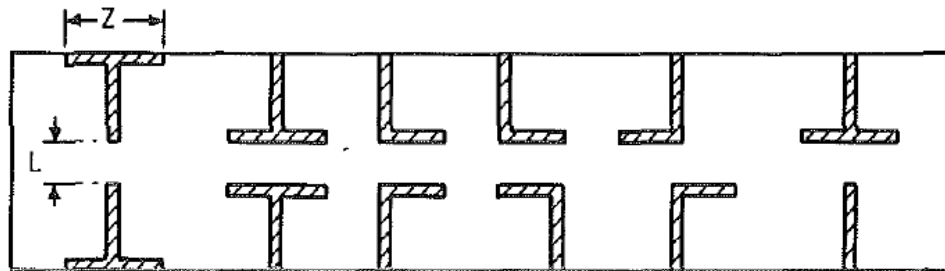


Figure 2.5: The plan of different T and L shaped coupled flanged shear wall system
(Coull and Wong 1984)

The non-linear finite element scheme was employed by Bari (1987), to study the behaviour of shear wall slab junction. The wall was assumed to have zero thickness and it was found that the ultimate strength of the structure was slightly lower and stiffness was slightly higher considering

the thickness of shear wall. Bari tested several models of shear wall-floor slab junction to establish suitable design method of shear wall slab structure using shear reinforcement and verified the results by non-linear 3-D finite element analysis, and considered the effect of lateral load as a concentrated load applied at the point of contra-flexure of the slab. He treated the slab as a cantilever extended from shear wall. Lateral load effect was applied through vertical load at the tip of the slab at point of contra-flexure. From findings, Bari produced load deflection curve to find out stiffness of the slab. It was concluded that the stiffness of the slab decreases as the load increases, but stiffness may not be considered as bending/flexural stiffness of the slab because walls does not rotate and slab deflect as a true cantilever from shear wall.

Hossain (2003) developed a non-linear finite element program using 3-D iso-parametric brick element to model coupled shear wall system. Non-linear behaviour of concrete was modeled by incorporating Kotosovs' 3-D model (1984) simulating cracking, crack propagation, crack closing and shear retention phenomena. It was found that the finite element mesh size has insignificant effect on the strains up to the yield point, but it has considerable effect on the failure load. For the slab model analyzed, it was found that the failure load decreases about 20% when mesh is refined from six to twelve elements. And also found that the strains are not affected by the value of shear retention factor up to yield point of the steel but ultimate load is affected. The high convergence tolerance with no tension stiffening model has a considerable advantage over the tension stiffening model in that it requires a smaller number of iterations to keep the residual forces within tolerance and hence less computer time. Hossain (2003) Thousands of numerical slabs with varying geometric dimensions were simulated after the validation of the model through test results and data from other research studies. Bending stiffness and effective width of floor slabs in pre-cracking, cracking and post-yielding stages of the response were evaluated and presented in terms of design charts and equations.

2.3 Cracking and Failure of Coupling Slabs in Shear Wall Structures

In the coupled shear wall system, it is always assumed that the initial cracking of the slab would occur at the most heavily stressed inner corridor edges of the shear walls, normal to the principal moment directions.

Schwaighofer and Collins (1977); Paulay and Taylor (1981) and Mirza and Lim (1989) have analyzed the influence of cracking on the effective stiffness of slabs subjected to either monotonic or cyclic loading. It shows that a considerable loss of stiffness occurs because of cracking up to reduction of 60% or even higher. If a slab is subjected to reverse cyclic loading with increasing imposed inelastic deformations, additional stiffness degradation may develop. Consequently, it is important to assess overall behaviour of the coupled wall system accurately; the influence of cracking on the slab stiffness should be examined.

Coull and Wong (1990) analyzed coupling slabs using linear elastic finite element modeling. The theoretical and experimental studies have shown that the main coupling action takes place in the passage (corridor) area at inner side of the coupled shear wall, and high stresses occur in the region of the inner edges of the shear walls. These high stresses may cause cracking of the concrete with yielding of the reinforcing steel bars, resulting reduction in the coupling stiffness as flexural resistance is almost reduced in most parts of the slab. On other hand, cracking causes a redistribution of stresses to other parts of the slab and activate other areas that are previously ineffective. So cracking plays some role for the loss of stiffness and redistribution of stress.

Hossain (2003) described cracking and failure of coupling slabs in a comparative study of finite element and experimental small scale models. Cracks started from the interior edges of the shear wall and gradually spread towards the edge of the slab and failure was occurred at the section passing through the interior edge of the shear wall, as shown in Fig. 2.6.

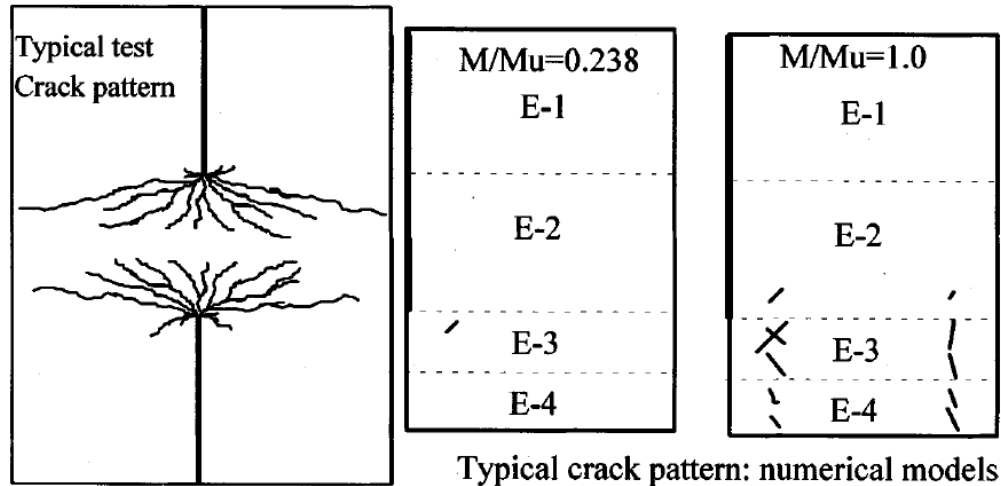


Figure 2.6 Crack pattern and failure of coupling slabs (Hossain 2003)

Results and conclusion of previous studies show that coupling slab failed due to the formation of transverse crack across the most heavily stressed inner end of the wall and resulted in a substantial reduction in the effective coupling stiffness of the slab. The distribution of longitudinal moments in the slab is not greatly affected by the crack, at a distance from the region near the top of the crack, where bending stress concentrations take place.

2.4 Modes of Failure of Coupled Shear Wall Structure

The shear or diagonal splitting is most common mode of failure in RCC beam, and researchers like Paulay and Subedi did different researches to find out failure modes in the buildings due to any lateral loading (Paulay 1971; Subedi 1991). Three modes of failure in RC coupled shear wall structures were identified basically depending upon the interaction and the behaviour of the coupling slab beams. In some failure modes, the walls fail before the coupling beams or slabs reach at their ultimate strength or the beam will partially collapse when the crushing of the wall takes place. These modes of failure depend on the effectiveness of the coupling action; if the coupling action is flexible, the flexural and shear failure occurs. Subedi (1991) explained these three modes of failures as illustrated in Fig. 2.7.

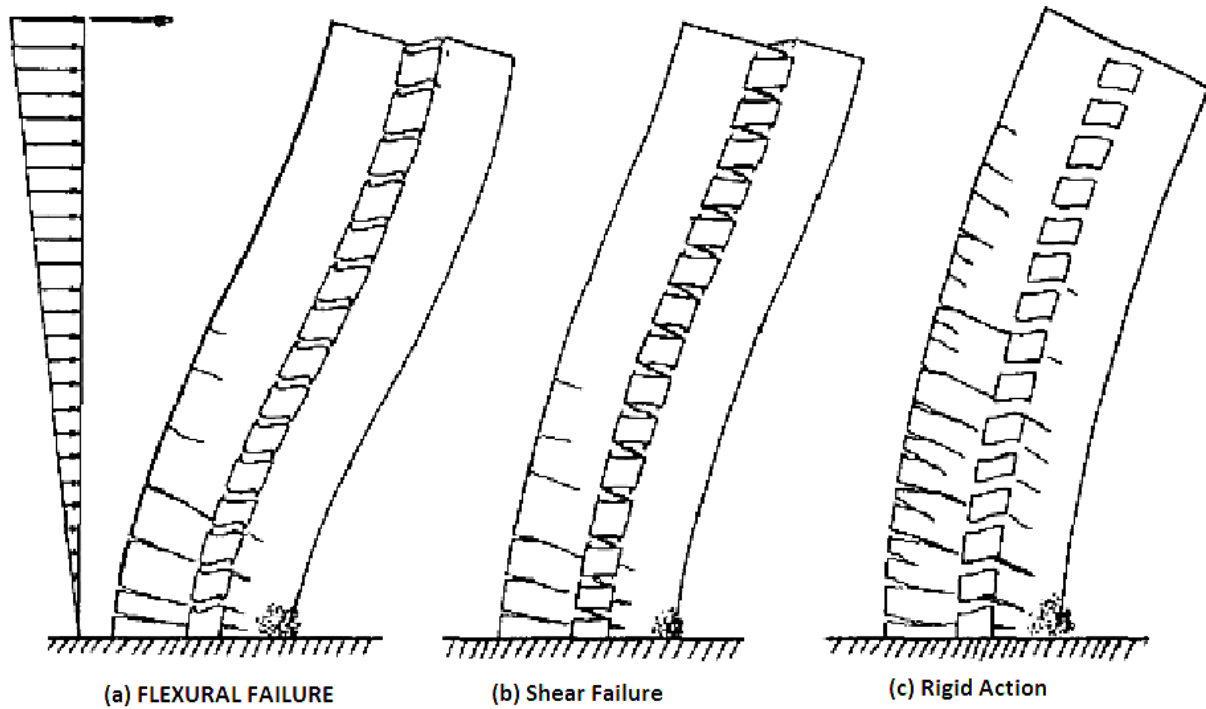


Figure 2.7: Failure modes of coupled shear wall under lateral load (Subedi 1991)

Flexural Failure: it occurs in walls with relatively thin small coupling beams reinforced with a small amount of main reinforcing steel. Firstly, under the action of the horizontal load, the walls will deform with the formation of flexural cracks in the tension side of the wall. The coupling beams near the highly stressed levels will develop flexural cracks at the joint near the inner side of walls. As the load is increased, the flexural cracks will progress deeper into the wall. Some new cracks may also develop along the height of the wall. The flexural cracks will also spread into more coupling beams/slabs. Since the load is amplified, the failure of the wall will occur by the crushing of the compression wall at the most highly stressed corner and the spread of flexural cracks in most of the coupling beams along the height, as shown in Fig. 2.7(a).

Shear or Diagonal-Splitting Failure: This failure starts initially after formation of flexural cracks in the tension side of wall. The coupling beams near the highly stressed levels might show some minor flexural cracks at the junction with the walls. As the lateral load is increased, the main feature in this mode of failure will be the formation of diagonal-splitting cracks in the coupling

beams around the highly stressed levels, and the inclined cracks starting near the center of the coupling beams and extending across the compression diagonal. A further increment of load will show some progress in the already-formed flexural cracks, with some new flexural cracks along the height of the wall. The spread of diagonal splitting into other coupling beams will follow as load continues to increase. The wall fails with the crushing of the compression wall at the most highly stressed corner. Diagonal splitting of most of the coupling beams will also be completed almost simultaneously with the crushing of the wall, Fig. 2.7(b).

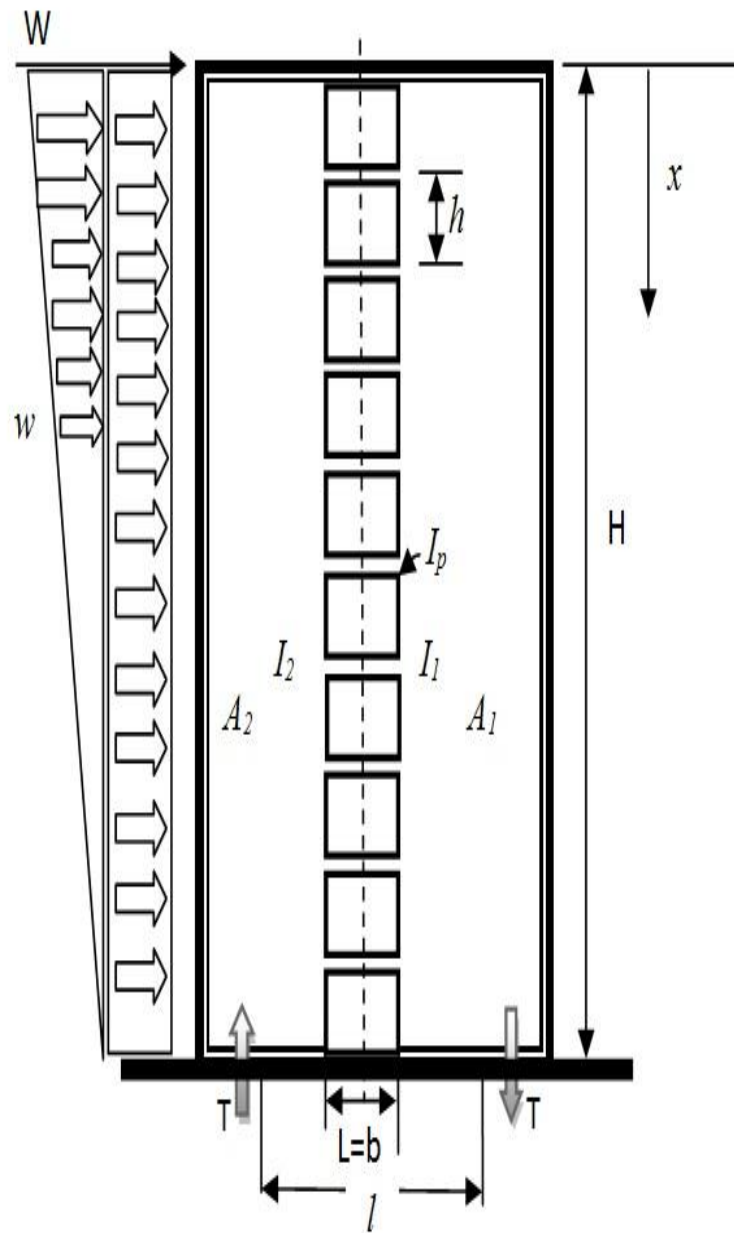
Rigid Action: The coupling action is stronger because of stiffer beam/slab and this mode of failure will occur when the tension wall will develop a large number of cracks along the height of the structure. Whatever might have been the ultimate mode of failure of the coupling beams/slabs, the failure of the wall will look like a simple cantilever beam under the action of the lateral load, as shown in Fig. 2.7(c).

2.5 Analysis of Coupled Shear Wall Structures

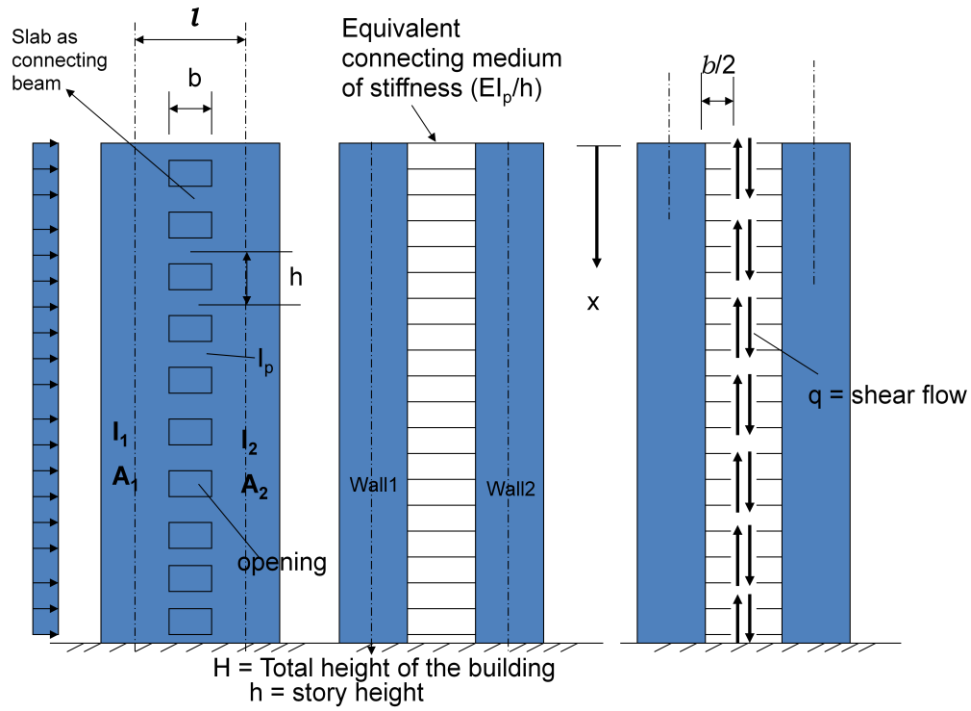
Coupled shear wall structure resists the lateral load by cantilever bending action resulting in rotation of the wall cross-sections and generating moments in the slabs. The free bending of a pair of shear wall is resisted by the floor slabs, which are forced to rotate and bend out of plane where they are connected rigidly to the walls. Due to large depth/width of the wall, considerable differential shearing action is imposed on the connecting slab, which develops transverse reactions to resist the wall deformations and induces tensile and compressive forces (T) into the walls (Fig. 2.8). As a result of the large lever arm involved, relatively small axial forces can give rise to substantial moment of resistance. The resistance of the floor slab against the displacements imposed by the shear walls is a measure of its coupling stiffness, which can be defined in terms of the displacements at its ends and the forces producing them.

The simplified analysis of coupled shear walls based on an assumption that the detached system of the connections formed by lintel beams or slab may be replaced by an equivalent continuous medium (*laminas*) in which walls are coupled together with the slab, as shown in Fig.

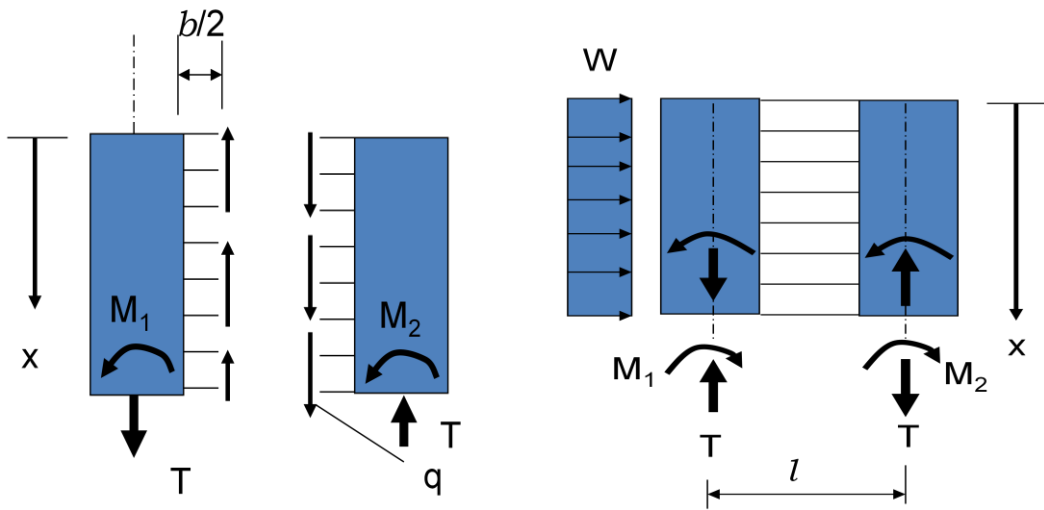
2.8. By considering this assumption the axially rigid beam or slab forms point of contra-flexure at the mid of the beam or slab as shown in Figs. 2.2 and 2.3. This technique has been used by Chitty (1947) in analysis of cantilever composed of parallel beams interconnected by cross beams.



(a)



(b)



(c)

Figure 2.8: (a) Coupled shear wall with equivalent continuous of laminae under lateral loadings
 (b) Coupled shear wall showing laminar shear flow and (c) Showing laminar shear force and moments (Hossain 2003)

The coupled shear wall with slab under the lateral load deflects and rotates, which produces deformation (δ) due to wall moment (M) in the slab as shown in Fig. 2.2. The slab portion between the walls with length (L) (opening in walls) acts as connecting beam and resist the moment in the walls and effectively contribute in the whole system.

2.5.1 Continuous Medium Method

In continuous medium method (Coull and Choudhury 1967a), individual coupling slab beams of stiffness are replaced by an equivalent continuous medium or laminas of stiffness as shown in Fig. 2.8. It is assumed that connecting/coupling slab beams do not deform axially and under the action of lateral loading both walls deflect equally with a point of contra-flexure at the midpoint of each connecting beams.

2.5.1.1 Analysis for Uniformly Distributed Load

The shear wall building with equal storey height (h) is subjected to uniformly distributed loading (w) as shown in Fig. 2.8 (a,b,c). Consider individual connecting beam of stiffness EI_p is replaced by laminas of stiffness EI_p / h per unit height. If the laminas are considered cut at their midpoints, the only force acting at cut section is shear force of intensity (q) per unit length. On considering the deformation of cut laminas, the compatibility conditions are set up to give no resultant relative deformation at the cut midpoint which leads to governing differential equation for the total shear force (T) in the connecting medium. Once the distribution T has been established, the shear force (Q) in the connecting beam at any level is obtained as the difference between the values of integral at levels $h/2$ above and below the beam. Also from T , moment and axial loads in the walls can then be established as well as stress in the walls at any level x . The moment at the junction of coupling beam and wall at various levels can also be found.

The behaviour of this system can be expressed as single order differential equation, enabling a general closed solution to the problem. Under lateral loads the coupling beam will undergo vertical displacement due to wall rotation, beam bending, beam shear deformation and axial tension and compression in shear walls. The relation can be expressed as second order differential equation as:

$$\frac{d^2T}{dx^2} - \alpha^2 T = -\beta x^2 \quad (2.10)$$

Where, T is integral of the shear flow ‘ q ’ in the continuous connection from top of the wall till x , which can be expressed as:

$$T = \int_0^x q \, dx \quad (2.11)$$

$$\alpha^2 = \frac{12I_p}{hb^3} \left[\frac{l^2}{I} + \frac{A}{A_1 A_2} \right] \quad (2.12)$$

$$\beta = \frac{1}{2} w l \left(\frac{12I_p}{hb^3} \right) \frac{1}{l} \quad (2.13)$$

$$I = I_1 + I_2$$

$$A = A_1 + A_2$$

$$I_p = \frac{I_b}{1 + 2.4 \left(\frac{t}{b} \right)^3 (1 + \nu)} \quad (2.14)$$

Where, t = depth of coupling slab; $b = L$ = width of opening and ν = Poisson’s ratio of the material; I_1 and I_2 = moment of inertia of wall 1 and 2, respectively; A_1 and A_2 : area of wall 1 and wall 2, respectively; E = modulus of elasticity of beam materials; I_b = moment of inertia of interconnecting beam; I_p = reduced the moment of inertia to reduced moment of inertia to include the effect of shear deformation; I_b = moment of inertia of the coupling beam = $Y_e \cdot t^3 / 12$. Y_e are the effective width of the slab, which is variable in the pre-cracking, cracking and post-yielding stages of the coupling slab/beam.

By substituting and solving Equation 2.10 with boundary condition, we get final solution as (Coull and Choudhury 1967a):

$$T = \frac{2\beta}{\alpha^4} \left\{ 1 + \frac{\sinh \alpha H - \alpha H}{\cosh \alpha H} \sinh \alpha x - \cosh \alpha x + \frac{1}{2} \alpha^2 x^3 \right\} \quad (2.15)$$

Once the distribution of the laminar shear force (T) across the height of the building has been determined, the shear force Q_i in any connecting beam or slab can be obtained from difference in values of T at level $\frac{h}{2}$ above and below beam or floor slab.

Also from T , moment and axial loads in the walls can then be established as well as stress in the walls at any level x . The moment at the junction of coupling beam and wall at various levels can also be found as $\frac{1}{2} Q_i b$. The deflected form of the structures can then be established by integrating moment curvature relationships.

The moments M_1 and M_2 in Wall 1 and Wall 2, respectively can be written as (Fig. 2.8c):

$$M_1 = \left(\frac{1}{2} wx^2 - Tl \right) \frac{l_1}{l} \quad \& \quad M_2 = \left(\frac{1}{2} wx^2 - Tl \right) \frac{l_2}{l} \quad (2.16)$$

It is assumed that the loads on the wall deflect walls equally due to high stiffness of the slabs and also the wall containing the opening or passage behave in same manner as the walls do not act separately. It is important for the design of any coupled shear wall system to know the stresses and deflection due to applied loads. Coull and Choudhury (1967a) described the complete stress distribution at any section of the coupled shear wall structure by superposition of two pure bending stress distributions. It was assumed that the wall system acts as a single composite cantilever with the neutral axis situated at the centroid of two walls (composite cantilever action) as well as the walls act completely independently with the neutral axis situated at the centroid of each of the wall (independent cantilever action).

As per Coull and Choudhury (1967a), the actual stress distribution in walls is equal to the sum of composite cantilever stresses (Fig 2.9c) and independent cantilever stresses (Fig 2.9d). By assuming again in independent cantilever action to ignore axial deformation, the wall will deflect equally and the load carried will be proportional to moment of inertia. So the bending moment in walls are expressed as:

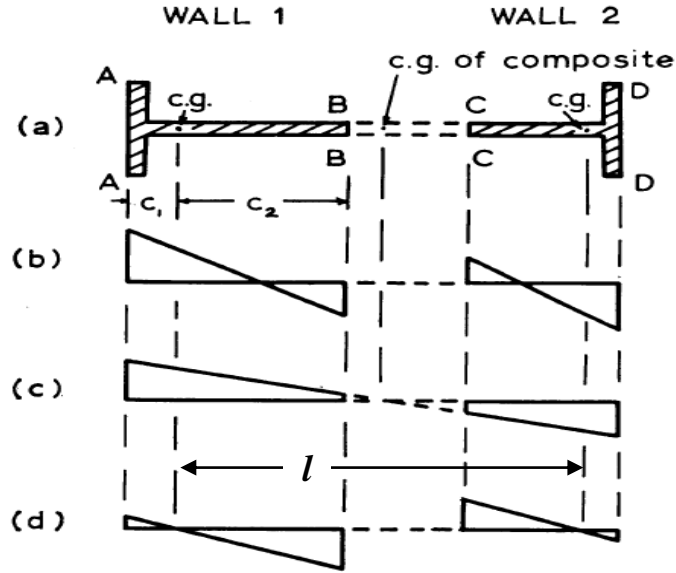


Figure 2.9: Plan of walls with stress distribution (Coull and Choudhury 1967a)

$$M_1 = \left(\frac{1}{2}wx^2\right) \frac{l_1}{l} \frac{K_1}{100} \quad \& \quad M_2 = \left(\frac{1}{2}wx^2\right) \frac{l_2}{l} \frac{K_1}{100} \quad (2.17)$$

Where, K_1 is the percentage of load carried by independent cantilever action.

In composite cantilever action, the bending moment $\left(\frac{1}{2}wx^2\right) \frac{K_2}{100}$ will be carried by the walls. Where, K_2 is the percentage of load carried by composite cantilever action.

Taking tensile stresses as positive, the maximum extreme fiber stresses at A (σ_A) and B (σ_B) of wall 1 as shown in Fig. 2.9 can be derived as:

$$\sigma_A = \frac{M_1 C_1}{I_1} + \frac{T}{A_1} = \left(\frac{1}{2} w x^2 - T l \right) \frac{C_1}{I} + \frac{T}{A_1}$$

(2.18)

$$\sigma_B = - \frac{M_1 C_2}{I_1} + \frac{T}{A_1} = - \left(\frac{1}{2} w x^2 - T l \right) \frac{C_2}{I} + \frac{T}{A_1}$$

Where, C_1 and C_2 are the distances from centre of gravity of wall 1 to points A and B, respectively (Fig. 2.9). Similar equations can be derived for wall 2.

In composite cantilever action, the stresses at A and B can be derived as:

$$\sigma_A = \frac{w x^2}{2 I'} \left(\frac{A_2 l}{A} + C_1 \right) \frac{K_2}{100}$$

(2.19)

$$\sigma_B = \frac{w x^2}{2 I'} \left(\frac{A_2 l}{A} - C_2 \right) \frac{K_2}{100}$$

Where, I' is the moment of inertia of the composite cantilever, given by:

$$I' = I_1 + I_2 + \frac{A_1 A_2}{A} l^2$$

In individual cantilever action, the stresses in wall can be derived as:

$$\sigma_A = \frac{M_1 C_1}{I_1} = \frac{w x^2}{2} \left(\frac{C_1}{I} \right) \frac{K_1}{100}$$

(2.20)

$$\sigma_B = - \frac{M_1 C_2}{I_1} = - \frac{w x^2}{2} \left(\frac{C_2}{I} \right) \frac{K_1}{100}$$

By equating, corresponding stresses at the four extreme fibers, positions for wall 1 and 2 from Eqs. 2.18, 2.19, and 2.20, K_2 can be expressed finally as:

$$K_2 = \frac{200}{(\alpha H)^2 \left(\frac{x}{H}\right)} \left\{ 1 + \frac{\sinh \alpha H - \alpha H}{\cosh \alpha H} \sinh \alpha H \left(\frac{x}{H}\right) - \cosh \alpha H \left(\frac{x}{H}\right) + \frac{1}{2} (\alpha H)^2 \left(\frac{x}{H}\right)^2 \right\} \quad (2.20)$$

The variation of K_2 as a function of stiffness ' αH ' for different values of height ratio ' x/H ' is shown graphically in Fig. 2.10. The value of $K_1 = 100 - K_2$, also plotted in Fig. 2.10.

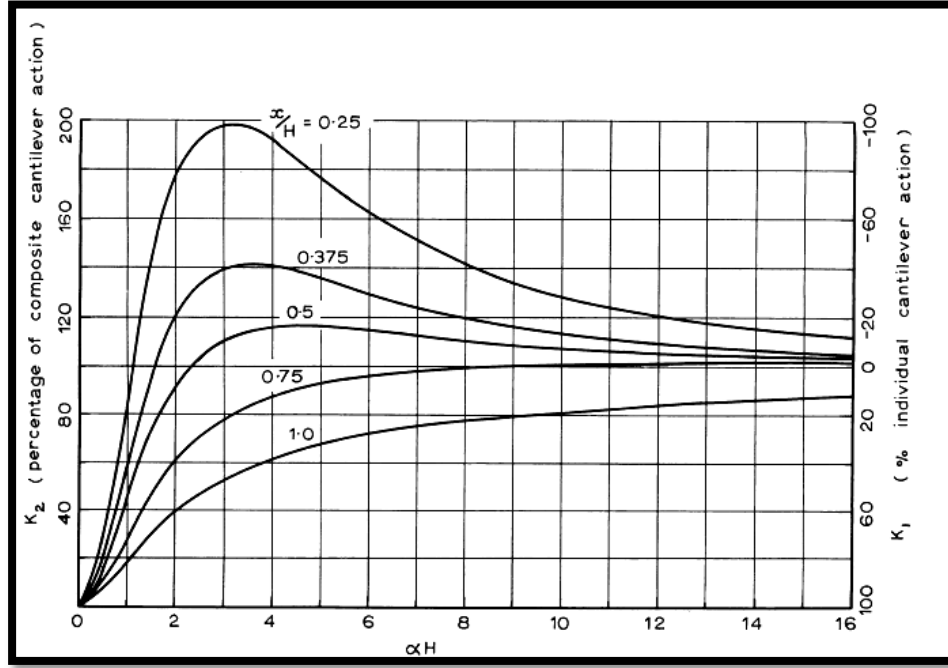


Figure 2.10: Variation of K_2 with x/H (Coull and Choudhury 1967a)

The stresses at connecting beams/slabs with respect to shear force per unit height in the equivalent continuous system for uniformly distributed load are expressed as:

$$q = \frac{dT}{dx} = w \frac{H}{l} \frac{1}{\mu} K_3 \quad (2.22)$$

Where,

$$\mu = 1 + \frac{A}{A_1 A_2} \frac{I}{l^2}$$

$$K_3 = \left\{ \frac{\sinh \alpha H - \alpha H}{\alpha H \cosh \alpha H} \cosh \left(\alpha H \frac{x}{H} \right) - \frac{\sinh \alpha H \left(\frac{x}{H} \right)}{\alpha H} + \frac{x}{H} \right\} \quad (2.22 \text{ a})$$

In this case shear force depends upon μ , α and x/H . Now differentiating Eq. 2.18, the maximum shear force intensity (q_{max}) can be derived as:

$$q_{max} = w \frac{H}{l} \frac{1}{\mu} K_3' \quad (2.23)$$

Where, K_3' is the maximum value of K_3 , as shown in Fig. 2.11.

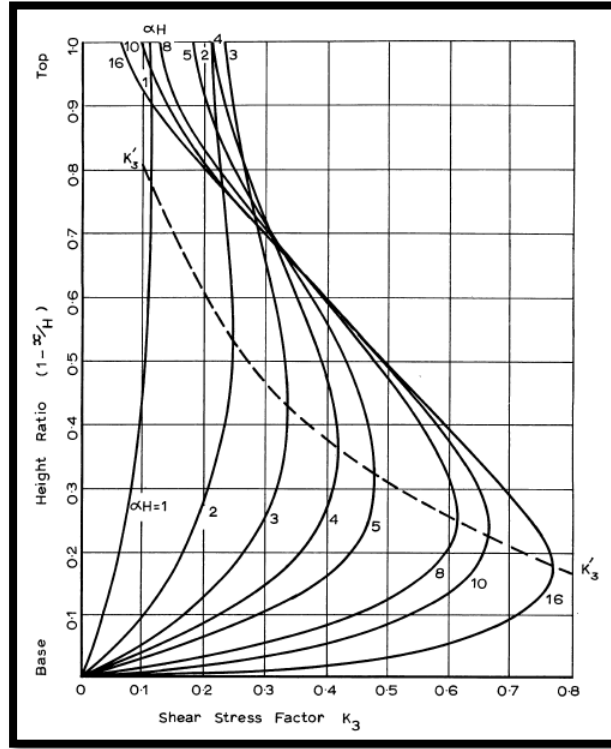


Figure 2.11: Variation of K_3 with the αH and x/H (Coull and Choudhury 1967a)

By obtaining required coefficient K_3 , the shear force ' Q ' in any particular beam/coupling slab can be calculated by the area between half storey height levels above and below the beam position.

The bending stresses in the walls may be obtained from ordinary beam theory, described in Eqs. 2.18, 2.19 and 2.20.

The moment-curvature relationship presented in Eq. 2.23a can be used in finding deflection (y) at any height x :

$$EI \frac{d^2y}{dx^2} = \frac{1}{2} w x^2 - Tl \quad (2.23a)$$

In particular, maximum deflection at the top of the structure (y_{\max}) can be expressed as:

$$y_{\max} = \frac{1}{8} \frac{wH^4}{EI} K_4 \quad (2.23b)$$

Where,

$$K_4 = \frac{\mu-1}{\mu} - \frac{8}{\mu} \left[\frac{\alpha H \sinh \alpha H - \cosh \alpha H + 1}{(\alpha H)^4 \cosh \alpha H} - \frac{1}{2(\alpha H)^2} \right] \quad (2.23c)$$

K_4 can also be obtained by using Fig. 2.12.

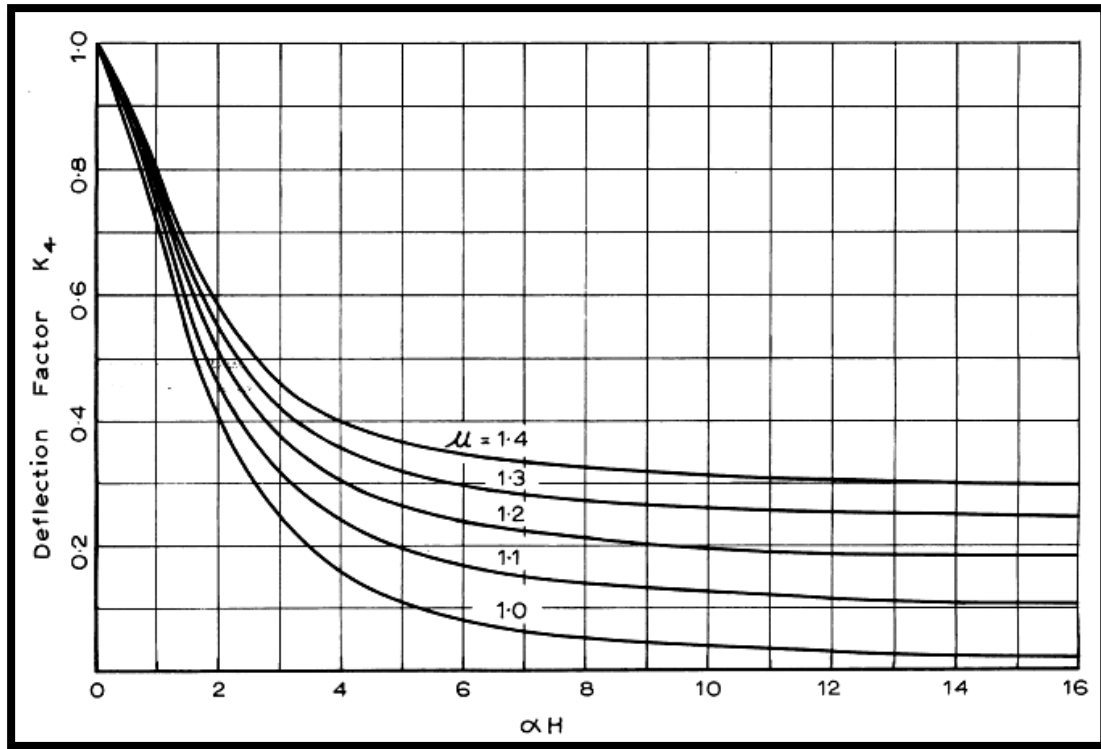


Figure 2.12: Curves showing the variation of K_4 with the αH and μ (Coull and Choudhury 1967a)

2.5.1.2 Analysis for Distributed, Triangular and Point Loading

Coull and Choudhury (1967b) described the analysis of coupled shear wall system (as shown in Fig. 2.13) subjected to a uniformly distributed loading (p) triangular loading with max intensity of w and point load (W) acting in the same direction. The second order differential equation for the system may be expressed as similar to previous equation as:

$$\frac{d^2T}{dx^2} - \alpha^2 T + W\beta x + w\beta x^2 \left(\frac{1}{2} - \frac{x}{6H} \right) + \frac{1}{2}p\beta x^2 = 0 \quad (2.24)$$

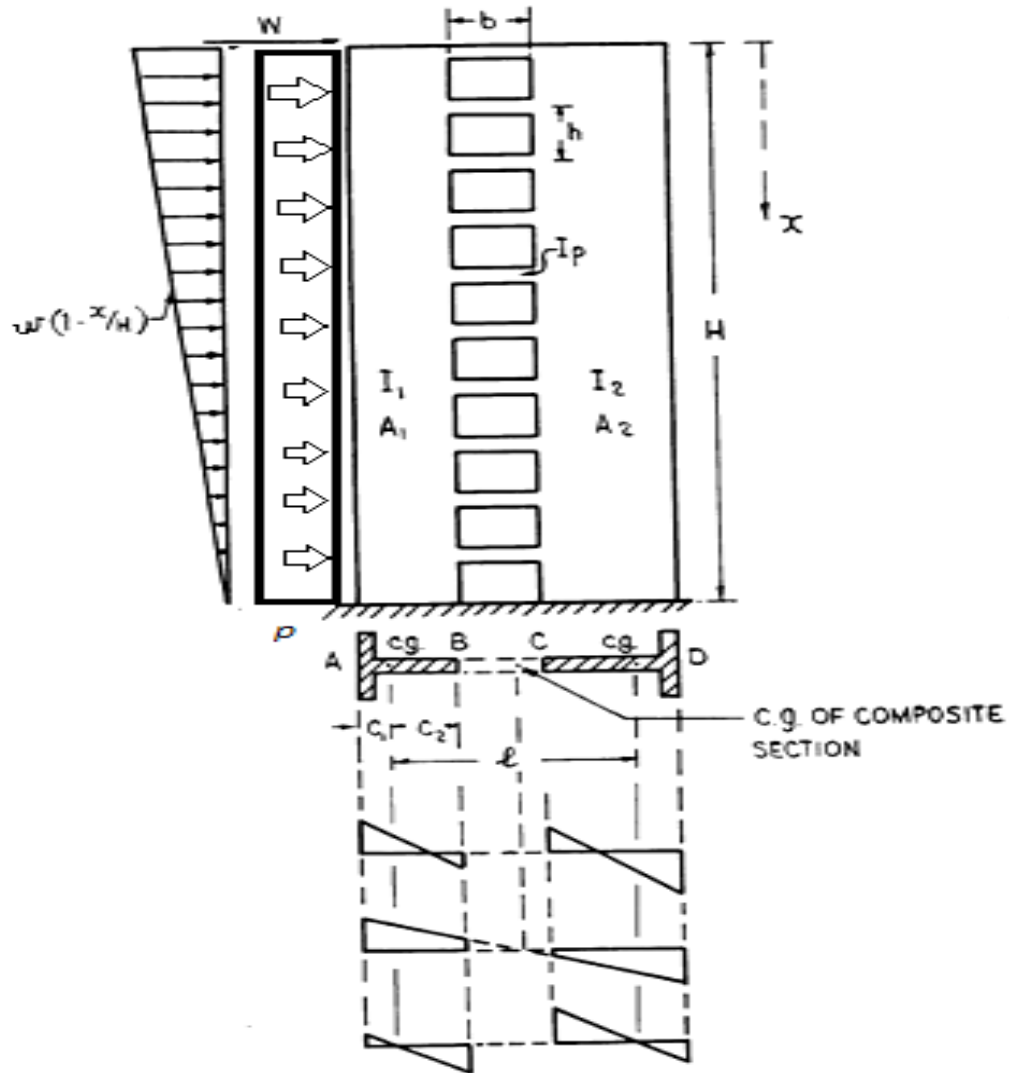


Figure 2.13: Coupled shear wall under uniform loading, triangular and point loading

(Coull and Choudhury 1967b)

Equation 2.24, the third, fourth and fifth terms represent the effect of point load, triangularly distributed load and uniformly distributed load effect, respectively.

The integral of the shear force (T) in the continuous connection from top of the wall till x can be expressed as:

$$T = \int_0^x q \, dx \quad (2.25)$$

$$\alpha^2 = \beta \mu l \quad (2.26)$$

$$\beta = \left(\frac{12I_p l}{hb^3 I} \right) \quad (2.27)$$

$$\mu = 1 + \frac{A}{A_1 A_2} \frac{I}{l^2}$$

Similarly to previous case, the bending moment in the walls are given by:

$$M_1 = (M_0 - Tl) \frac{l_1}{l} \text{ \& } M_2 = (M_0 - Tl) \frac{l_2}{l} \quad (2.28)$$

Where,

M_0 is the moment at the section, given by;

$$M_0 = Wx + wx^2 \left(\frac{1}{2} - \frac{x}{6H} \right) + \frac{1}{2} px^2 \quad (2.29)$$

In composite cantilever action the stresses at A and B of the wall can are given by:

$$\sigma_A = \frac{M_0}{I'} \left(\frac{A_2 l}{A} + C_1 \right) \frac{K_2}{100} \quad (2.30)$$

$$\sigma_B = \frac{M_0}{I'} \left(\frac{A_2 l}{A} - C_2 \right) \frac{K_2}{100}$$

Where, I' is moment of inertia of the composite cantilever, given by:

$$I' = I_1 + I_2 + \frac{A_1 A_2}{A} l^2$$

Individual cantilever action, the loads carried are proportional to the stiffness of individual elements, so that the bending moment carried by each walls are given by:

$$M_1 = M_0 \frac{K_1 I_1}{100 I} \quad \& \quad M_2 = M_0 \frac{K_1 I_2}{100 I} \quad (2.31)$$

Extreme fiber stresses in wall 1 becomes:

$$\sigma_A = M_0 \frac{K_1 C_1}{100 I} \quad (2.32)$$

$$\sigma_B = M_0 \frac{K_1 C_2}{100 I}$$

On equating corresponding stresses at the four extreme fiber position the proportional function K_2 is found, and expressed finally as:

For point load at the top (values can also be obtained from Fig. 2.14):

$$K_2 = 100 \left\{ 1 - \frac{\sin h \alpha x}{\alpha x \cos h \alpha H} \right\} \quad (2.33)$$

For triangularly distributed load (values can also be obtained from Fig. 2.15:

$$K_2 = \frac{200}{(\alpha H)^2 \left(\frac{x}{H}\right)^2} \left\{ 1 + \frac{\sin h \alpha H - \left(\frac{\alpha H}{2}\right) + \left(\frac{1}{\alpha H}\right)}{\cos h \alpha H} - \cos h \alpha x - \frac{\alpha^2 x^3}{6H} + \frac{1}{2} (\alpha H)^2 + \frac{x}{H} \right\} \quad (2.34)$$

Where, x/H is height ratio, and α is geometric parameter.

Similarly, the values of $K_1=100-K_2$, can be obtained using Equations as well as Figs. 2.14 and 2.15.

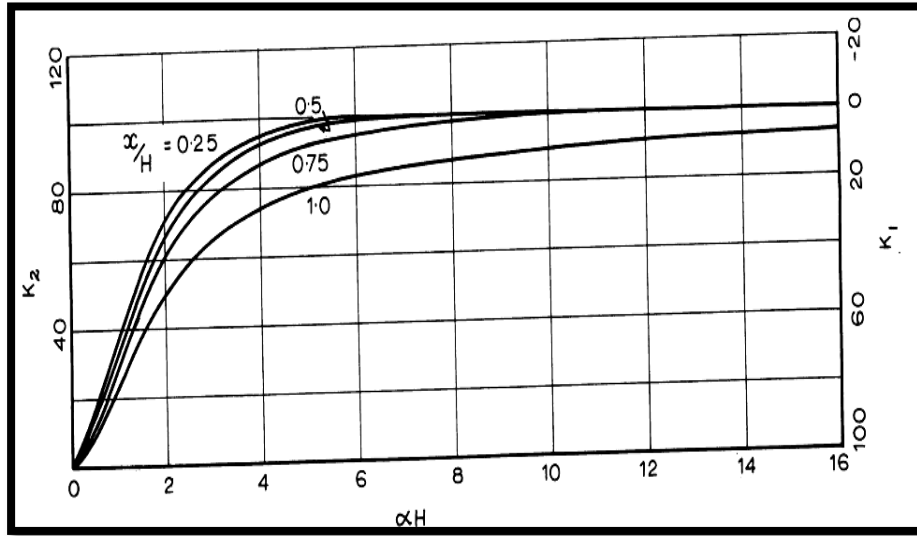


Figure 2.14: Curves showing the variation of K_1 and K_2 for point load at the top
(Coull and Choudhury 1967b)

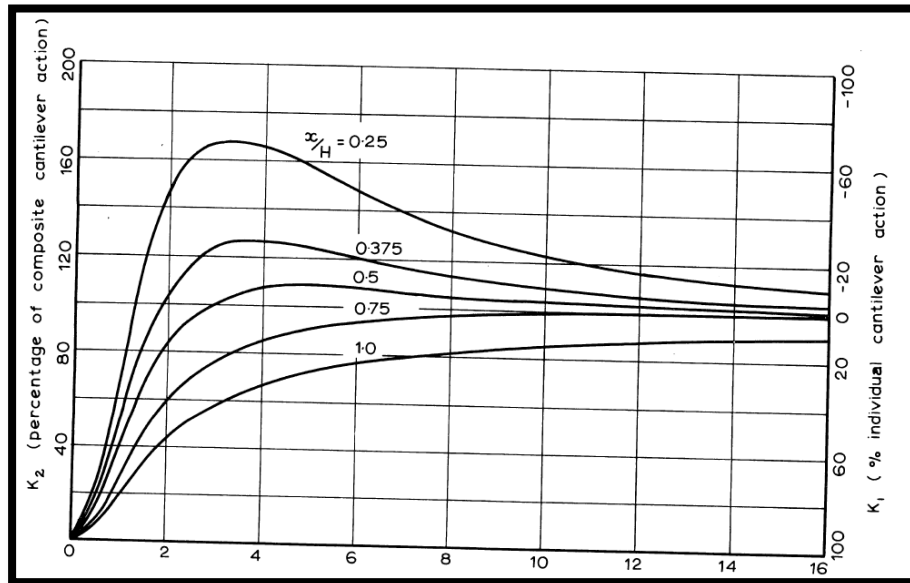


Figure 2.15: Curves showing the variation of K_1 and K_2 for triangularly distributed load
(Coull and Choudhury 1967b)

The shear flow per unit height ' q ' in the connecting medium for point load can be expressed as:

$$q = \frac{dT}{dx} = \frac{W}{l} \frac{1}{\mu} K_3 \quad (2.35)$$

Where,

$$K_3 = \left\{ 1 - \frac{\cos h \alpha x}{\cos h \alpha H} \right\} \quad (2.36)$$

For triangular and uniformly distributed loading;

$$q = \frac{dT}{dx} = w \frac{H}{l} \frac{1}{\mu} K_3 \quad (2.37)$$

Where,

$$K_3 = \left\{ \frac{\sin h \alpha H - \left(\frac{\alpha H}{2}\right) + \left(\frac{1}{\alpha H}\right)}{\alpha H \cos h \alpha H} \cos h \alpha x \frac{\sinh \alpha x}{\alpha H} - \frac{1}{(\alpha H)^2} - x^2/2H^2 + \frac{x}{H} \right\} \quad (2.38)$$

In the case of triangularly distributed load, the maximum value of K_3 is indicated by a broken line as shown in Fig. 2.11. For point load the maximum value of K_3 always occurs at the top.

The moment-curvature relation can be used to find the maximum deflection (y_{max}) that occurs at the top of the wall and can be expressed as:

For point load at the top;

$$y_{max} = \frac{WH^3}{3EI} K_4 \quad (2.39)$$

Where,

$$K_4 = 1 - \frac{3}{\mu} \left\{ \frac{1}{3} + \frac{\sinh \alpha H}{(\alpha H)^3 \cosh \alpha H} - \frac{1}{(\alpha H)^2} \right\} \quad (2.40)$$

and also can be obtained from Fig. 2.16

For triangularly distributed load, the maximum deflection can be expressed as:

$$y_{max} = \frac{11}{120} \frac{wH^4}{EI} K_4 \quad (2.41)$$

Where,

$$K_4 = 1 - \frac{1}{\mu} + \frac{120}{11} \frac{1}{\mu(\alpha H)^2} \left\{ \frac{1}{3} - \frac{1 + \left(\frac{\alpha H}{2} - \frac{1}{\alpha H} \right) \sinh \alpha H}{(\alpha H)^2 \cosh \alpha H} \right\} \quad (2.42)$$

And also can be obtained from Fig. 2.16.

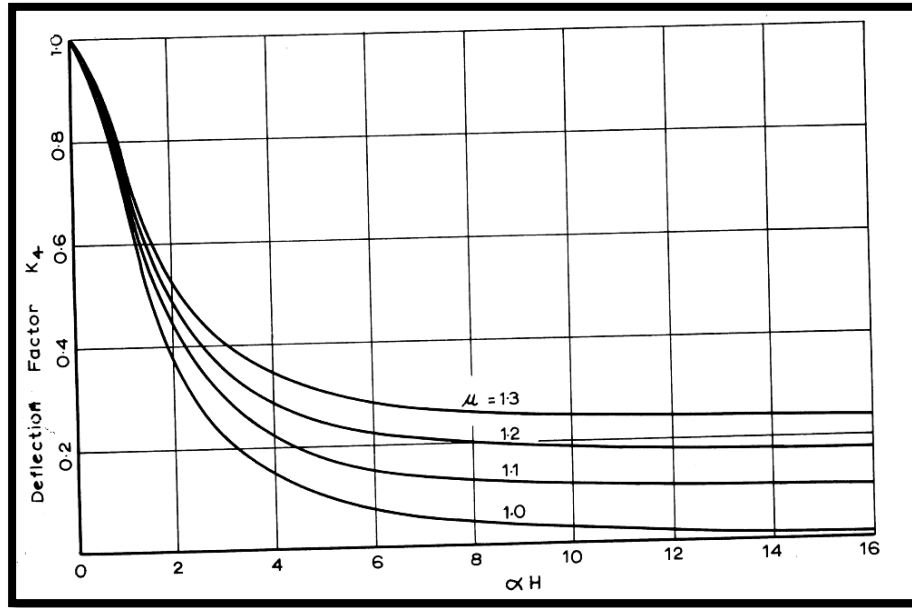


Figure 2.16: Curves showing the variation of deflection factor K_4 for point load at top and triangular loading (Coull and Choudhury 1967b)

2.5.1.3 Analysis of Shear Walls with Multiple Bay of Opening

For shear walls with one or two bands of opening uniformly located throughout connecting system (Fig. 2.7), the design will be based on the most highly stressed beam subjected to the greatest shear force Q_{max} , expressed in terms of K_1 and K_2 proposed by Coull and Irwin (1969).

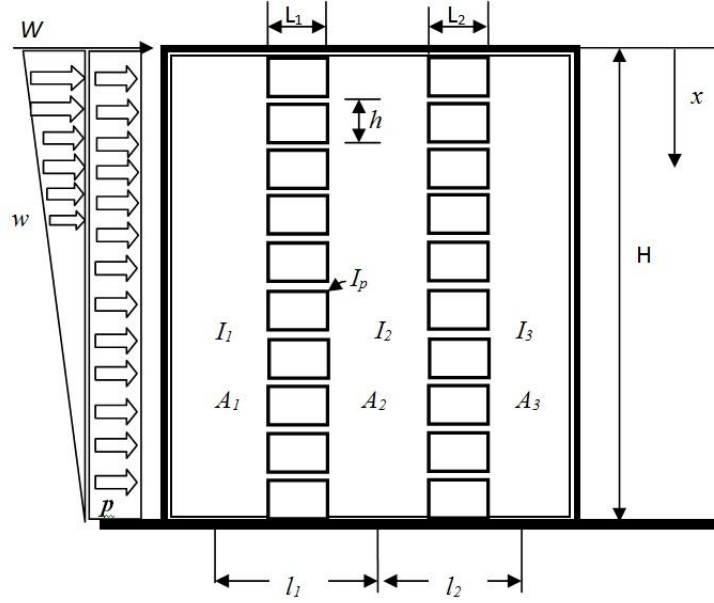


Figure 2.17: Building with Shear wall with two band openings

For uniformly distributed load:

$$Q_{max} = p \frac{\mu^2 H^2}{\alpha^2} K_1 \quad (2.43)$$

Where, p is intensity of uniformly distributed load and

$$K_1 = \left[\left(1 - \frac{x}{H} \right) \frac{h}{H} + \frac{2 \sinh \left(\frac{\alpha H}{2} \frac{h}{H} \right)}{(\alpha H)^2 \cosh \alpha H} \left\{ \sinh \left(\alpha H \frac{x}{H} \right) - \alpha H \cosh \alpha H \left(1 - \frac{x}{H} \right) \right\} \right] \quad (2.44)$$

For triangularly distributed load:

$$Q_{max} = w \frac{\mu^2 H^2}{\alpha^2} K_2 \quad (2.45)$$

Where, w is maximum intensity of triangular load, and

$$K_2 = \left[\frac{1}{2} \frac{h}{H} - \frac{1}{2} \frac{h}{H} \left(\frac{x}{H} \right)^2 - \frac{1}{24} \left(\frac{h}{H} \right)^3 - \frac{1}{(\alpha H)^2} \frac{h}{H} + \sinh \left(\frac{\alpha H}{2} \frac{h}{H} \right) \left\{ \frac{2 \sinh \left(\alpha H \frac{x}{H} \right) + \left(\frac{2}{\alpha H} - \alpha H \right) \cosh \alpha H \left(1 - \left(\frac{x}{H} \right) \right)}{(\alpha H)^2 \cosh \alpha H} \right\} \right] \quad (2.46)$$

Coull and Irwin (1969) also presented graphs for obtaining values for maximum shear force coefficient K_1 and K_2 (Fig. 2.18), for uniformly distributed load and for triangular load (Fig. 2.19). The curves are generally applicable to any wall with one or two symmetrical bands opening and non-uniform thickness as well as applied to any cross-sectional shape of connecting beam or slab and walls.

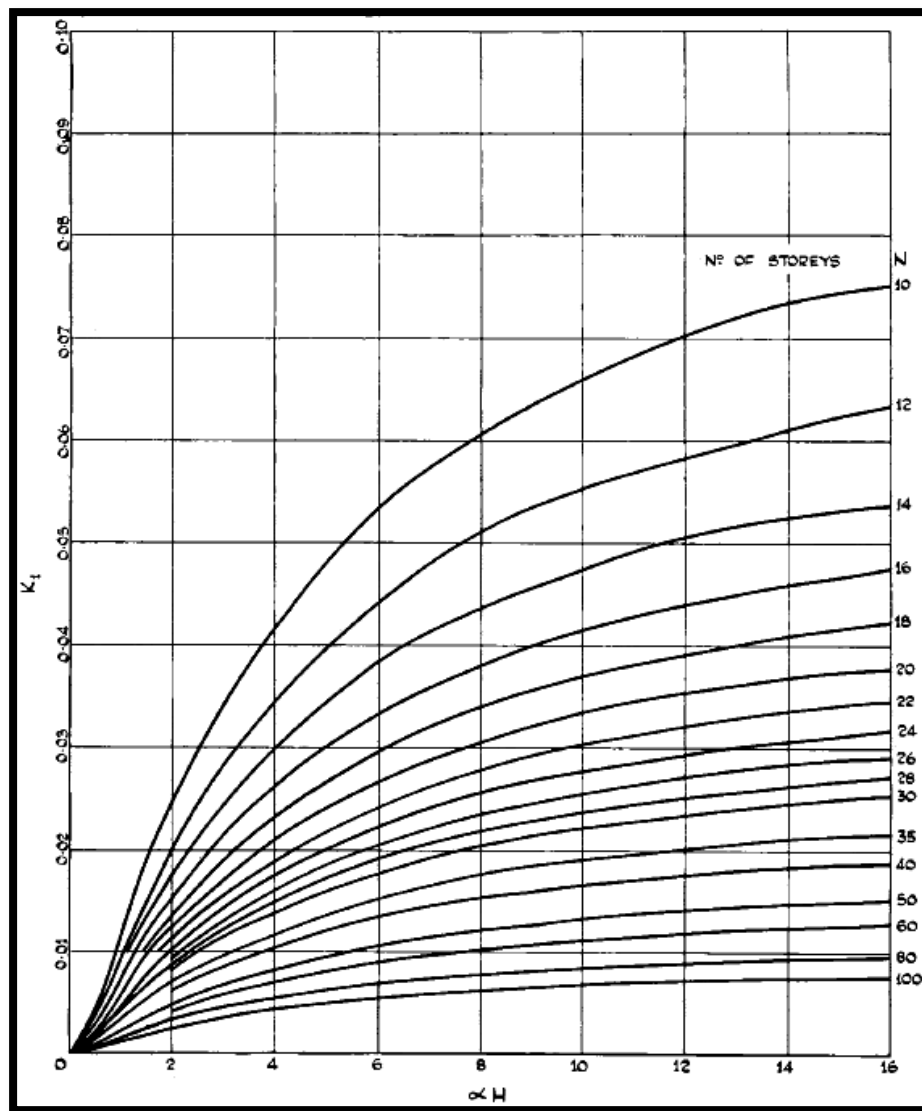


Figure 2.18: Coefficient of maximum shear force K_1 for uniformly distributed load
(Coull and Irwin 1969)

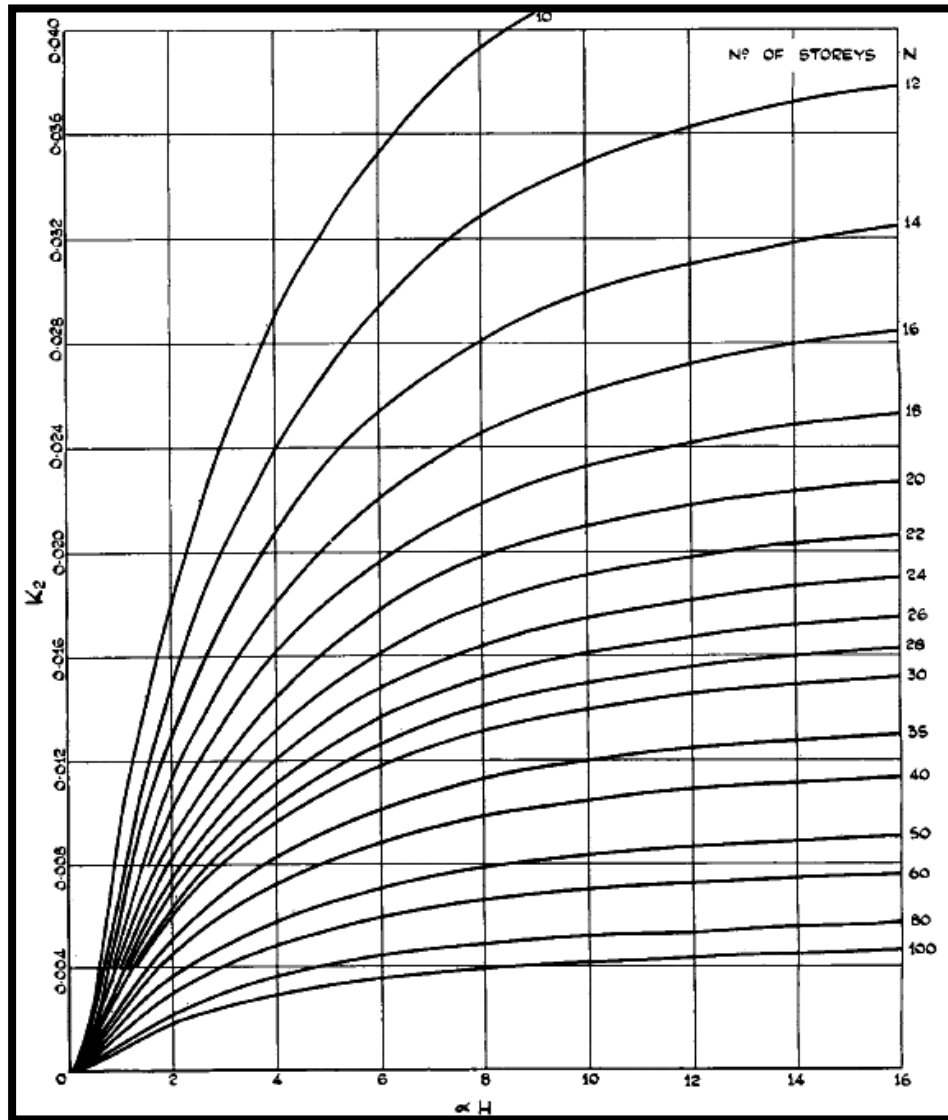


Figure 2.19: Coefficient of maximum shear force K_1 for uniformly distributed load
(Coull and Irwin 1969)

2.5.1.4 Physical Interpretation of Design Parameters

It is important to interpret design parameters such as α and μ on which the design curves for coupled shear wall system depend. Coull & Choudhury (1967b) alternatively expressed the values of α and μ for design purposes as:

$$\mu = 1 + \frac{1}{2} \left(\frac{d_1 + d_2}{d_1 d_2} \right) \left(\frac{d_1^3 + d_2^3}{l^2} \right) \quad (2.47)$$

$$\alpha = \sqrt{\mu} \left\{ \left(\frac{144}{hb^3} \right) \left(\frac{I_p}{t_w} \right) \left(\frac{l^2}{d_1^3 + d_2^3} \right) \right\}^{1/2} \quad (2.48)$$

$$l = \frac{1}{2} (2b + d_1 + d_2)$$

Where, d_1 and d_2 are the width of the walls and t_w is the thickness of the wall.

Since a number of dimensions are involved, it is convenient to consider a single corridor opening (b) which is commonly used in modern apartment building around 6 to 8 ft (1.82 to 2.43 m) and the height of the storey should be kept commonly around 8.5 to 9.5 ft (2.5 to 2.89 m). The width of the building will generally lie within the range of 45 to 70 ft (13.716 to 21.33 m). If the wall width is equal the sum and lie between 40 to 64 ft (12.19 to 19.50 m), so the value of μ for these both extremes are 1.98 and 1.236, a variation of ± 1.6 percent from the mean, and if it is unequal the value of μ lies between 1.295 to 1.353, a variation of ± 2.2 percent from the mean. Thus, although the small variations in μ may have a considerable influence on the magnitude of maximum deflections, the values of μ will not affect greatly on the value of α which is directly proportional to $\sqrt{\mu}$.

In tall building structure with coupled shear wall, floor slab is 6 to 8 inch (150 to 200 mm) thick and effective width Y_e lies between 20 to 24 ft (6.09 to 7.31 m), the range of I_p should be around 0.21 to 0.59 ft⁴, thickness of wall lies t_w between 12 to 24 inch (0.304 to 0.609 m), and $\left(\frac{I_p}{t} \right)^{\frac{1}{2}}$ varies between 0.32 and 0.77 commonly. The values of α in equal walls is 0.0622 to 0.0459 $\left(\frac{I_p}{t} \right)^{\frac{1}{2}}$ and in unequal walls ($d_1=2d_2$) is 0.0558 to 0.0412 $\left(\frac{I_p}{t} \right)^{\frac{1}{2}}$.

Table 2.1 indicates that a movement of the corridor opening away from the center of the wall tends to decreases the parameter αH . Also with distributed lateral loads, the position of maximum shear force in the connecting system tends to travel to a higher level, with the same tendencies are found when the wall thicknesses increases, and the stiffness of connecting medium decreases. In all situations, K_4 increases with the increase of stiffness parameter αH .

By taking possible height range of 100 to 300 ft (30 to 90 m), the value of stiffness ' αH ' can be evaluated from Table 2.1 as suggested by Coull and Choudhury (1967b).

Table 2.1: Variation of parameter αH for shear wall structure (Coull and Choudhury 1967b)

	αH Range							
	Height H = 100 ft				Height H = 300 ft			
Width of Building	46 ft		70 ft		46 ft		70 ft	
$(I_p / t)^{1/2}$	0.32	0.77	0.32	0.77	0.32	0.77	0.32	0.77
Equal Walls ($d_1 = d_2$)	2.00	4.79	1.47	3.54	6.00	14.37	4.41	10.62
Un Equal Walls ($d_1 = 2d_2$)	1.79	4.30	1.32	3.17	5.37	12.90	3.95	9.51

2.6 Role of Reinforced Concrete in the Coupled Shear Wall Structures

Reinforced concrete (RC) plays very vital role in the structural strength, stiffness and ductility of coupled shear wall structures under gravity and lateral loading. For decades, normal concrete was normally used with steel reinforcement in such highly reinforced structures. Numerous research studies have been conducted in the past to investigate the behaviour of coupled shear walls with normal concrete highlighting bending stiffness and effective width of floor/coupling slabs having different wall geometry (Qadeer and smith 1969; Coull and Wong 1981, 1983, 1984, 1990; Hossain 2003; Coull and Irwin 1969; Coull and Choudhury 1967a, b).

Hossain (2003) studied the non-linear flexural behaviour of coupled shear wall structures using reinforced micro-concrete by testing small scale models of $1/12^{\text{th}}$ scale. The influence of geometric parameters on flexural stiffness and effective width in pre-cracking, cracking and post-yielding stages of reinforced micro-concrete was investigated. The proposed use of high performance concretes (HPCs) such as Self-Consolidating Concrete (SCC) and Engineered Cementitious Composite (ECC) will significantly improve the process of casting through self-consolidation and quality of construction as well as improve the strength, ductility and durability of coupled shear wall system.

2.6.1 Self-Consolidating Concrete (SCC)

Self-Consolidating Concrete (SCC) is a highly flowable concrete that can flow into place under its own weight. This will achieve high-quality consolidation without any kind of machine vibration and also without defects due to bleeding or segregation. It can be used to improve the productivity of casting congested sections and also to insure the proper filling of restricted areas with minimum or no consolidation (Khayat 1999). This type of concrete will improve the working environment by eliminating the noise pollution caused by vibrators and reduces instrumental and labour cost.

SCC was developed in Japan in the early 1980's (Hayakawa et al. 1993). Major factor to develop this kind of concrete to accommodate flowability under highly reinforced structural members in such high intensity seismic Areas in Japan, and reduce cost in terms of time and highly skilled labour, to fill highly reinforced concrete members with conventional normal concrete with large size of the aggregates.

This can be developed through different approaches. First method is to increase significantly the amount of fine materials such as fly ash, volcanic ash and slag cement without changing the water content compared to common concrete. (Hossain and Lachemi 2010) Secondly to design SCC is incorporating a Viscosity Modifying Admixture (VMA) to improve the stability of the SCC. (Lachemi et al. 2003) This kind of admixtures commercially available in the local markets but eventually this is costly and increases the price of SCC. VMA are water soluble polymers which improve the ability of cement paste to keep its constituents in suspension and also increase the viscosity of the mixture. Using the VMA with super-plasticizers can ensure adequate workability without segregation.

Bouzoubaâ and Lachemi (2001) evaluated the SCC made of high volumes of Class F fly ash. Nine SCC mixtures and one control concrete were studied. The content of the cementitious materials was maintained constant (400 kg/m^3), while the ratio of water/cementitious material ranged from 0.35 to 0.45. The self-compacting mixtures had a cement replacement of 40%, 50%, and 60% by Class F fly ash. Tests were performed on all mixtures to obtain the properties of fresh concrete in terms of stability and viscosity. The SCCs developed 28-day compressive strengths

ranging from 26 to 48 MPa. The results showed that an economical SCC could be successfully developed by incorporating high volumes of Class F fly ash.

Lachemi et al. (2003) studied twenty-one concrete mixtures to investigate the performance of three types of SCC manufactured with fly ash, slag cement, and various VMAs based on mechanical properties and also on cost. Fly Ash SCC mixtures had cement replacement of 40%, 50%, and 60%, while slag cement SCC mixtures had 50%, 60%, and 70% replacement. The water-cementitious material ratios (w/cm) ranged from 0.35% to 0.45%. Three different VMAs were used in VMA SCC mixtures with w/cm of 0.45%. Tests were carried out on all mixtures to obtain mechanical properties such as compressive strength. The results indicated that an economical SCC with desired properties could be successfully developed by incorporating FA, slag cement, or VMA. It was found that these SCC could replace the control concrete and could be more economical (30% to 40% in case of FA and slag cement). Although the cost of VMA SCC was slightly higher than those with FA and slag cement, it had more resistance to segregation and had higher early strength development.

2.6.2 Engineered Cementitious Composites (ECC)

Engineered Cementitious Composite (ECC) is a class of ultra-ductile fiber reinforced cementitious composites. ECC has been systematically engineered over the last years to achieve high ductility under tensile and shear loading (Li 1998; Li 2003; Li et al. 2001; Sahmaran et al. 2009, 2011). ECC was originally developed at the University of Michigan in the early 1990s (Li 1993). ECC is characterized by high ductility in the range of 3% to 7%, tight crack width of around 60 μm and relatively low fiber content of 2% or less by volume. The typical fiber used in ECC is the polyvinyl alcohol (PVA) fiber with a diameter of 39 μm and a length of 6–12 mm.

This strain capacity is realized through the formation of many closely spaced micro cracks, allowing for a strain capacity over 300 times than that of normal concrete. These cracks, which carry increasing load after formation, allow the material to exhibit strain hardening, similar to many ductile metals. Under severe bending loads, an ECC beam deforms similar to a ductile metal plate through plastic deformation as shown in Fig. 2.21, so it is also called “bendable concrete” (Li

2011). In compression, ECC materials exhibit compressive strengths similar to high strength concrete (e.g. greater than 60 MPa) (Lepech and Li 2007a).



Figure 2.20: Extreme flexure capabilities of ECC under a large bending load (Li 2011)

A typical uni-axial tensile stress-strain curve of ECC containing 2% PVA fiber (Weimann and Li 2003) is shown in Fig. 2.20. The characteristic strain hardening after first cracking is accompanied by multiple micro cracking. The crack width development during inelastic straining is also shown in Fig. 2.21. Even at ultimate load, the crack width remains less than about 80 μm . Unlike normal concrete or fiber reinforced concrete (FRC), the steady-state crack width is an intrinsic material property, independent of loading (tension, bending, or shear) and steel reinforcement type and amount. This observation has important implications in service life, economics, and architectural aesthetics. In short, where steel reinforcement is used to control crack width in concrete, such steel reinforcement can be completely eliminated in ECC.

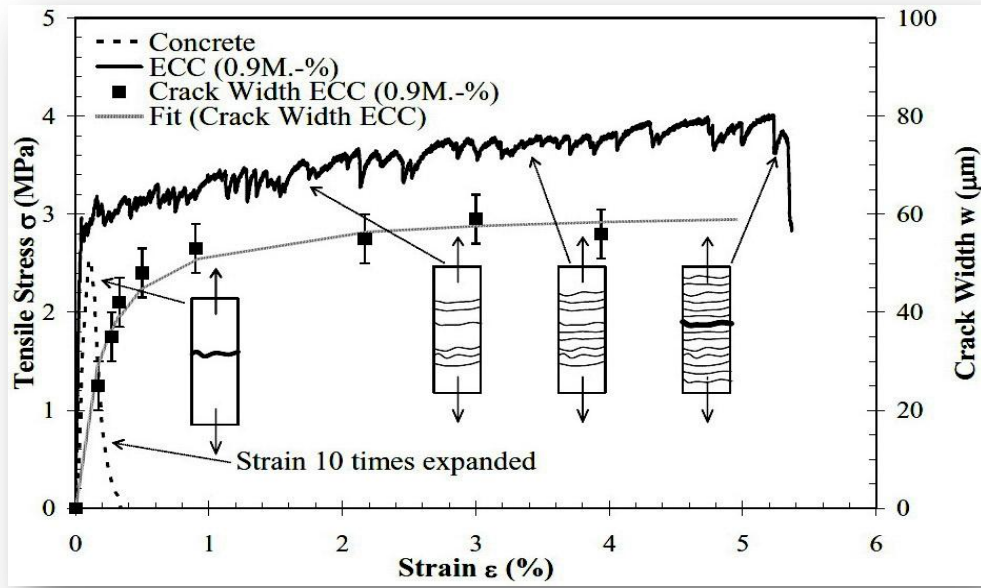


Figure 2.21: Typical tensile stress-strain curve and crack width development of ECC

(Weimann and Li 2003)

Although the components of ECC may be similar to Fiber Reinforced Concrete (FRC), the typical ECC characteristic of strain hardening through micro cracking is achieved through micromechanical tailoring of the components (i.e. cement, aggregate, and fibers) (Li 1998; Lin et al. 1999), along with the control of the interfacial properties between components. Fracture properties of the cementitious matrix are carefully controlled through mix proportions. Fiber properties, such as strength, modulus of elasticity, and aspect ratio have been customized for use in ECC. The interfacial properties between fiber and matrix have also been optimized in cooperation with the manufacturer for use in this material. Typical mix proportions of ECC using a polyvinyl alcohol (PVA) fiber are given in Table 2.2. All proportions are given with materials in the dry state.

Table 2.2: Engineered cementitious composite typical mix design proportions (Nawy 2008)

Cement	Fly Ash	Sand	Water	(HRWRA)*	Fiber (Vol. %)
1.0	1.2	0.8	0.56	0.012	0.02
* High-Range Water Reducer Admixture					

While most high performance FRCs rely on a high fiber volume to achieve high performance, ECC uses low amounts of discontinuous fiber which is greater than the calculated critical fiber content required to achieve strain hardening. This low fiber volume along with the common components, allows flexibility in construction execution. Various fiber types have been used in the production of ECC. Typical ECC mixtures use Poly-Vinyl Alcohol (PVA). The PVA fiber is surface coated by an oil agent (1.2% by weight) to reduce the fiber/matrix interfacial bonding. The mix design described in Table 2.2 has been experimentally demonstrated in a broad range of investigations to consistently produce good ECC fresh and hardened properties. Adaptations of this reference mix have been used in various construction projects. Full-scale production of ECC was carried out in Japan (Kunieda and Rokugo 2006) and in the United States (Lepech and Li 2007a). Experience in concrete ready-mix plants suggests the charging sequence of raw material shown in Table 2.3.

Table 2.3: Material charging sequence into ready-mix trucks (Nawy 2008)

No.	Activity	Elapsed Time (min)
1	Charge all sand.	2
2	Charge approximately 90–95% of mixing water, all HRWR, all hydration stabilizers.	2
3	Charge all fly ash.	2
4	Charge all cement.	2
5	Charge remaining mixing water to wash drum fins.	4
6	Mix at high RPM for 5 minutes or until material is homogenous.	5
7	Charge fibers.	2
8	Mix at high RPM for 5 minutes or until material is homogenous.	5
Total		24

2.6.2.1 Applications of ECC

ECC is designed for several types of engineered applications, other than ECC large-scale on site construction applications, and it is designed for high-early-strength ECC applications that require rapid strength gain to quickly reopened transportation to the motorist public (Wang and Li 2006), Lightweight ECC applications to minimize the dead load of structural members (Wang and Li 2003), Green ECC applications to maximize material greenness and infrastructure sustainability (Lepech et al. 2007b) and Self-healing ECC applications to heal cracks after experiencing damages (Li and Yang 2007; Yang et al. 2005). Although the design of ECC is involved in different types of construction applications, the development of ECC is still evolving and even broader ranges of its properties have developed in the future as needed.

Members made of ECC in combination with steel plates provide higher flexural resistance with a thinner cross section than normal steel-concrete members. Fig. 2.22 (left) shows the Mihara Bridge in Hokkaido, Japan with a bridge length of 972 m and central span of 340 m (Mitamura et al. 2005).



Figure 2.22: Left Overview of Mihara Bridge (Mitamura et al. 2005) and right labour repairing Mitaka Dam with ECC for water-proofing (Kojima et al. 2004)

Over 60 year old the Mitaka Dam in Hiroshima-Prefecture, Japan in 2003 (Kojima et al. 2004), with several damaged concrete surface repaired with ECC. Cracks, spalling, and water

leakage were concerns that prompted the use of ECC by spraying as a water-tight cover layer of 20 mm thick at upstream over 600 m², as shown in Fig. 2.22 (right).

Concrete Retaining wall in Gifu, Japan repaired using ECC in 2003, sizes 18 m in width and 5 m, constructed in the 1970s (Rokugo et al. 2005) as shown in Fig. 2.23. Ordinary Portland cement could not be used due to the severity of the cracking in the original structure, which would have caused reflective cracking. ECC was intended to minimize this danger; after one year only micro cracks of tolerable width were observed. Cracking was harder to observe 24 months after repair compared to 12 months after, being hidden by dirt accumulated on the surface.



Figure 2.23: Surface preparation with high-pressure water jet repair of concrete retaining wall (Rokugo et al. 2005), upper left before repairing and right after repairing

As one of the first field applications of ECC in the USA, an ECC patch repaired and replaced the deck of the Curtis Road Bridge in Michigan, US in 2002, (Li and Lepech 2004). In addition to bridge deck patching repairs, the most recent field application of ECC in the USA with a bridge “link slab” completed in cooperation with MDOT on Grove Street Bridge in Southeast Michigan in 2005 (Lepech and Li 2007a). The objective was to eliminate the maintenance requirements associated with typical bridge deck expansion joints. In this project, about 32 m³ of ECC were cast in place using standard ready-mix concrete trucks to build the first ECC link slab in US. With a strain capacity exceeding 2%, these composites can be used to replace traditional steel expansion devices and can fully accommodate the thermal deformations of adjacent bridge spans. This ECC link slab design was adopted in 2006 in the highway segment that extends from Bolzano to the Austrian border bridge in north Italy. Currently research is in progress at Ryerson University, Canada on the application of ECC link slabs in joint-free bridge deck construction (Sherir 2012; Mavani 2012).

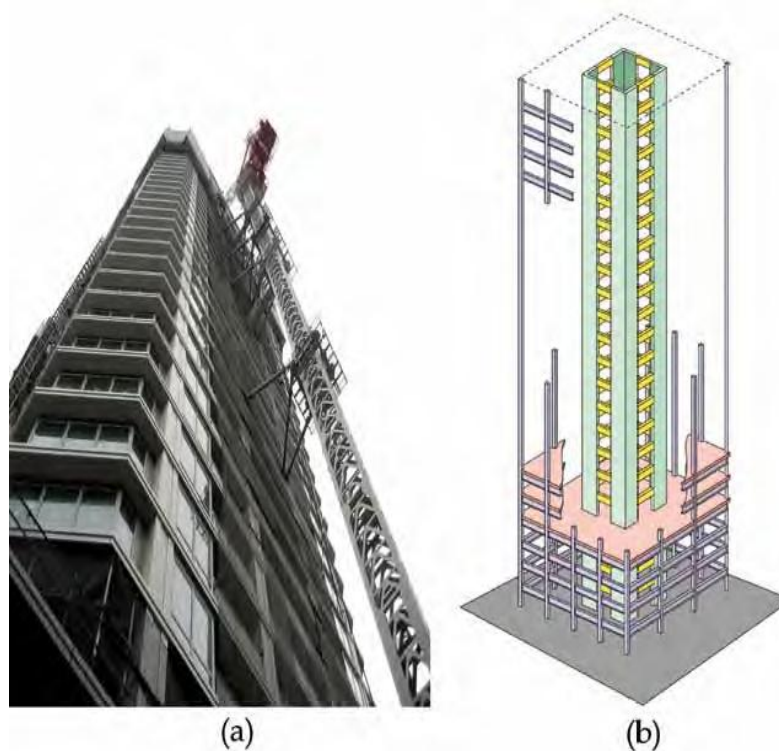


Figure 2.24: (a) The Nabeaure Tower in Yokohoma, Japan building with pre-cast coupling beams and (b) Schematics view showing coupling beams (in yellow) on each floor (Maruta et al. 2005)

In high rise building, in Japan ECC has been used in structural applications as coupling beams (Maruta et al. 2005). Due to the high energy absorption capacity of R/ECC, the application of this material in coupling beams in shear wall system, which connect adjacent core walls, and it is very useful for high rise buildings in high intensity Seismic regions. The recent development of precast ECC coupling beam elements by Kajima Corporation in Japan can be easily integrated into current seismic construction practices. Currently two high-rise buildings in Tokyo, Japan have been built integrating ECC coupling beams, Fig. 2.24.

2.7 Summary and Conclusion

The analysis of non-linear coupling action of the slab in coupled shear wall system is described based on previous research studies. It is observed and concluded that all Researcher's or investigator's uses different approaches to study the relative influences of material and structural parameters. The variation of stresses and strain in the slab and modes of failures are investigated in details. It is found that the behaviour of coupling slabs in pre-cracking, cracking and post-yielding stages depend upon its material properties and geometric parameters of the shear wall such as wall opening (corridor opening), length and width of the slab. Researchers produced design charts and equations for finding bending stiffness and effective width of the slabs that can be used for design purposes. Analysis of coupled shear walls using continuous medium method is also described in detail.

To date, however, no research has been conducted on the effect of high performance concrete especially Engineered Cementitious Composite (ECC) on the strength, stiffness and ductility of the coupled shear wall system. Application of ECC will greatly enhance the strength, stiffness and ductility of the coupled shear wall structures. The knowledge of the structural behaviour of such structural system with ECC is very important in developing analytical models and design aids to predict the strength, stiffness and ductility of the overall system as well as bending stiffness/effective width of coupling slab. Such models/design aids can be useful to develop design guidelines for shear wall system with ECC coupling slab used in practical construction applications. Proposed research on the flexural behaviour of coupling slabs in shear wall structures incorporating HPCs such as ECC and Self-Consolidating Concrete (SCC) is a timely initiative and is warranted.

CHAPTER 3

EXPERIMENTAL SETUP, MODEL PROPERTIES, INSTRUMENTATION AND TESTING

3.0 Introduction

This chapter describes the development of a test set-up and its working principle to carry out small scale model tests of 1/12th scale simulating flexural behaviour of coupling slabs in shear wall structures. It also describes testing procedures, model instrumentations, geometric dimensions of models, design of reinforcement, mix design/material properties of ECC and SCC, steel properties and casting/curing of model specimens.

3.1 Simulation of Non-linear Flexural Behaviour of Coupling Slab and Working Principle of Test Set-up

The behaviour of coupling slab in CSW system in resisting lateral forces is described in Chapter 2 under section 2.1. A schematic of the experimental set-up and its working principle are presented in the Fig. 3.1. One leg (wall) of the test model is fixed to the fixed platform through base plate-fixing angle assembly while the other leg was fixed in a similar manner to the movable/free platform. Upward load (Q), was then applied through hydraulic cylinder at the movable end and corresponding vertical deflection (δ), of the platform was monitored. The load (Q), was applied through the centre of the wall incrementally until failure of the slab to get complete (Q - δ) and hence, moment-rotation (M - θ) responses as shown in Fig. 3.1. Moment diagram shows the development of maximum moment at the wall centre and zero moment at the middle of corridor opening representing an inflexion point as described in Continuous Medium Method Approach (Coull and Choudhury 1967a,b; Hossain 2003).

The model tests provided information on the strength, stiffness and modes of failure of the system. From Q - δ and M - θ responses, the behaviour of slab in pre-cracking to post-yielding stages of CSW system were analyzed to derive flexural/bending stiffness ' k ', and effective width of coupling slab (Y_e) by using the equations derived in Chapter 2 and incorporating geometrical and material parameters of the test specimens.

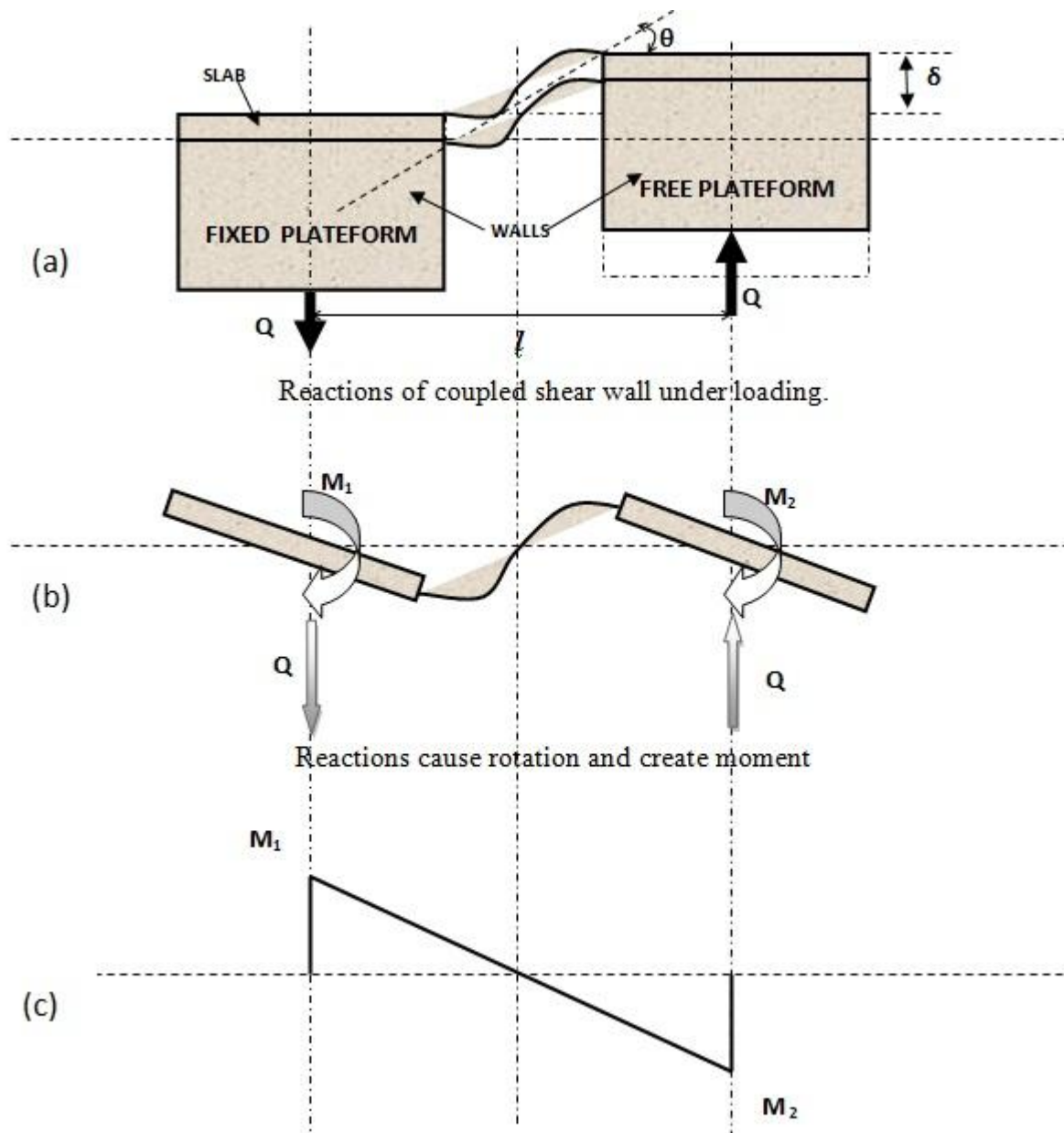


Figure 3.1: Working principle of test-set-up and behaviour of coupling slab

3.2 Geometry of Model Test Specimens

Six small scale model tests of approximately 1/12th scale of CSW building had been carried out to investigate the general behaviour of the system and to study the effect of geometric parameters. The test had been conducted for a particular value of Y/X (0.6) with L/X of 0.3, 0.4 and 0.6. Two high performance concretes (HPCs) namely SCC and ECC were used to make the specimens. Three model tests were conducted for each concrete. This experimental investigation was carried out by keeping constant values of the width (Y) (600 mm) and length (X) (1000 mm) of the slab and using three different values (350 mm, 300 mm and 200 mm) of corridor opening (L or b). The wall (t_w) and slab (t) thickness were kept constant at 60 mm. Both walls had equal width ($W_1 = W_2$). Detailed dimensions of the models and geometric ratios (L/X and Y/X) are presented in Table 3.1. The model specimen designated as for example 'ECC350' or 'SCC350'. The letters in the model designation represents type of HPC and numerics represent the width of the wall in mm. All geometric dimensions of the model specimens are presented in Figs. 3.2 and 3.3.

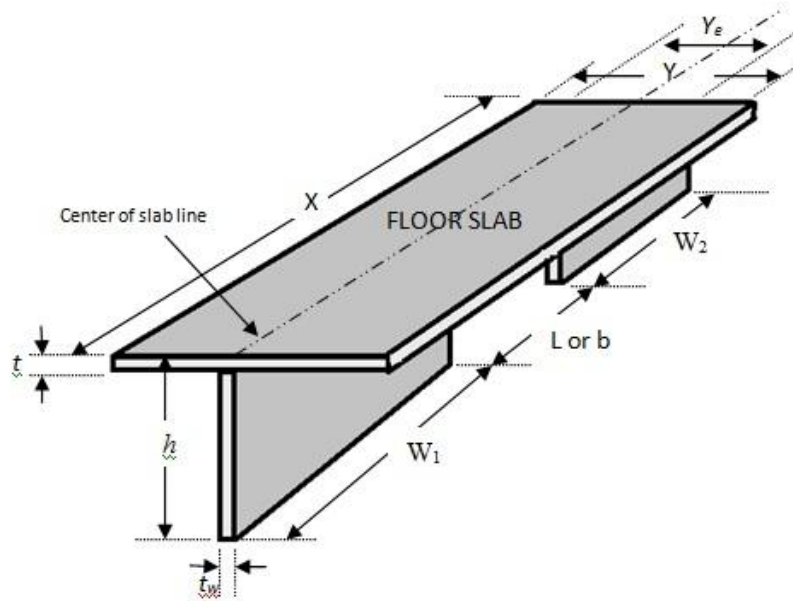


Figure 3.2: Isometric view of coupled shear wall, showing geometric parameters

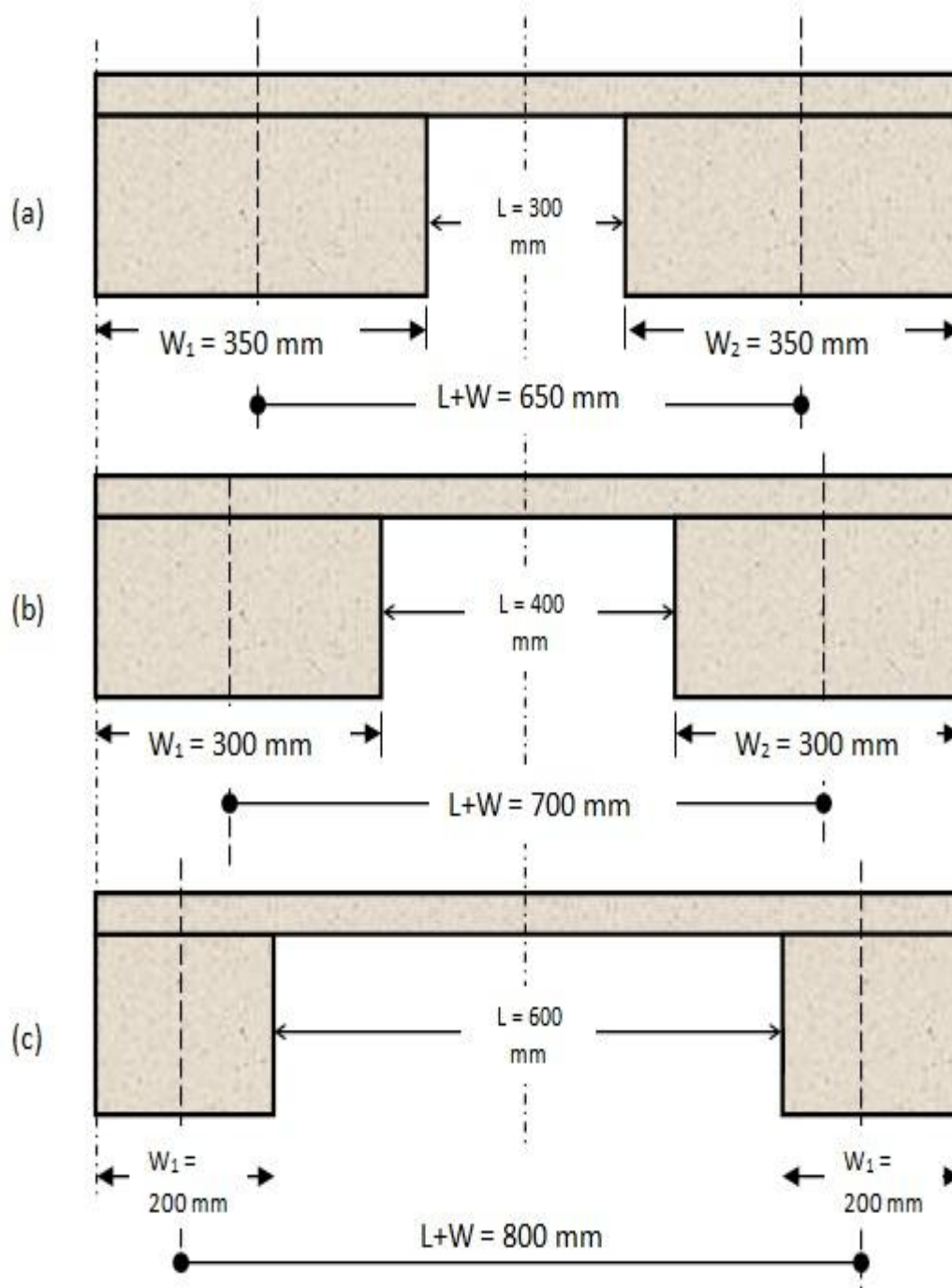


Figure 3.3: Three different assemblies showing geometric parameter

Table 3.1: Geometrical parameters of model test specimens

Model	Y/X	L/X	Length of Slab (X) (mm)	Width of the slab (Y) (mm)	Width of the wall (W) (mm)	Thickness of slab (t) (mm)	Wall thickness (t_w) (mm)	Corridor Opening (L) (mm)
ECC350	0.6	0.3	1000	600	350	60	75	300
ECC300		0.4	1000	600	300	60	75	400
ECC200		0.6	1000	600	200	60	75	600
SCC350		0.3	1000	600	350	60	75	300
SCC300		0.4	1000	600	300	60	75	400
SCC200		0.6	1000	600	200	60	75	600

3.3 Material Properties and HPC Mix Design

3.3.1 Tests on Mechanical Properties of Concrete

Mechanical properties of the concrete used in experimental studies were determined by means of compressive strength (f_c') and flexural strength (f_r). The concretes were cast in the moulds without using any vibrators or compactors. Four specimens from each batch were tested for the hardened properties at the standard age of 28 days.

3.3.1.1 Compressive Strength

The 28-day average compressive strength was obtained from 100 mm x 200 mm cylinders for SCC and ECC as per ASTM C109/C109 M (2011). Minimum three specimens were prepared for each of ECC and SCC. The average compressive strength (f_c') test results of each specimen are tabulated in table 3.2 of ECC and SCC.

3.3.1.2 Flexural Strength

To check the flexural strength of concrete, a four point bending test was performed on control beam specimens under load displacement control condition at a loading rate of 0.005 mm/s on a closed loop controlled servo hydraulic material test. For each mix, three beam specimens, 355 x 76 x 50 mm in size were prepared and tested after 28 days. The load was applied at the mid span of the beam. During test the load (p) in MPa and the mid span deflection were recorded on computerized data recording system. The formula to find the flexural strength (f_r) is expressed as:

$$f_r = \frac{pL}{bd^2} \quad (3.1)$$

Where, p = load in N; L = span length = 304 mm; b = width of the beam = 50 mm and d = height of the beam = 76mm.

The tensile strength (f_r) of ECC and SCC for six model CSW specimens is shown in Table 3.2.

Table 3.2: Type and strength of concrete for each specimen (28 days)

<i>Specimen No.</i>	<i>Concrete Type</i>	<i>Concrete strength (Mean Value) MPa</i>	
SCC350	SCC	Compressive strength (f_c')	44
		Tensile strength (f_r)	3.80
SCC300	SCC	Compressive strength (f_c')	38
		Tensile strength (f_r)	3.35
SCC200	SCC	Compressive strength (f_c')	44
		Tensile strength (f_r)	3.03
ECC350	ECC	Compressive strength (f_c')	41
		Tensile strength (f_r)	4.55
ECC300	ECC	Compressive strength (f_c')	36
		Tensile strength (f_r)	4.30
ECC200	ECC	Compressive strength (f_c')	39
		Tensile strength (f_r)	4.10

3.3.2 Modulus of elasticity of ECC and SCC

To obtain the value of modulus of elasticity of ECC and SCC, two cylinder (100 mm x 200 mm) samples were also cast. These cylinders were then tested at 28 days for measuring the modulus of elasticity. Three single strain gauges were attached to the longitudinal direction of the cylinder. The length of the strain gauges was bigger than five times of the maximum aggregate size of concrete. The secant modulus of elasticity of ECC was determined from the compression test of two cylinder ECC and SCC samples. The average slope of the three strain-stress curves at the linear stage ($0.4 f_c'$) for the first and second sample was 24,500 MPa and 24,980 MPa, respectively for ECC, as shown in Figs. 3.4 and 3.5.

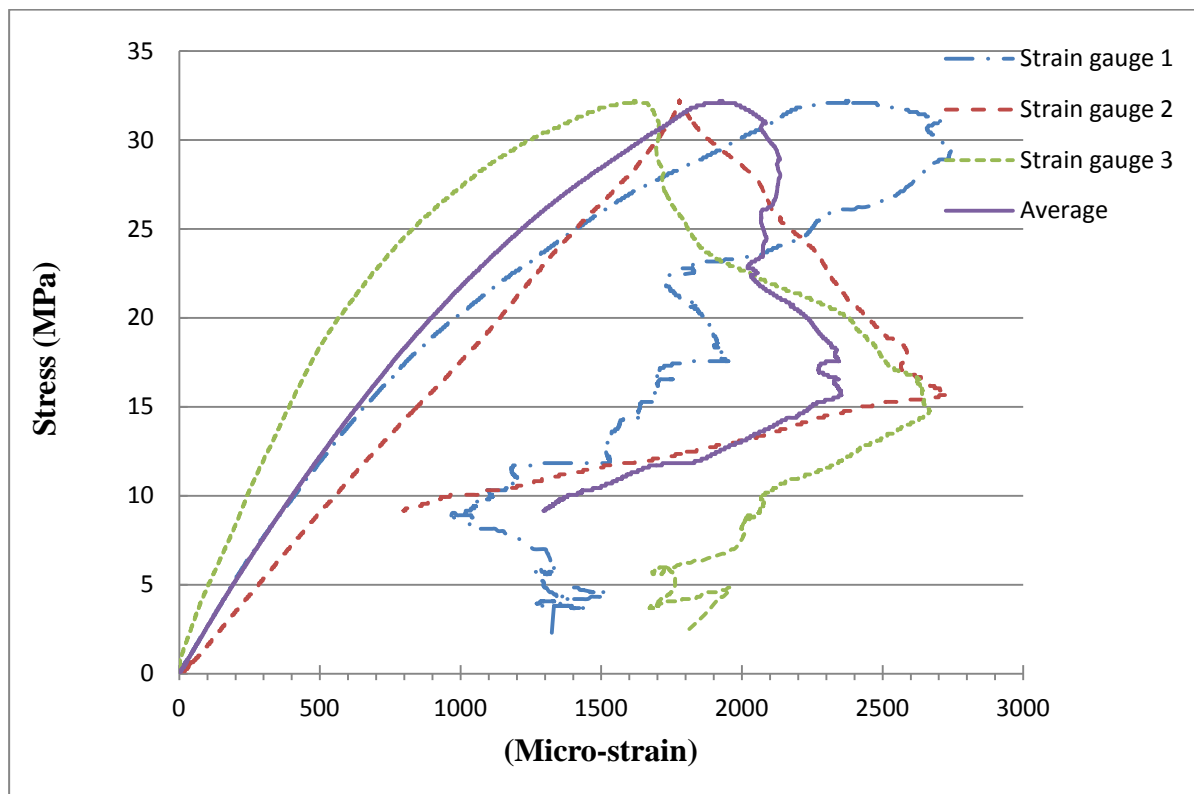


Figure 3.4: The result of the first test for the modulus of elasticity (Average $E = 24,500$ MPa)

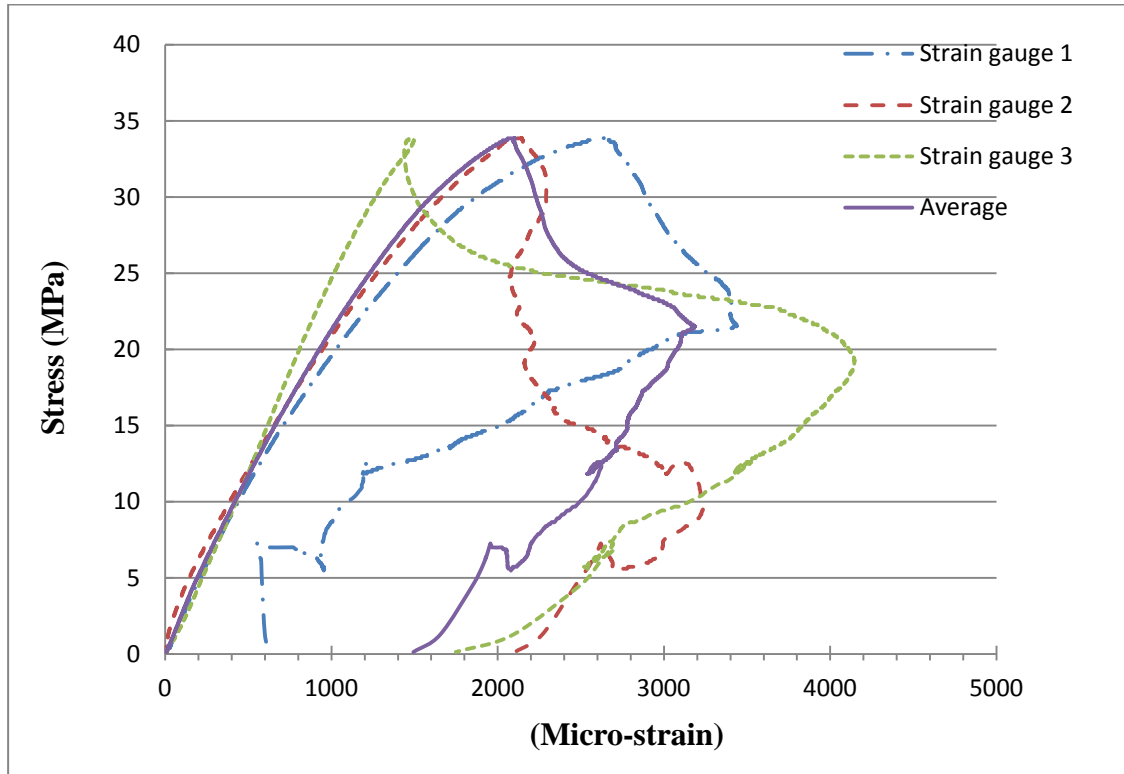


Figure 3.5: The result of the second test for the modulus of elasticity (Average $E=24,980$ MPa)

The ECC and SCC of modulus of elasticity from the two tests and the average ($E = 24,740$ MPa) and ($E = 32,130$ MPa) values are presented in Table 3.5.

Table 3.3: Modulus of elasticity (E) for the ECC and SCC

Specimen No.	The average E_{ECC} (MPa) based on the results of three strain gauge of ECC	The average E_{SCC} (MPa) based on the results of three strain gauge of SCC
1	24,500 MPa	30,670 MPa
2	24,980 MPa	33,590 MPa
Average	24,740 MPa	32,130 MPa

3.3.3 Reinforcing Steel Properties

Mild steel reinforcing bars of 4.75 mm diameter from the mesh reinforcement were used. Two bar samples of 400 mm length were tested under tension in the laboratory to determine yield stress, yield strain, ultimate strength and ultimate strain.

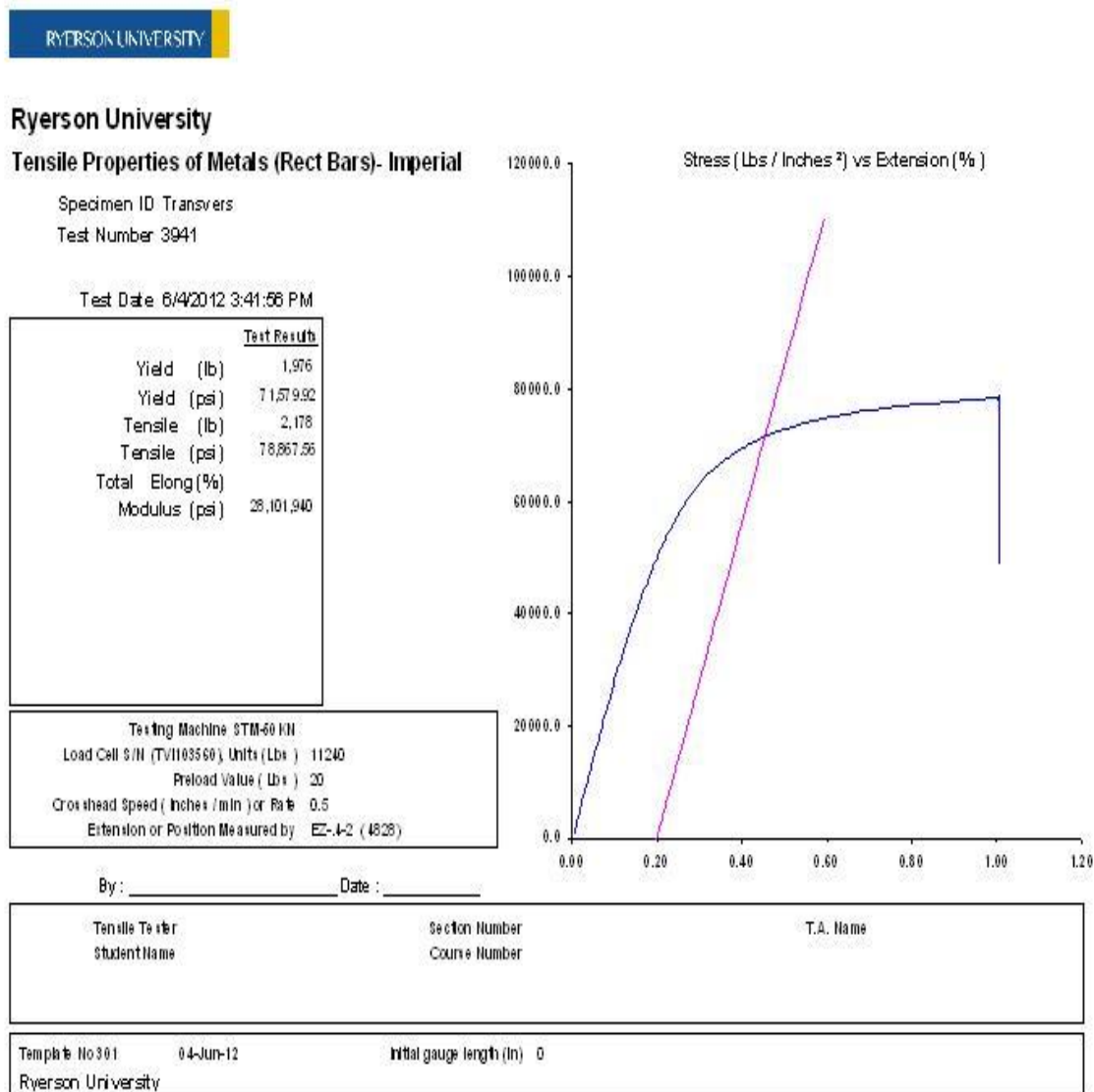


Figure 3.6: Tensile test results of steel bar # 3941

Ryerson University

Tensile Properties of Metals (Rect Bars)- Imperial

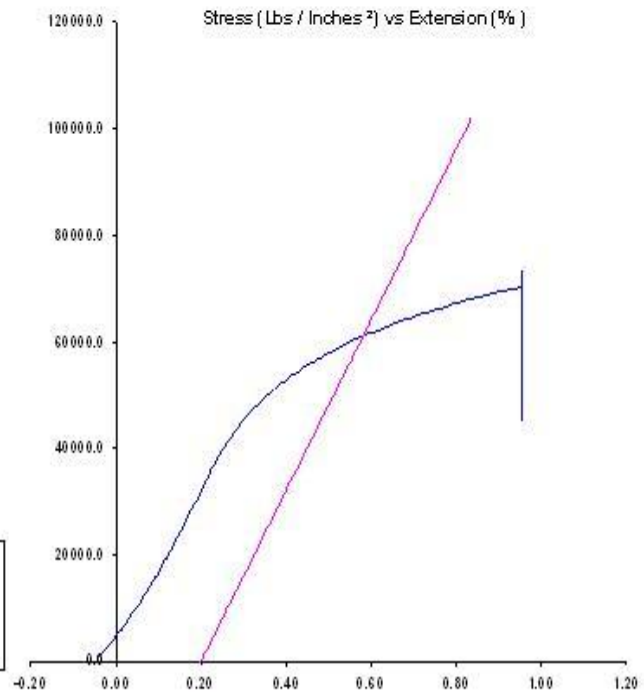
Specimen ID Transvers

Test Number 3939

Test Date 6/4/2012 3:36:13 PM

Test Results	
Yield (lb)	1,688
Yield (psi)	61,140.90
Tensile (lb)	2,030
Tensile (psi)	73,520.03
Total Elong (%)	
Modulus (psi)	16,044,670

Testing Machine STM-60 kN	
Load Cell S/N (TV1103560) Units (Lbs)	11240
Preload Value (Lbs)	20
Crosshead Speed (inches /min) or Rate	0.5
Extension or Position Measured by	EZ-4-2 (4828)



By : _____ Date : _____

Tensile Tester	United Testing Systems	Section Number	T.A. Name
Student Name	Rizwan	Course Number	

Template No 301	04-Jun-12	Initial gauge length (in)	0
Ryerson University			

Figure 3.7: Tensile test results of steel bar # 3939

Table 3.4: Table showing results of tensile test of steel bars

Test No	Yield Stress (f_y)	Ultimate Stress (f_u)	Modulus of elasticity (E_s)
	MPa	MPa	MPa
3941	493.52	543	193760
3939	421	506.9	110630.8
Average	457.26	524.95	152195.4

The results of the coupon tests for mild steel are shown in Figs. 3.6 and 3.7, respectively. The tensile testing machine gave the results in imperial units, so the Table 3.6 shows the results in both SI and Imperial units. The tension coupon results gave detailed information on the stress versus strain and modulus of elasticity of the mild steel bars used in mesh reinforcement. The average yield stress of 457 MPa, ultimate strength of 524.95 MPa, and modulus of elasticity of 152195.4 MPa were found. The usual range of modulus of elasticity for steel bars is from 200 GPa to 207 GPa (Yu 2000, ASTM-A36, 1986). Mild steel bars used in this study showed lower values of modulus of elasticity.

3.3.4 HPC Mix Design

Two types of concrete, namely; Self-Consolidating Concrete (SCC) and Engineered Cementitious Composites (ECC) were used to cast the coupled shear wall test models for experiment. All specimens were cast as per the guidelines for the concerned ASTM standard.

3.3.4.1 Self-Consolidating Concrete (SCC)

Type GU (General use type 10 Ordinary Portland cement) cement as per CSA A3001-03 (2003) from Lafarge Ltd. and type “S” slag cement were used. The coarse aggregate was crushed limestone from Munroe quarry with maximum size of 8 to 10 mm. Well graded coarse sand was used as fine aggregate. The High Range Water reducing Agent (HRWRA), ADVA® CAST 575, was used as Super-Plasticizer (SP) from Grace Products as an admixture to avoid adding extra water in the mix. And also one of the inherent properties of such HRWRA is to provide high early strength of concrete. The mix design and ingredients of SCC are shown in Table 3.5.

Table 3.5: Mixture proportions of SCC

SCC ingredients, kg/m ³					
Cement	Slag	Water	Coarse	Fine	HRWRA (SP)
400	90	172	750	910	1850

The volume of SCC needed for casting one CSW specimen with one time slump test and required control cylinders and beam specimens was around 80 liters. An industrial mixer having a maximum capacity of 300 liters was used so that one batch of 80 liters of concrete could be made easily.

Procedure for making SCC, the following mix sequences were carried out:

- The slag was added to the cement bucket and mixed with the cement (Fig. 3.8a).
- Sand and coarse aggregate were added to the concrete mixer and mixed for 15 second (Fig. 3.8b).
- The cement and slag were poured in the concrete mixer and mixed for 20 second.
- 60% of total water was added to the concrete mixer and mixed for 30 second.
- SP were added to the rest of the water. The remaining water were poured to the mixer and mixed for 1 to 2 minutes.
- Resume mixing for 2 minutes and check for required flowability.



(a)



(b)

Figure 3.8: Mixing the SCC ingredients; (a) Slag and cement (b) Sand and coarse aggregate

3.3.4.2 Engineered Cementitious Composite (ECC)

For making of ECC, the same industrial mixer was used; the weight of the super-plasticizer was measured by using digital scale with the accuracy of 0.01 grams for both SCC and ECC. The ECC mix design is presented in Table 3.6.

Table 3.6: Mixture properties of ECC

ECC ingredients, kg/m ³					
Cement	Fly Ash	Water	PVA Fiber	Silica Sand	HRWRA (SP)
386	847	327	26	435	3.7

Type GU cement (General use type 10 Ordinary Portland cement) from Lafarge and Class F fly ash supplied by Boral Materials Technologies were used for ECC mix. The Polyvinyl Alcohol (PVA) fiber of 8mm length and 39 μm in diameter was used. PVA fiber has attracted most attention due to the outstanding composite performance and economic consideration. The nominal strength of the PVA fiber was 1620 MPa and the density of 1300 kg/m³. Fiber was coated by hydrophobic oil (1.2% by weight) in order to reduce the fiber/matrix interfacial bond strength. The fiber content 2% by volume in excess of the calculated critical fiber content had been typically used in the ECC mix design (Li et al. 2001; Kong et al. 2003)

The silica sand with 110 μm average grain size and ADVA® CAST 575, a poly-carboxylate based high range water reducer from Grace Canada Inc as Super-Plasticizer (SP) were used. This SP is poly-carboxylic-ether type high range water reducer with solid content of approximately 30% and conforms to ASTM C 494 (2011) type F and ASTM C1017 (2007) type I.

80 liters of ECC was needed for a CSW model specimen and control specimens. Solid ingredients, including cement, fly ash and sand, were first mixed for a minute. Water and chemical admixtures (SP) were then added into the dry mixture and mixed for two minutes and then polyvinyl alcohol fiber was added at the end (Fig. 3.9a) and mixed for an additional three minutes.

The amount of SP was adjusted during the mix to have a uniform mixture and flowable ECC. The flowable ECC was poured to a small bucket for casting as shown in (Fig. 3.9b).



Figure 3.9: Making ECC

3.4 Design of Reinforcement for Models and Reinforcement Details

Small scale model specimens used in this study were similar to those used by Hossain (2003) where the reinforcements were calculated based on an equivalent static uniform wind load of 8.76 kN/m along the height of the building. The maximum wind shear, induced in the most highly stressed slab of a 20-storied coupled shear wall building having storey height of 3m and slab thickness of 200 mm, was calculated by using continuous medium method (Hossain 2003). The slab was then designed for reinforcement by applying maximum wind shear along the central contra flexure line. The percentage of reinforcements in the small scale test models were kept similar to those obtained in the prototype building. However, it should be noted that the amount of reinforcement in all the model slabs in this study was kept constant despite changes in geometric dimensions. So the maximum storey shear capacity (Q) was different for the coupling slab in various specimens although moment capacity remained same.

In all six model specimens, reinforcements in the form of mesh of 100 mm x 100 mm in size were provided in the manner as shown in Fig. 3.10.

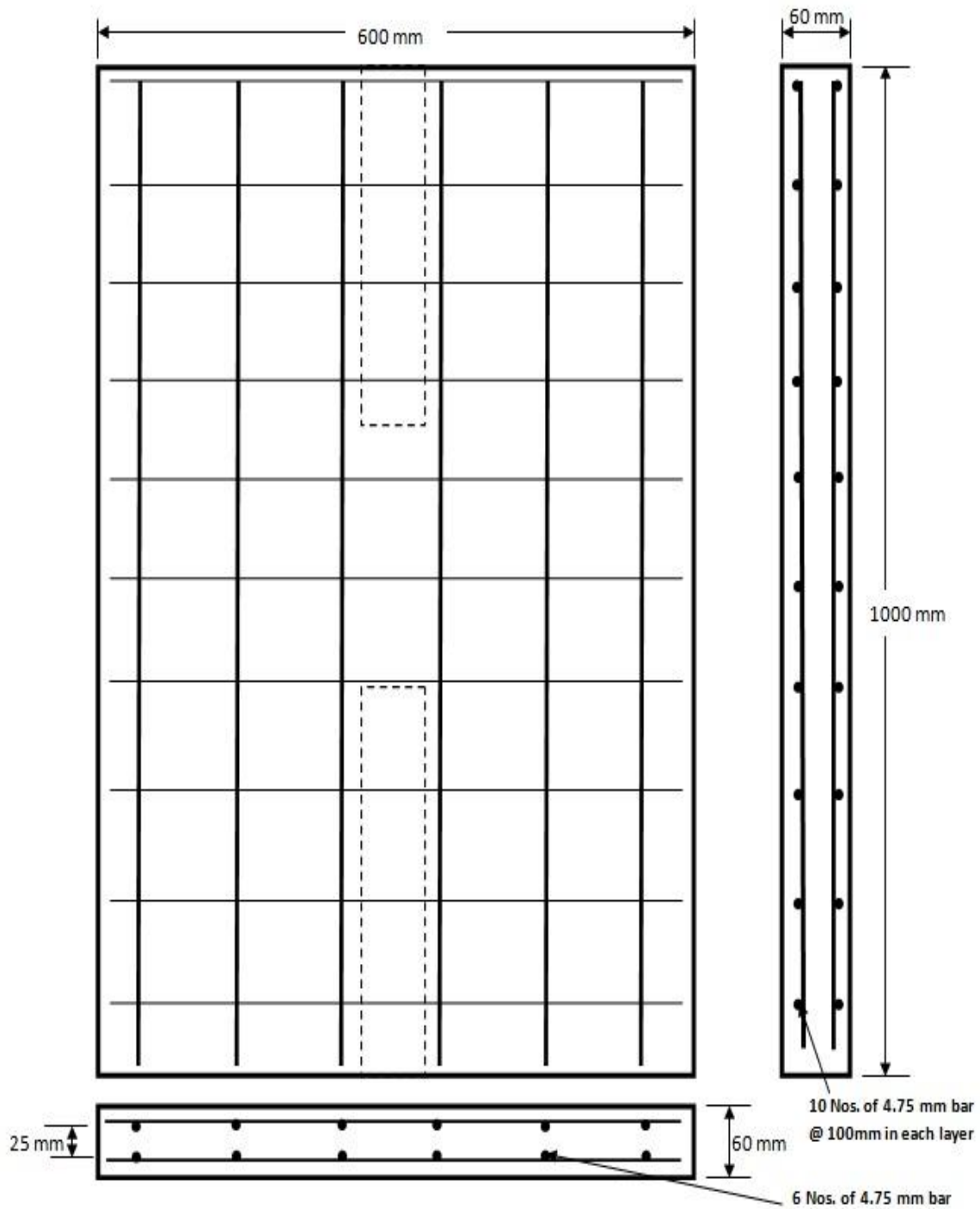


Figure 3.10: Reinforcements in the slab

Technical drawing showing the reinforcement detail for a wall and slab. The wall has a height of 250 mm and a length labeled "Wall length (W)". The slab has a thickness of 60 mm. The wall reinforcement includes 2 layers of 5 bars of 4.75 mm diameter at 50 mm center-to-center spacing. The slab reinforcement includes top and bottom bars. A 100 mm dimension is shown for the slab reinforcement. A 75 mm dimension is shown for the wall reinforcement. Labels include "Slab", "Wall", and "2 layers of 5 bars of 4.75 mm bar @ 50mm C/c".

68

3.5 Analytical Moment and Shear Capacities of Coupling Slabs in Model Specimens

The slab moment capacity under flexure was derived according to CSA A23.3-04 (2009) using rectangular stress block (as shown in Fig. 3.12).

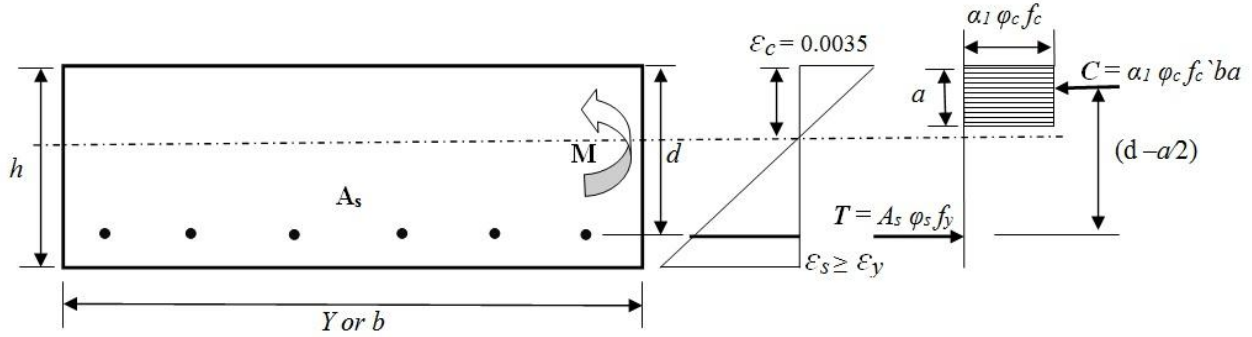


Figure 3.12: Rectangular stress block of rectangular slab

The equilibrium of compression (C) and tension (T) forces is used to determine 'a' as:

$$a = \frac{\phi_c A_s f_y}{\alpha_1 \phi_c f_c b}$$

Where; $\alpha_1 = 0.85 - 0.0015 f_c' \geq 0.67$

The moment resistance, M_r , developed by internal force couple, C and T, is therefore:

$$M_r = \phi_s A_s f_y \left[d - \frac{a}{2} \right]$$

By assuming $\phi_s = \phi_c = 1$, and taking certain geometric and physical parameters of two different materials with three different assemblies, f_c' of ECC = 39 MPa, f_c' for SCC = 42 MPa, $h = 60$ mm, $Y \text{ or } b = 600$ mm, $d = 45.62$ mm, $f_y = 457.26$ MPa, α_1 for ECC = 0.791 and α_1 for SCC = 0.787, we can get;

For ECC; $a = 2.607$ mm, $M_r = 2.154$ kN m, and

For SCC; $a = 2.435$ mm, $M_r = 2.159$ kN m

The both analytical resisting moments for SCC and ECC slabs are approximately same.

So assuming average Resisting Moment (M_r) = Factored Moment (M_f) = 2.157 kN m

So required amount of reinforcements should be calculated by;

$$A_{s,estimated} = \frac{M_f}{f_y 0.9 (0.9 h)} = \frac{2.157 \times 10^6}{457.26 \times 0.9 (0.9 \times 60)} = 97.062 \text{ mm}^2$$

6 bars of 4.75 mm diameter in one layer with c/c distance of 100 mm were provided as shown in Fig. 3.11. To check minimum steel requirements under CSA A23.3-04 (2009), by taking average $f'_c = 40.5$ MPa, we get:

$$A_{s,min} = \frac{0.2 \sqrt{f'_c} b h}{f_y} = \frac{0.2 \sqrt{40.5} 600 \times 60}{457.26} = 100.21 \text{ mm}^2$$

$$A_{s,min} = 100.21 \text{ mm}^2 < A_{s,provided} = 106.323 \text{ mm}^2 > A_{s,estimated} = 97.062 \text{ mm}^2$$

The analytical equivalent storey shear load resistance (Q_a) for the coupling slabs of model specimens is calculated based on the analytical moment resistance (M_r) and considering critical section at the junction of the interior edge of the shear wall. The analytical storey shear load resistance of all model ECC and SCC specimens are presented in Table 3.7.

Table 3.7: Analytical moment and shear load resistance of coupling slab

Model	Corridor opening (L)	Analytical Moment and Equivalent storey Shear Force		
		M_r	L/2	$Q_a = M_r / (L / 2)$
	mm	kN m	m	kN
ECC350	300.00	2.154	0.15	14.36
ECC300	400.00	2.154	0.20	10.77
ECC200	600.00	2.154	0.30	7.18
SCC350	300.00	2.159	0.15	14.39
SCC300	400.00	2.159	0.20	10.79
SCC200	600.00	2.159	0.30	7.20

3.6 Casting of Model Specimens

The casting of specimens with 3 different assemblies with 2 different kinds of concrete materials was carried in the Concrete Laboratory of Ryerson University. A flexible wooden mould was designed and fabricated, that can accommodate all the variability in dimensions, as shown in Fig. 3.13.

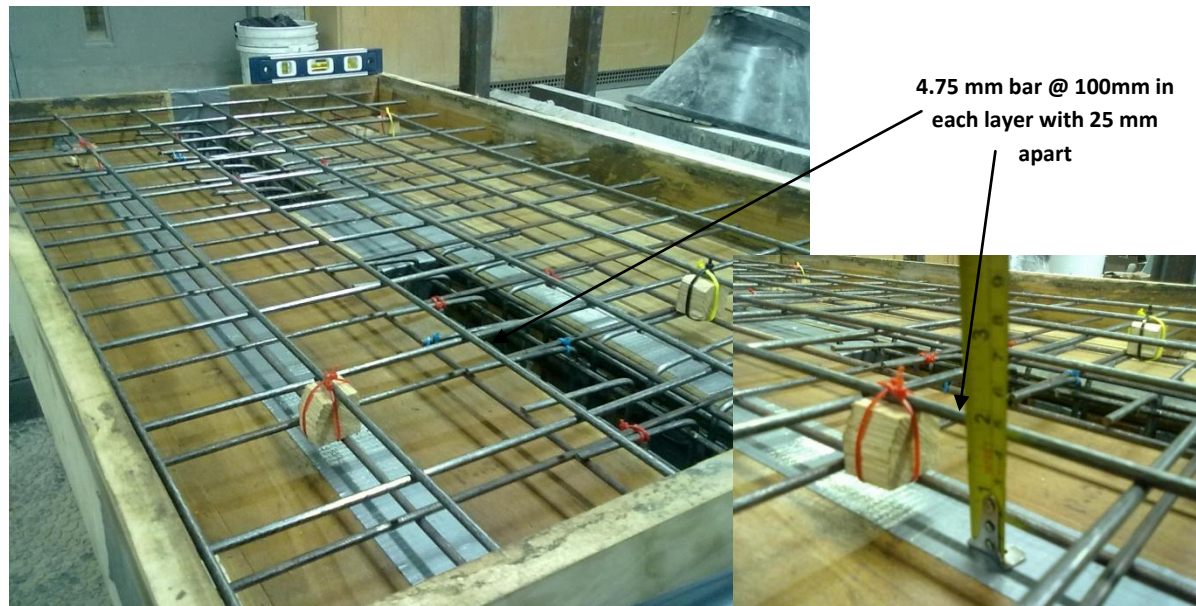


Figure 3.13: Formwork/mould ready with steel reinforcements for casting CSW model specimens



Figure 3.14: Casting of highly flowable ECC mixture into the mould

Immediately after mixing ECC/SCC were poured in into the mould without consolidation. Fig. 3.13 and Fig. 3.14 show the typical casting of ECC specimen. Fig. 3.14 shows highly flowable ECC went inside the narrow gaps of heavily reinforced walls with ease saving construction time and ensuring high quality work without voids. Same ease of casting was observed with flowable SCC. Control specimens in the form of cylinders and beams were also cast at the same time. After casting, CSW specimens and control specimens were covered with plastic sheets. After 48 hours, model specimens and control specimens were de-molded. Model and control specimens (covered with plastic bags) were then left to air cure under uncontrolled conditions of humidity and temperature until testing at the age of 28 days.

3.7 Experimental Set-up, Instrumentation and Testing

After 28 days of curing, coupled shear wall specimens were attached to the test set-up for testing under monotonic loading to failure. Figs. 3.15 to 3.18 show the laboratory test set-up with CSW specimen and instrumentation. One wall was attached to the fixed platform and other wall was free to move upward with help of hydraulic jack directly applying vertical force (Q) on the wall centre through the steel plate-angle assembly (Fig. 3.15). The walls of the model specimens were fixed to the base plate with the help of 12.5 mm threaded rod (casted in the walls previously) with the help of steel angle assembly. The movement of the movable base plates with wall (movable platform) was guided by roller on the sides to ensure pure vertical movement of the wall. The angle-plate assembly provided at both platforms holds the specimen at horizontal position with zero displacements displacement during the loading. Strain gauges were installed on the concrete surface and as well as on the top and bottom reinforcing bars at key locations.

Four different linear variable displacement transducers (LVDTs) were installed to measure the displacements (δ) at four different critical locations such as at the middle of the movable wall, upper edge of movable wall, center of the slab and center of the fixed wall (Figs. 3.15 and 3.18). Hydraulic jack, strain gauges and LVDT's were directly connected to the computerized data acquisition to record load, strain and displacement during the loading history until failure.

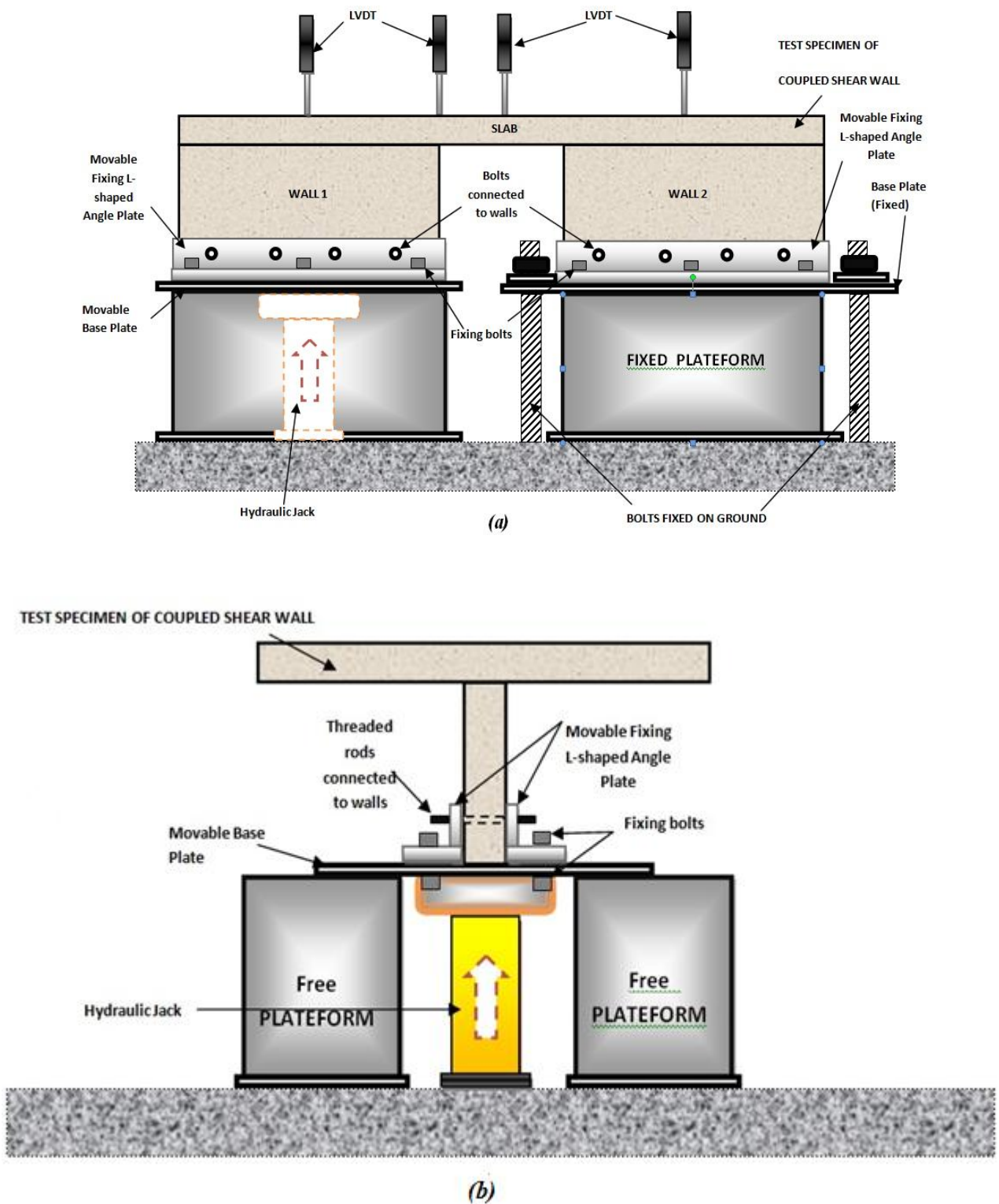


Figure 3.15: (a) Front view (b) Side-View of experimental setup

Load was applied at the rate of 0.05 kN per minute until the failure of the specimens. During the loading history, load, displacements, strains in concrete and reinforcing steel, cracking, crack propagation, and failure modes of the specimens were observed. From the test, load-displacement ($Q-\delta$) and corresponding moment-rotation ($M-\Theta$) response (as illustrated in Fig. 3.1) was obtained for each of the CSW model specimens.

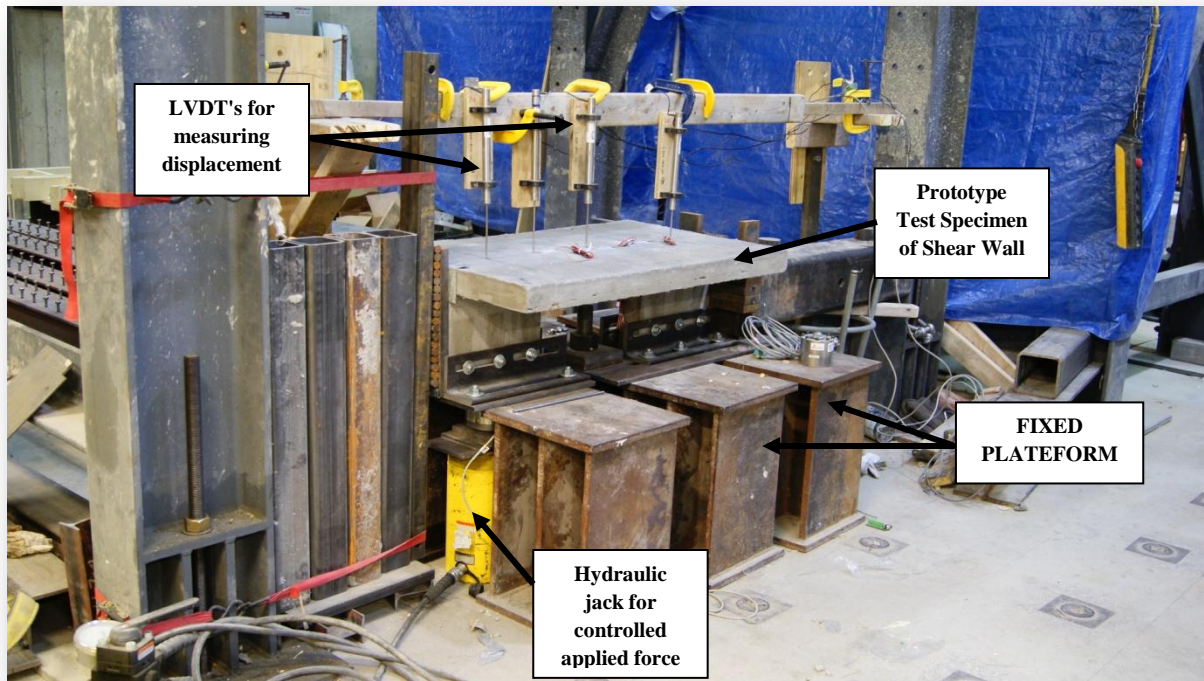


Figure 3.16: *Laboratory test setup (instrumentation)*

Figure 3.17 and 3.18 show the testing of CSW specimen having a L/X of 0.6. Fig. 3.17 showing the supports installed for test setup accordingly. Fig. 3.18 showing the deformed specimen subjected to load applied through the movable wall proved that the principle of simulating flexural behaviour of coupling slab was working.

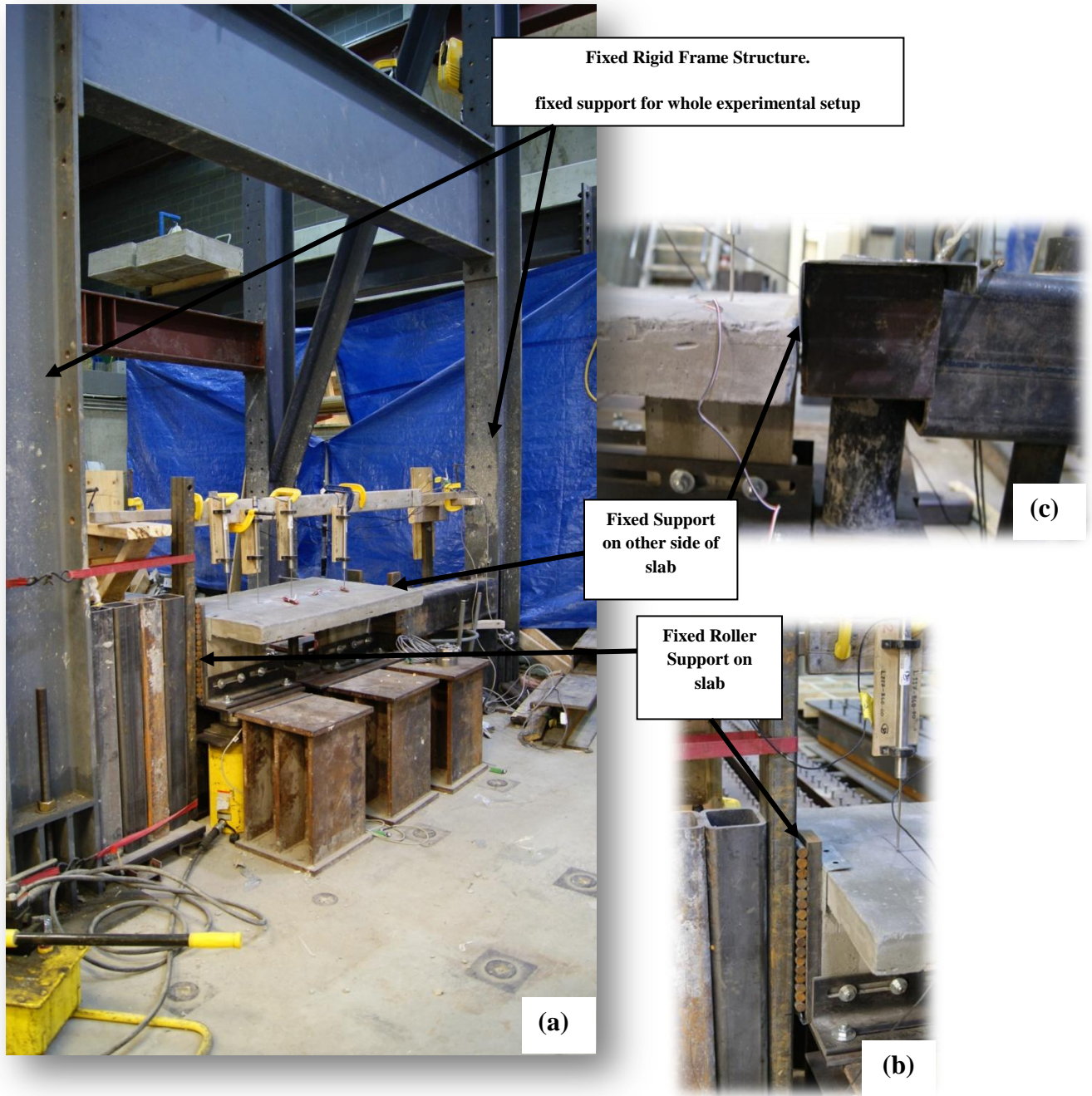


Figure 3.17: Laboratory test setup (supports)



Free moving
vertically up in
experimental
setup

Fixed wall of
experimental
setup



Figure 3.18: Laboratory test setup exhibiting desired deformed behaviour of coupled shear wall

3.8 Chapter Summary

Test set-up and its working principle are described in addition to the details of CSW model specimens (including dimensions, reinforcement design, and theoretical strength), ECC/SCC mix design/properties, instrumentation, and testing procedures. The test results and their analyses, discussion and interpretation will be provided in the next chapters.

CHAPTER 4

ANALYSES OF EXPERIMENTAL RESULTS

4.0 Introduction

This chapter presents an analysis of test results based on load-displacement response, strain development in steel and concrete, cracking and failure modes of CSW model specimens to study the influence geometric parameters and type of HPCs namely SCC and ECC. In addition, cracking, yielding and ultimate loads of CSW model specimens are identified from the load-strain and load-displacement responses. The performance of reinforced ECC and SCC based CSW specimens are compared based on strength, ductility and energy absorbing capacity.

4.1 Experimental Results

A systematic experimental investigation was conducted on the non-linear behaviour of reinforced ECC and SCC slabs in coupled shear walls. The CSW model specimens with different configurations with planar shear walls were used. The CSW models were divided into three different groups having L/X of 0.3, 0.4 and 0.6 with Y/X of 0.1 and constant reinforcement in the slab. The geometry of these models was explained in the previous chapter. The behaviour of ECC and SCC coupling slabs will be compared and explained based load-deflection ($Q-\delta$) response, stress-strain development in steel and concrete and failure modes including cracking and crack propagation.

4.1.1 Behaviour of Reinforcement in Slab based on Strain Development

The strain gauges were installed at key locations in the reinforcing bars before casting of concrete. Typical strain gauge locations are shown in Fig. 4.1. All the strain gauges were located along the centre line of the slab in line with walls. Strain gauge 1 was installed near the inner edge of the moving wall on the top reinforcement where it will be subjected to tension as per deformed shape of the coupling slab under loading (Fig. 3.1 in Chapter 3). Strain gauges No. 2 and 3 were installed at inner edges of the fixed wall on the top and bottom reinforcement where they were expected to be subjected to compression and tension, respectively.

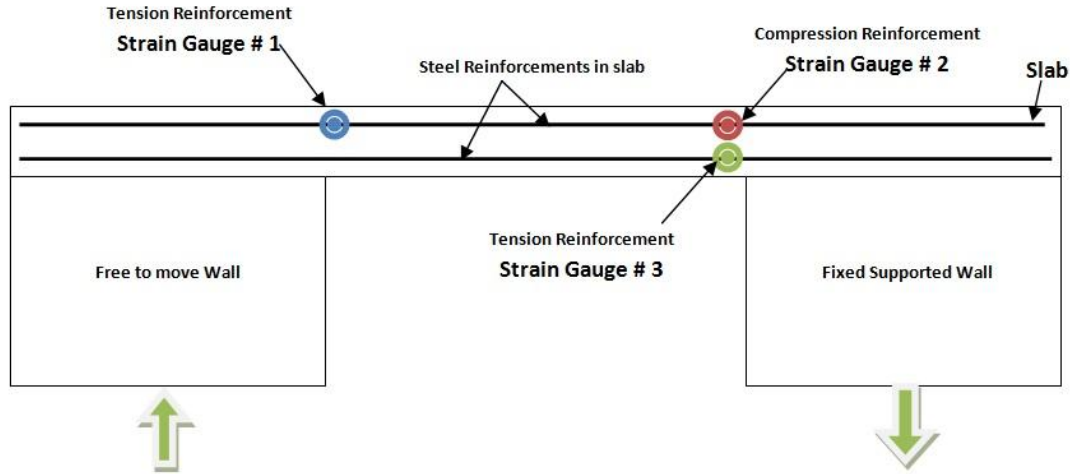


Figure 4.1: Locations of strain gauges at slab reinforcements

Figure 4.2 shows a typical load-strain response illustrating SCC300 model specimen. It is noted that steel at the tension (strain gauges 1 and 3) zone yielded before failure. The green and blue line (strain gauges 1 and 3) is clearly indicating a sudden increase in the strain development (more than 2000 micro-strain) at ultimate load of 10.94 kN when the slab was failed. The strain development in strain gauge 2 (red line) confirms that the steel in the compression zone was not yielded even the slab reached its ultimate load carrying capacity. Hence, theoretical calculation based of ultimate load of coupling slab based yielding of reinforcement and proved to be true from the experimental strain development. It can also be observed that the yielding load was lower than the ultimate load and in this particular slab the yield load was 8.70 kN. It is important to notify that first yielding of steel bars were indicated by strain gauge 3 (near the edges of fixed wall) at about 10.81 kN, and after that with slight increase of loading, strain gauge no. 1 also yielded and the slab failed at 10.94 kN. More or less similar behaviour was observed in other ECC and SCC specimens. For all the specimens, failure was due to the failure coupling along transverse line passing through the edge of the shear wall where reinforcement was yielded. However, the analysis of concrete strain will provide more insight into the coupling slab behaviour.

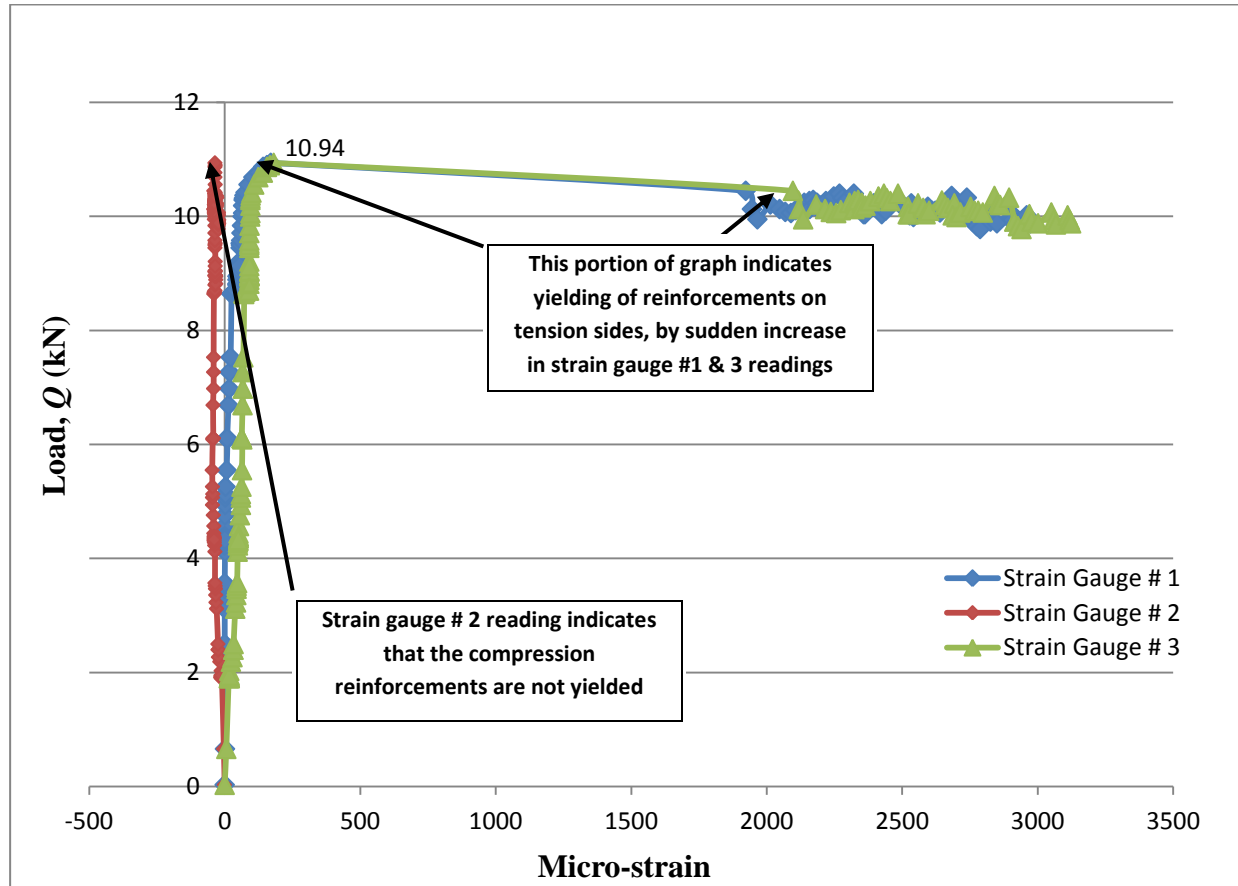


Figure 4.2: Load-strain relationship of reinforcements in the slab of SCC300

4.1.2 Strain Development in Concrete and Proof of Theory

To monitor development of strain in concrete, the strain gauges were installed at the top surface of slabs near inner edges of both wall (strain gauge 1 and 3) walls and at the centre (strain gauge 2) of the slab where the point of contraflexure was expected. All the strain gauges were installed along the centre line of the slab. Figs. 4.3 and 4.4 show the typical location of strain gauges in the model specimens.

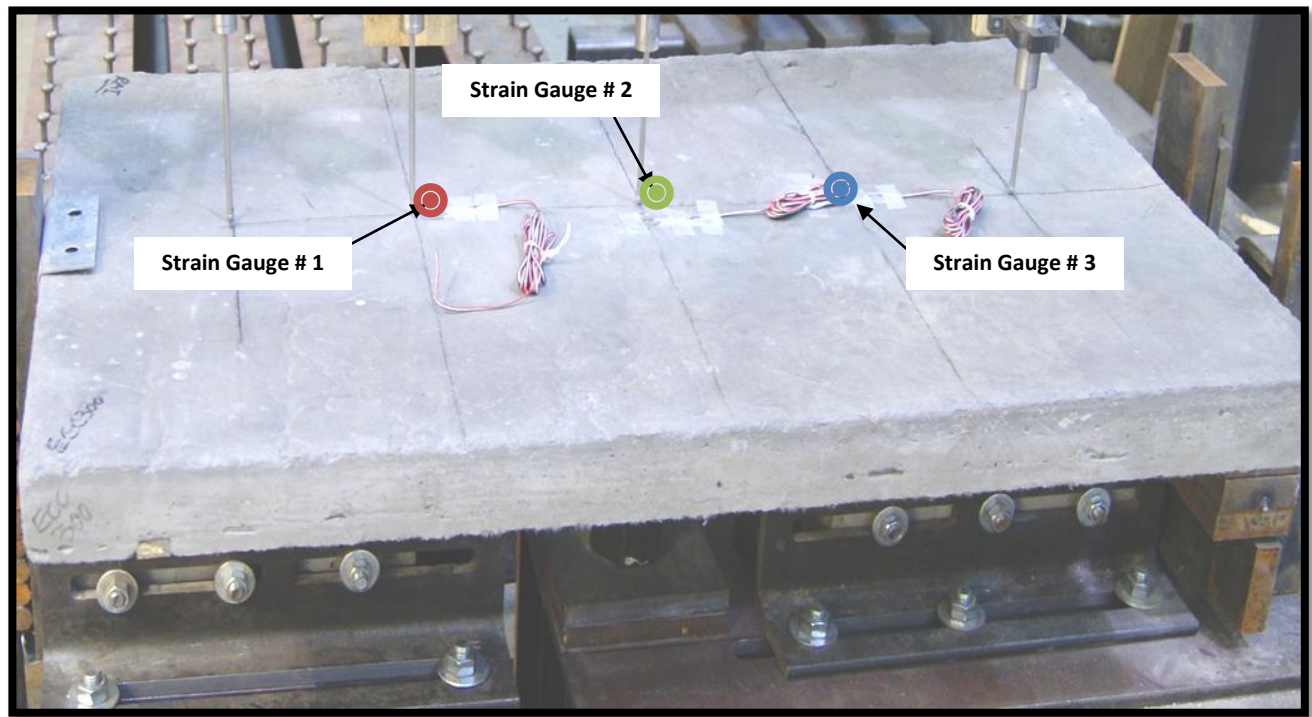


Figure 4.3: Placement of strain gauges in concrete

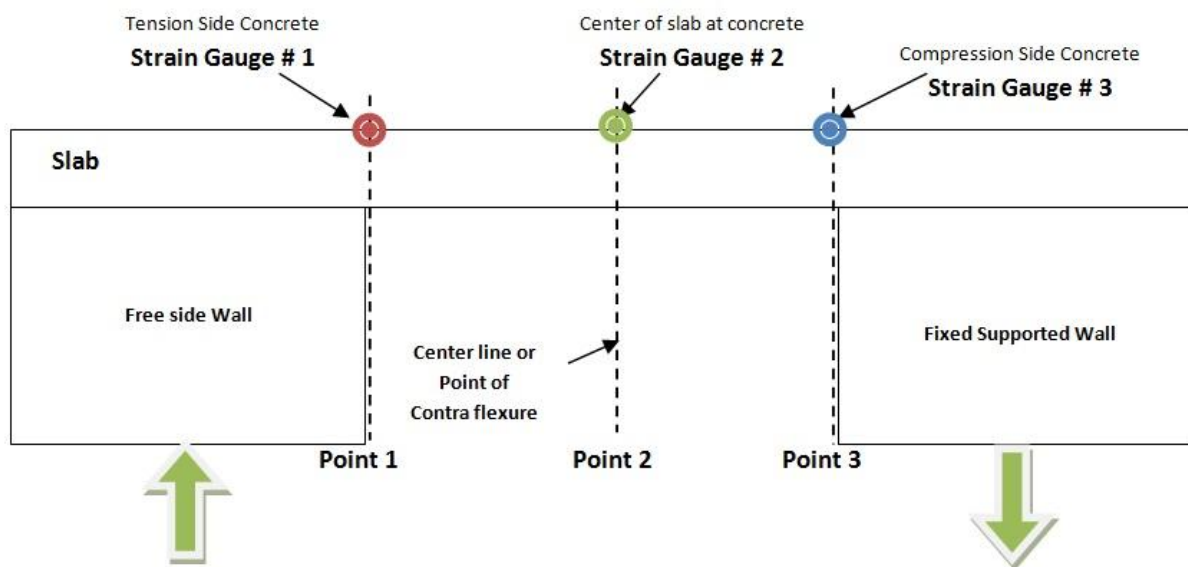


Figure 4.4: Diagram showing the locations of strain gauges

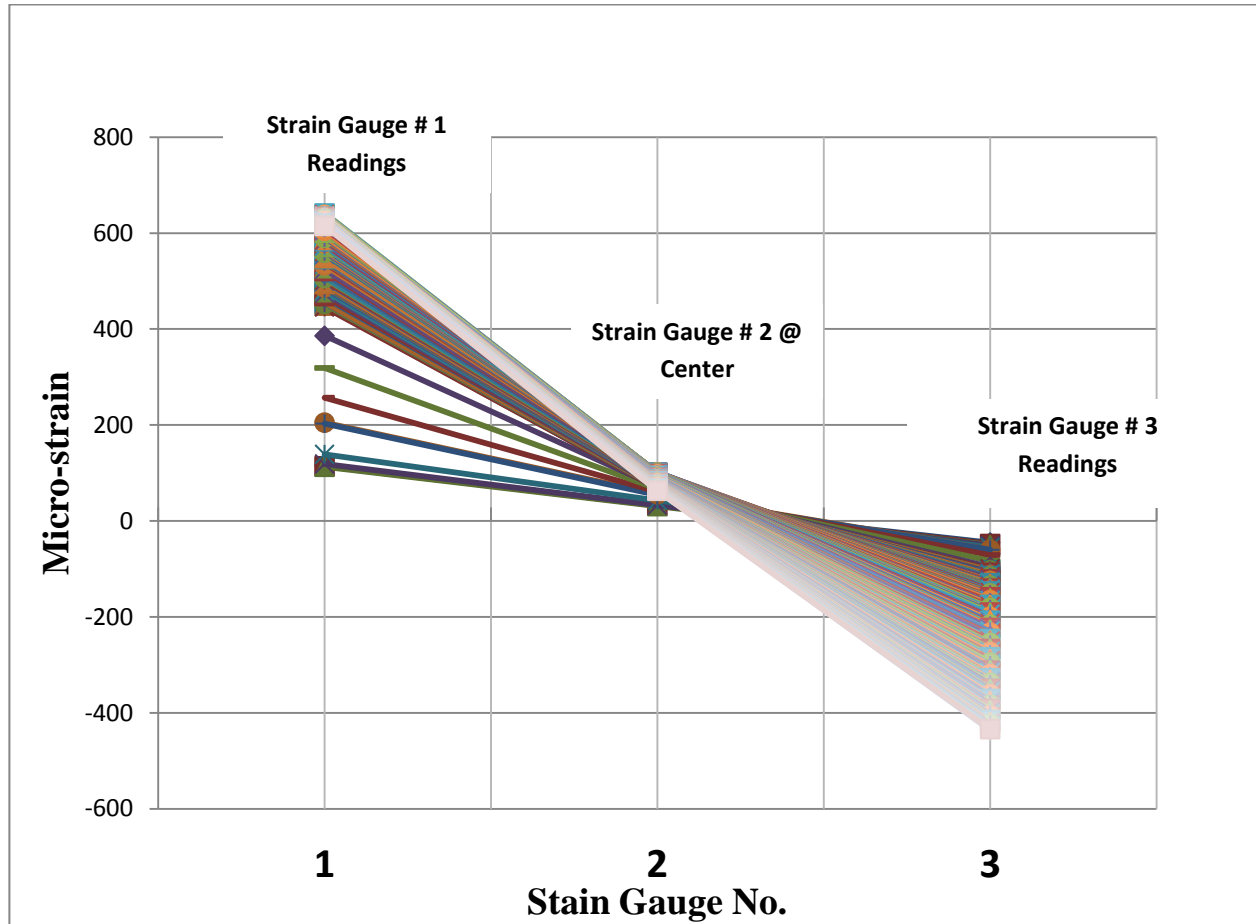


Figure 4.5: Strain relationship of all 3 strain gauges, showing point of contra-flexure form at the center of ECC300

Figure 4.5 shows typical variation of concrete strain along the length of the slab at different load levels (Q) illustrating the case of specimen ECC300. Strain gauge was subjected to tensile strain and strain gauge 3 was subjected to tensile strain as expected. It is interesting to note that very small strain at the centre (Strain gauge 2) compared to Gauge 1 and gauge 2 proved the existence of point of contra-flexure as assumed in theoretical formulation of Continuous Medium Method (Coull and Choudhury 1967a,b; Hossain 2003). This experiment proved a very important basic assumption of the existence of point of contraflexure in the middle of the coupling slabs in shear wall structures. This also proved that the test set-up realistically simulated the behaviour of coupling slabs under lateral loads.

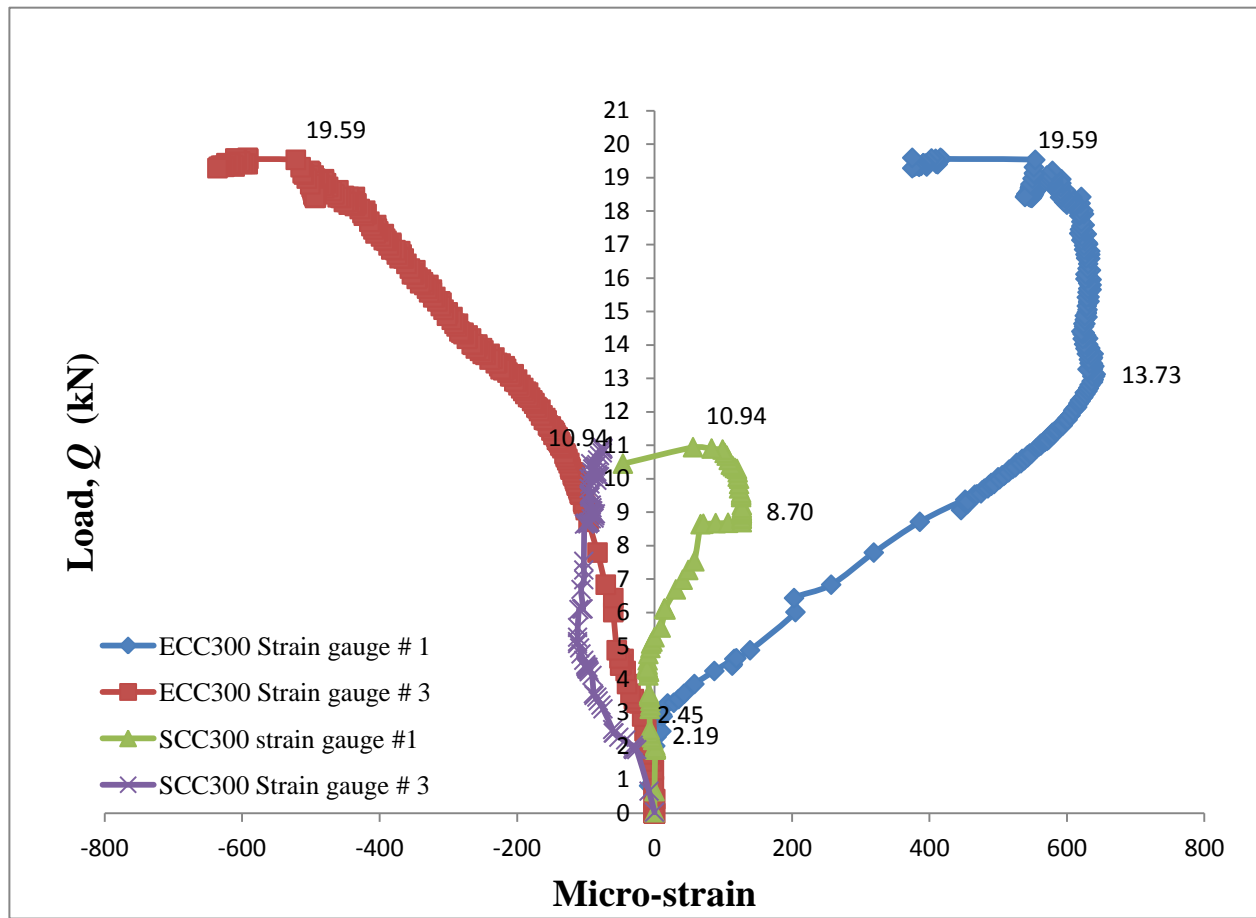


Figure 4.6: Comparison of load-concrete strain relationship of ECC and SCC ($L/X\ 0.4$)

Fig. 4.6 compares the load-concrete strain responses of SCC and ECC model specimens (ECC300 and SCC300) with $L/X = 0.4$. The tensile and compression strain development at the edge of free wall (strain gauge 1) and fixed wall (strain gauge 3), respectively, clearly signified the true behaviour of coupling slab. It is interesting to note that ECC walls developed significantly higher tensile and compressive strain compared to its SCC counterparts. This can be associated with the higher strain hardening capacity of ECC and its capability to produce micro-cracking. This is an important finding which signifies the superior performance of ECC slabs compared to SCC slabs in terms of ductility and energy absorbing capacity of the system. Other ECC and SCC model specimens showed similar trends of variation of concrete strain development.

Analysis of strain development in all the model specimens is conducted. From the change in the load-strain development response (such as change in slope), it was possible to identify approximately the cracking, yielding and ultimate loads of the CSW model specimens. The cracking, yielding and ultimate loads are compared from simultaneous analysis of load-strain and load-displacement relationship of CSW specimens. Table 4.1 summarizes cracking, yielding and ultimate loads and corresponding concrete strains of the CSW specimens.

Table 4.1: Load and concrete tensile strain in cracking, yielding and ultimate stages

Model	Cracking stage		Yielding stage		Ultimate stage	
	Load (kN)	micro-strain	Load (kN)	micro-strain	Load (kN)	micro-strain
ECC350	3.09	-17	21.89	79	27.1	78
SCC350	2.4	5	8.76	130	11.6	122
ECC300	2.45	8	13.73	629	19.59	416
SCC300	2.19	-2	8.7	127	10.94	56
ECC200	1.37	22	10.7	222	17.63	153
SCC200	1.35	1	8.67	52	10.6	39

4.1.3 Load-Displacement Response, Crack Development and Failure Modes

Experimental load-displacement ($Q-\delta$) responses of CSW model specimens are analyzed to compare the performance ECC and SCC based on strength and ductility point of view as well as to study the effect of geometric parameter such as L/X .

4.1.3.1 Models with L/X of 0.3 (ECC350 and SCC350)

Fig. 4.7 compares the load-displacement responses of SCC350 and ECC350 specimens. Load increased with the increase of load for both ECC and SCC specimens. The cracking, yielding and ultimate stages can be identified from the slope changes of the load displacement response. Initially cracks started to form near the inner edges of the walls and specimen failed due to the failure of slabs due to the formation transverse cracks along the edges of the wall (Figs. 4.8 and 4.9) and

yielding of reinforcement in the tension zone as identified from steel strain development. The cracking and crack propagation is similar in both ECC and SCC specimens on the tension side.

However, ECC specimens developed very fine and large number micro-cracks not visible through naked eyes (Fig. 4.8) in contrast to the development of one or two major cracks with large crack width (maximum crack width of about 1.25 mm at failure) in SCC specimens (Fig. 4.9).

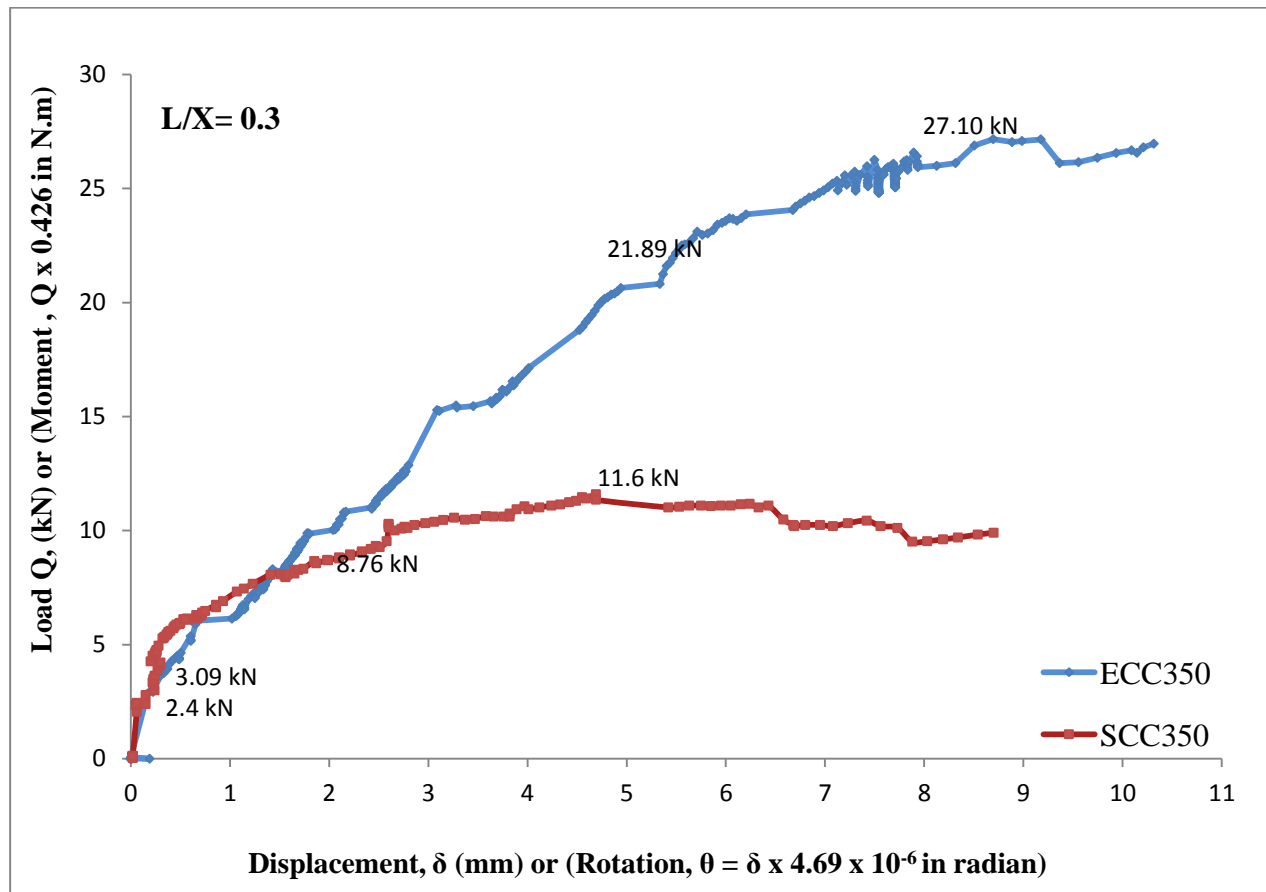


Figure 4.7: Experimental load-displacement responses of ECC and SCC specimens (L/X 0.3)

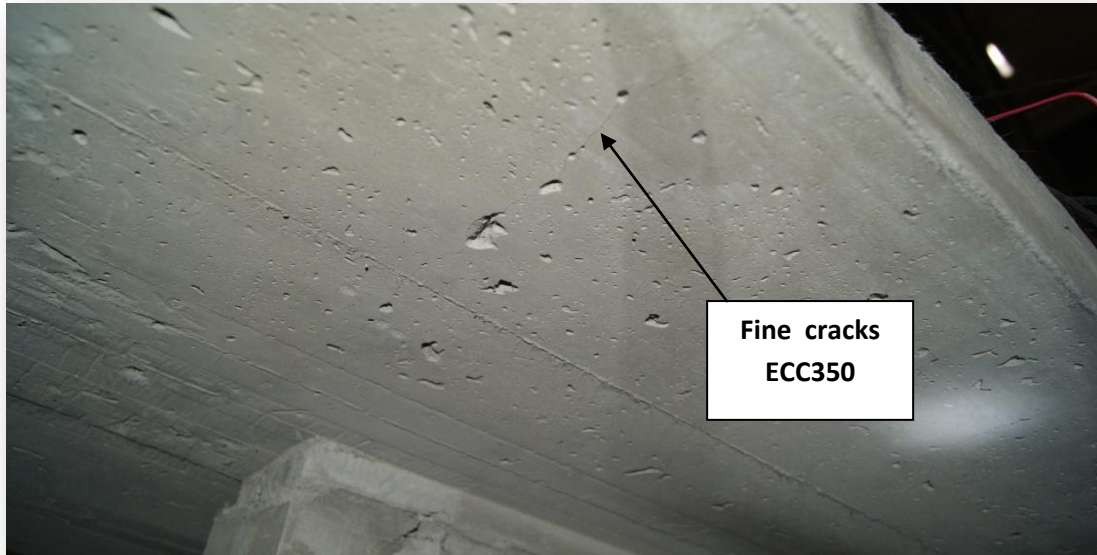


Figure 4.8: Crack development and crack propagations in ECC350 specimen at inner edges of the fixed wall

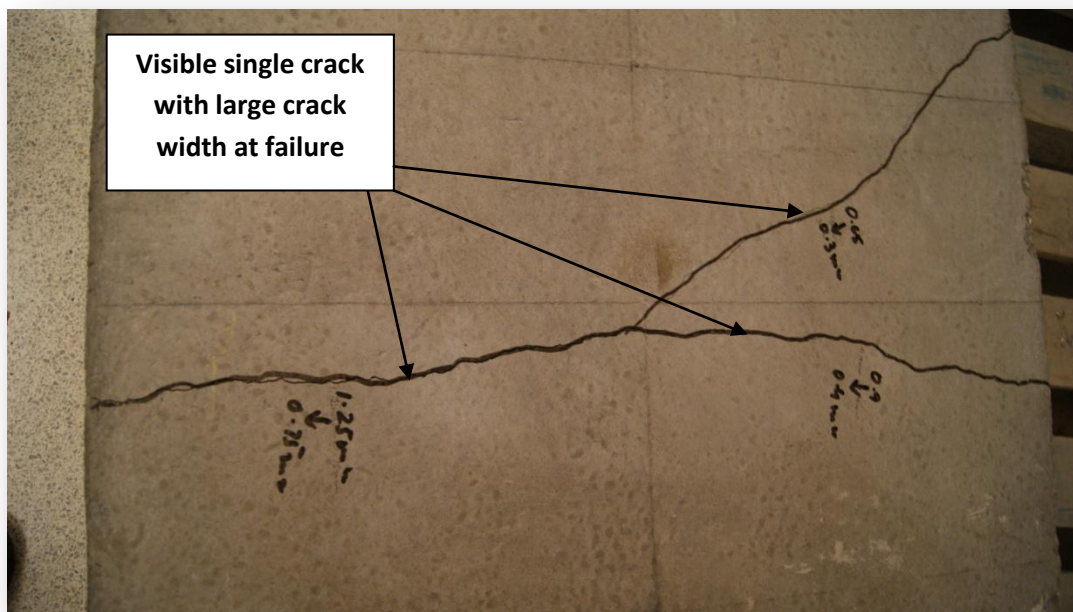


Figure 4.9: Crack development and crack propagations in SCC 350 specimen at the inner edges of the wall

In ECC350, cracking started 3.09 kN around 11.40% of ultimate load and in SCC350 at 2.4 kN around 20.69% of ultimate load (Table 4.2). Yielding of steel in ECC350 started at 80.77% of ultimate load and in SCC350 at 75.52% of ultimate load. Ultimately the ECC350 failed at much higher load of 27.1 kN compared with 11.6 kN of SCC350. ECC specimens underwent more deflection than SCC counterpart. ECC specimen showed 22.33% and 33.33% higher load and displacement respectively at cracking point, 59.98% and 67.10% higher load and displacement respectively at yielding and 57.20% and 47.15% higher load and displacement at failure compared with its SCC counterpart.

ECC specimen showed 1.89 times more ductility and 2.33 times higher ultimate load compared to its SCC counterpart (Table 4.2).

4.1.3.2 Models with L/X of 0.4 (SCC300 and ECC300)

Figure 4.10 compares the load-displacement responses of SCC300 and ECC300 specimens. Load increased with the increase of load for both ECC and SCC specimens. These specimens exhibited similar behaviour compared to ECC/SCC350 specimens in terms of cracking, yielding and failure modes.

In ECC300, cracking started 2.45 kN around 12.51% of ultimate load and in SCC300 at 2.19 kN around 20.02% of ultimate load (Table 4.2). Yielding of steel in ECC300 started at 70.09% of ultimate load and in SCC300 at 79.52% of ultimate load. Ultimately, ECC300 failed at much higher load of 19.51 kN and SCC300 at 10.94 kN. ECC specimen showed 10.61% and 20.75% higher load and displacement, respectively at cracking, 36.64% and 23.76% higher load and displacement respectively at yielding and 44.16% and 24.53% higher load and displacement respectively at failure compared with its SCC counterpart.

ECC specimen showed 1.32 times more ductility and 1.79 times higher ultimate load compared to its SCC counterpart (Table 4.2). The bigger load-displacement envelopes also shows higher energy absorbing capacity of ECC CSW specimens compared to its SCC counterpart.

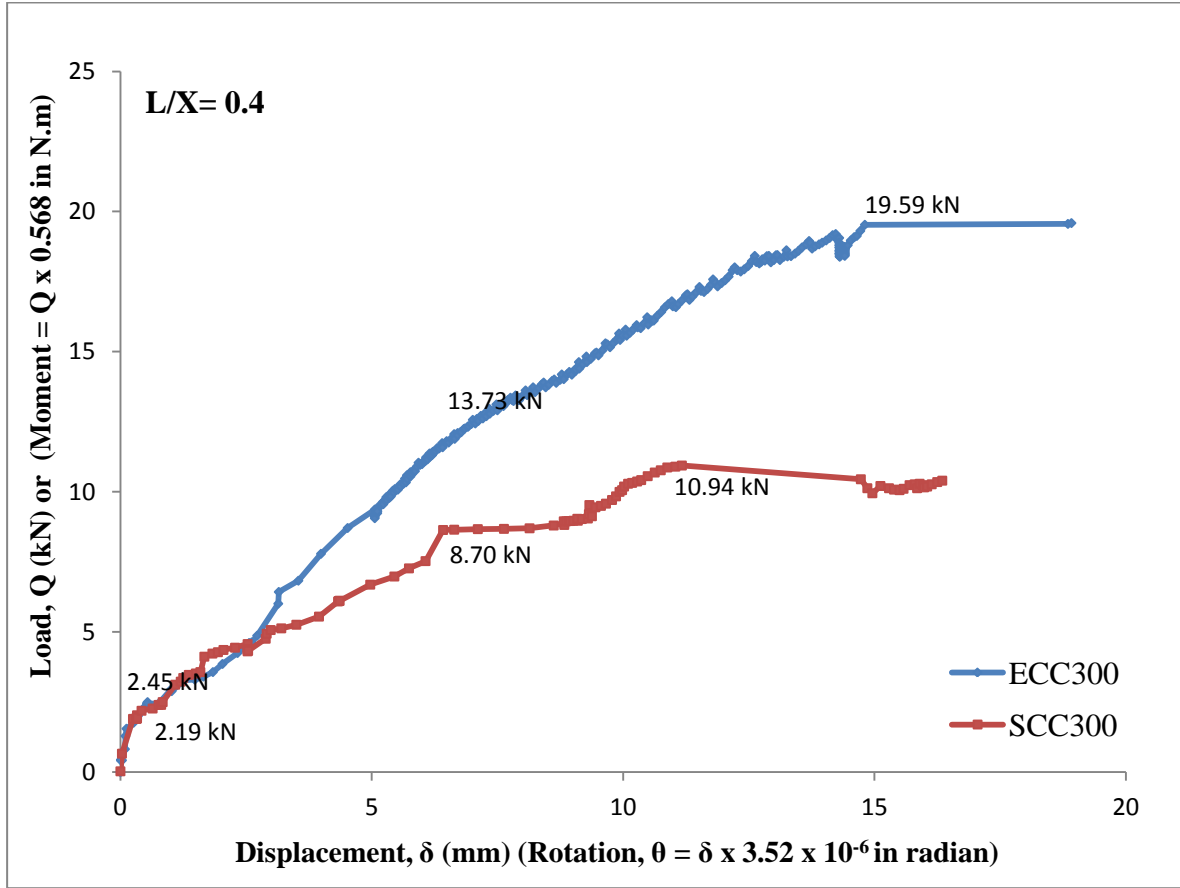


Figure 4.10: Experimental load-displacement responses of ECC and SCC specimens (L/X 0.4)

4.1.3.3 Models with L/X of 0.6 (ECC200 and SCC200)

Figure 4.11 compares the load-displacement responses of SCC200 and ECC 200 specimens. Load increased with the increase of load for both ECC and SCC specimens. These specimens exhibited similar behaviour compared to ECC-SCC350/ECC-SCC300 specimens in terms of cracking, yielding and failure modes. ECC200 specimens developed large number of transverse fine micro-cracks in coupling slabs along the inner edges of the shear wall before failure (Fig. 4.12).

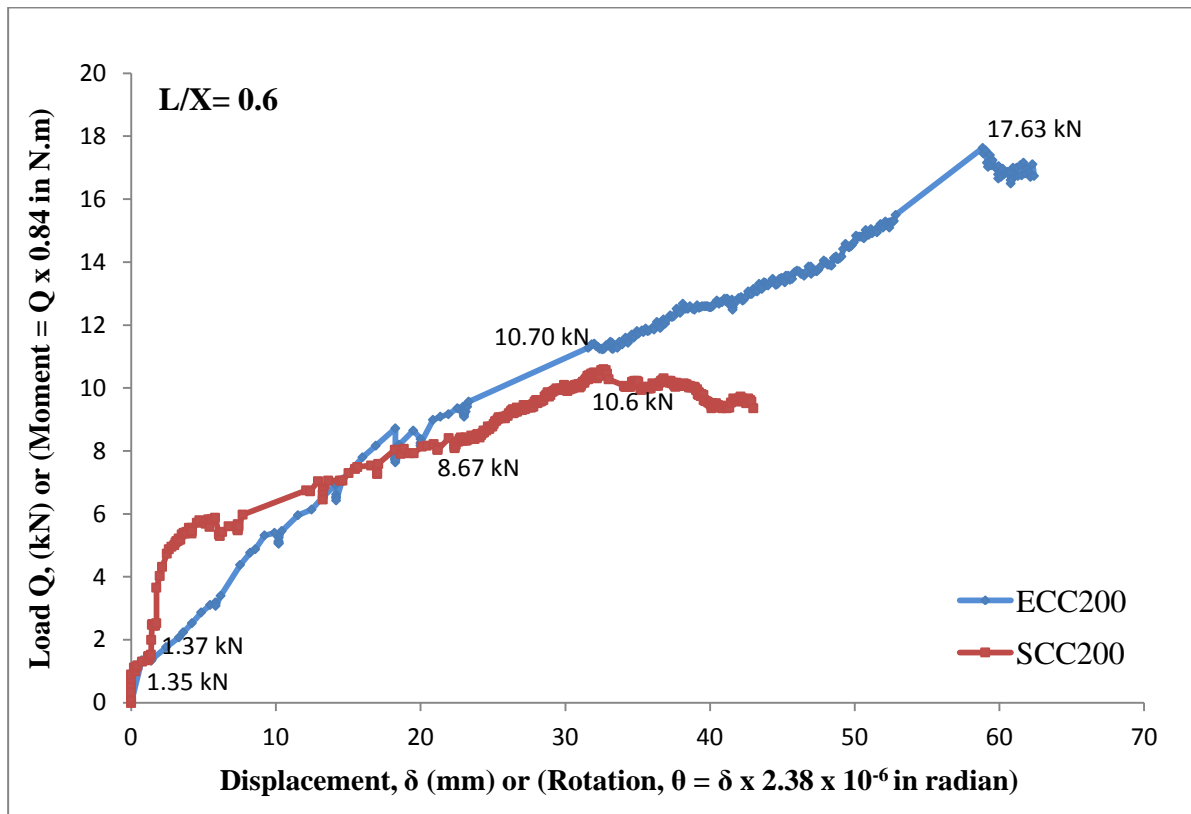


Figure 4.11: Experimental load-displacement responses of ECC and SCC specimens (L/X 0.6)

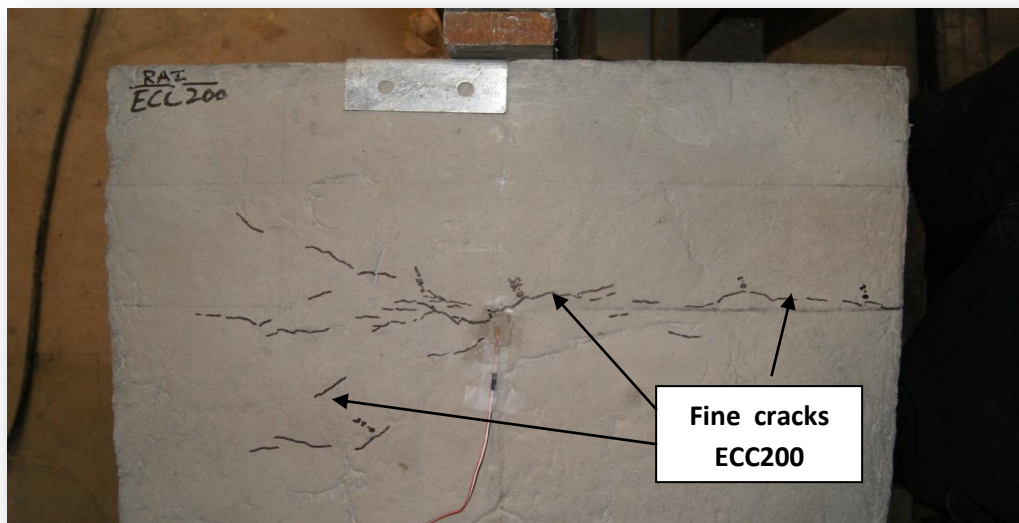


Figure 4.12: Shows small crack propagations of ECC200 slab at near inner edges at upper side of the slab on loading side

In ECC200, cracking started 1.37 kN around 7.77% of ultimate load and in SCC200 at 1.35 kN around 12.74% of ultimate load (Table 4.2). Yielding of steel in ECC200 started at 60.69% of ultimate load and in SCC200 at 81.79% of ultimate load. ECC200 failed at a higher load of 17.63 kN and SCC200 at 10.6 kN. ECC specimen showed 1.46% and 19.86% higher load and displacement respectively at cracking, 18.97% and 17.10% higher load and displacement respectively at yielding and 39.88% and 40.25% higher load and displacement respectively at failure compared with its SCC counterpart.

ECC200 specimen showed 1.67 times more ductility and 1.66 times higher ultimate load compared to its SCC200 counterpart (Table 4.2). The bigger load-displacement envelopes also shows higher energy absorbing capacity of ECC CSW specimens compared to its SCC counterpart.

Table 4.2 summarizes cracking, yielding and ultimate loads and corresponding displacement of all CSW specimens based on the analysis of load-deflection response as well as load-strain developments as described earlier. In this study, relative ductility (ψ) is defined as the ratio of ECC specimen displacement at peak load (δ_{uECC}) to corresponding SCC specimen peak displacement (δ_{uSCC}):

$$\psi = \frac{\delta_{uECC}}{\delta_{uSCC}} \quad (4.1)$$

Overall, the load carrying capacity of CSW specimens decreased and displacement increased with the increase of L/X from 0.3 to 0.6 in cracking, yielding and failure stages (Table 4.2). Failure load decreased from 27.1 kN to 17.63 kN (a reduction of 35%) for ECC and from 11.6 kN to 10.6 kN for SCC (a reduction of 9%) when L/X increased from 0.3 to 0.6. On the other hand, peak deflection increased from 8.61 mm to 58.58 mm (an increase of 580%) for ECC and 4.55 mm to 35.00 mm (669%) for SCC when L/X is increased from 0.3 to 0.6.

Table 4.2: Summary of test results from load-displacement response and also ductility values of all CSW model specimens

	Load (Q) (kN)			Displacement (δ) (mm)		
	ECC/SCC 350	ECC/SCC 300	ECC/SCC 200	ECC/SCC 350	ECC/SCC 300	ECC/SCC 200
L/X →	0.3	0.4	0.6	0.3	0.4	0.6
Cracking						
ECC	3.09	2.45	1.37	0.23	0.53	1.41
SCC	2.40	2.19	1.35	0.15	0.42	1.13
Yielding						
ECC	22.56	13.12	12.73	5.35	8.46	27.89
SCC	10.47	9.25	8.04	1.76	6.45	23.12
Ultimate (Peak)						
ECC	27.10	19.59	17.63	8.61	14.80	58.58
SCC	11.60	10.94	10.6	4.55	11.17	35.00
Ratio						
⁺ Q_{uECC}/Q_{uSCC}	2.33	1.79	1.66			
[*] $\delta_{uECC}/\delta_{uSCC} = \psi$				1.89	1.32	1.67

⁺ Q_{uECC}/Q_{uSCC} = Ratio of ultimate load ^{*} ψ : Relative ductility

In general, cracking, yielding and ultimate load were higher for ECC specimens compared with SCC specimens. The bigger load-displacement envelopes (Figs. 4.7, 4.10 and 4.11) also demonstrates high energy absorbing capacity of ECC CSW specimens compared to their SCC counterparts.

4.2 Comparison of Experimental and Theoretical Load Capacity

Table 4.3 compares theoretical load capacity of SCC/ECC coupling slab based on CSA A23.3-04 (2009) previously presented in Chapter 3 with those obtained from model tests.

Table 4.3: Comparison of experimental and theoretical load capacity of coupling slab

Model	Ultimate Equivalent storey shear load capacity of coupling slab (kN)		
	Analytical (Code) (CSA A23.3-04,2009)	Experimental	Ratio
	Q_a	Q_{exp}	Q_{exp}/Q_a
Engineered cementitious composite (ECC)			
ECC350	14.36	27.10	1.89
ECC300	10.77	19.59	1.82
ECC200	7.18	17.63	2.46
		Mean	2.06
Self-consolidating concrete (SCC)			
SCC350	14.39	11.60	0.81
SCC300	10.79	10.94	1.01
SCC200	7.20	10.60	1.47
		Mean	1.10

CSA A23.3-04 (2009) seems to have predicted load capacity of coupling slabs reasonably well as the ratio of experimental to theoretical/Code predicated values ranges between 0.81 and 1.47 with a mean value of 1.10. On the other hand, CSA A23.3-04 (2009) seems to have under predicted load capacity of coupling slabs as the ratio of experimental to theoretical/Code predicated values ranges between 1.89 and 2.46 with a mean value of 2.06. Higher load capacity of ECC coupling slab (as expected) is attributed to the presence of PVA fibers acting as reinforcement whose contributions to load carrying capacity are not considered in the CSA A23.3-04 (2009) Code. Presence PVA fibers significantly improved the crack resistance of ECC by bridging cracks and inducing lower stress transfer to embedded reinforcement (which delayed the yielding of steel) and significantly improve post-cracking and post-yielding load resistance of ECC. This is evident from the long cracking to post-yielding branch of the load-displacement responses of ECC showing significant strain hardening compared with SCC.

4.3 Chapter Conclusions

Load-displacement response, failure modes and strain characteristics of CSW specimens are found to be influenced by the type of concrete ECC or SCC as well as geometric parameters of the specimens. The load-displacement responses presented in this chapter will be used in the next Chapter to derive flexural stiffness and effective width coupling slabs in pre-cracking, cracking and post-yielding stages of the structure.

CHAPTER 5

BENDING STIFFNESS AND EFFECTIVE WIDTH OF COUPLING SLAB

5.0 Introduction

This chapter presents bending stiffness (k) and effective width (Y_e) of coupling slab in pre-cracking, cracking and post-yielding stages evaluated from the experimental load-displacement ($Q-\delta$) response or corresponding moment-rotation ($M-\Theta$) response. Influence of geometric parameters and concrete types (ECC and SCC) on bending stiffness and effective width are described. In addition, bending stiffness and effective width from previous research studies are compared. Design charts for prediction of bending stiffness and effective width are presented for practical applications.

5.1 Determination of Bending Stiffness and Effective Width of Coupling Slab

The load-displacement or moment-rotation response curve plays a very important role in determining the bending/flexural stiffness and effective width of the coupling slab in CSW system. Bending/flexural stiffness and effective width of coupling slab can be obtained by using Eq. 2.1 and Eq. 2.8 (described in Chapter 2) and $Q-\delta$ or $M-\Theta$ response from model tests.

For the determination bending stiffness throughout the loading history, each and ($Q-\delta$ or $M-\Theta$) is idealized as shown in Fig. 5.1. The slope of the initial linear part of the ($Q-\delta$ or $M-\Theta$) curve 'AB' is called as pre-cracking stiffness (k_o). The point 'B' on the curve is roughly an indication for the first appearance of the cracks. After cracking of concrete, the first part of the non-linear curve was approximated by a straight line 'BC' and the slope of this part is called cracking stiffness (k_{cr}). The point 'C' on the curve was roughly an indication of the first yielding in flexural reinforcement. After yielding the second part of the non-linear curve was approximated by a straight line 'CD' and the slope of this part is called post-yielding stiffness (k_p). The portion beyond 'D' indicated post-peak model response with point 'D' representing peak or ultimate load/moment carrying capacity of the structure.

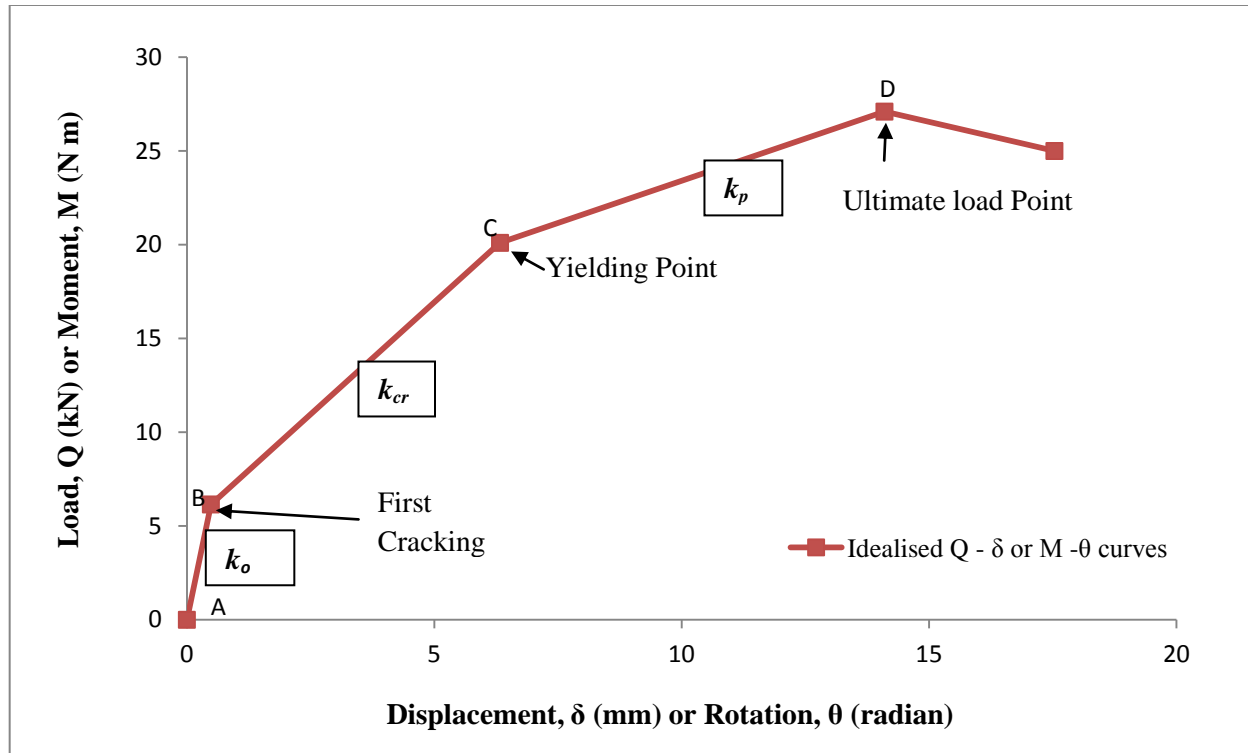


Figure 5.1: Idealized load-displacement and moment rotation cure

5.1.1 Calculation of Bending Stiffness and Effective Width

Bending stiffness (k) is evaluated based on Eq. 2.1 presented as Eq. 5.1a in this chapter.

$$\text{Bending Stiffness} = k = \frac{M}{\theta_D} \quad (5.1a)$$

Where, D = flexural rigidity of the slab = $\frac{Et^3}{12(1-\nu^2)}$,

t = thickness of slab = 60 mm and ν = Poisson's ratio for slab material = 0.15

From Equation 5.1, D is calculated for ECC and SCC specimens using average modulus of elasticity (presented in Chapter 3) of the concrete $E_{ECC} = 24,740$ MPa and $E_{SCC} = 32,130$ MPa respectively.

$$\text{Flexural Rigidity for ECC slab} = \frac{24740 \times 60^3}{12(1-0.15^2)} 10^{-3} = 45557.033 \text{ N.m}$$

$$\text{Flexural Rigidity for SCC slab} = \frac{32130 \times 60^3}{12 (1 - 0.15^2)} 10^{-3} = 59165.214 \text{ N.m}$$

Bending stiffnesses are calculated from the idealized line at different stages by Eq. 5.1b:

$$k_o = \frac{M_{cr}}{\theta_{cr} D} \quad ; \quad k_{cr} = \frac{M_y - M_{cr}}{\theta_{ys} D}; \quad k_p = \frac{M_u}{(\theta_u - \theta_{ys}) D} \quad (5.1b)$$

where M_{cr} , M_y and M_u are the moment at cracking, yielding and ultimate stage respectively and θ_{cr} , θ_{ys} , and θ_u , at cracking, yielding and ultimate stage, respectively.

Multiplication factors are also calculated to transform Q and δ to corresponding M and Θ , respectively based on geometric dimensions of the CSW models. Table 5.1 presents the multiplication factors.

Table 5.1: Multiplication factors

L/X	Multiplication factors	
	Moment (M) $l = L + W$	Rotation (θ) $= (2/l) \times 10^{-3}$
	m	Radians
0.3	0.426	4.69484E-06
0.4	0.568	3.52113E-06
0.6	0.840	2.38095E-06

By multiplying load and deflection values by factors tabulated in Table 5.1 moment and rotation values are obtained.

Using idealized ($M-\Theta$ or $Q-\delta$) curves for each of the model specimens, the values of bending stiffness at pre-cracking, cracking and post yielding stages (k_o , k_{cr} and k_p , respectively) are calculated using Eq. 5.1. Typical idealized ($M-\Theta$) curves for model specimens are presented in Figs. 5.2 to 5.4. Strain hardening of ECC can be clearly visibly from the longer cracking and yielding branch of the idealized curves.

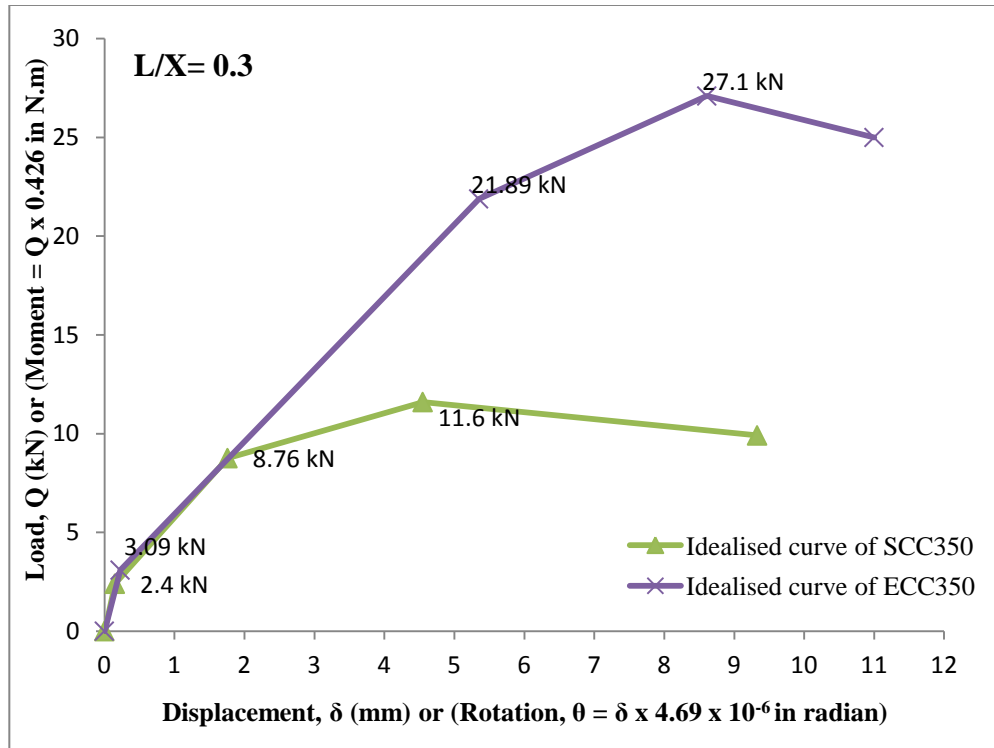


Figure 5.2: Idealized load-displacement and moment-rotation curves of ECC and SCC models

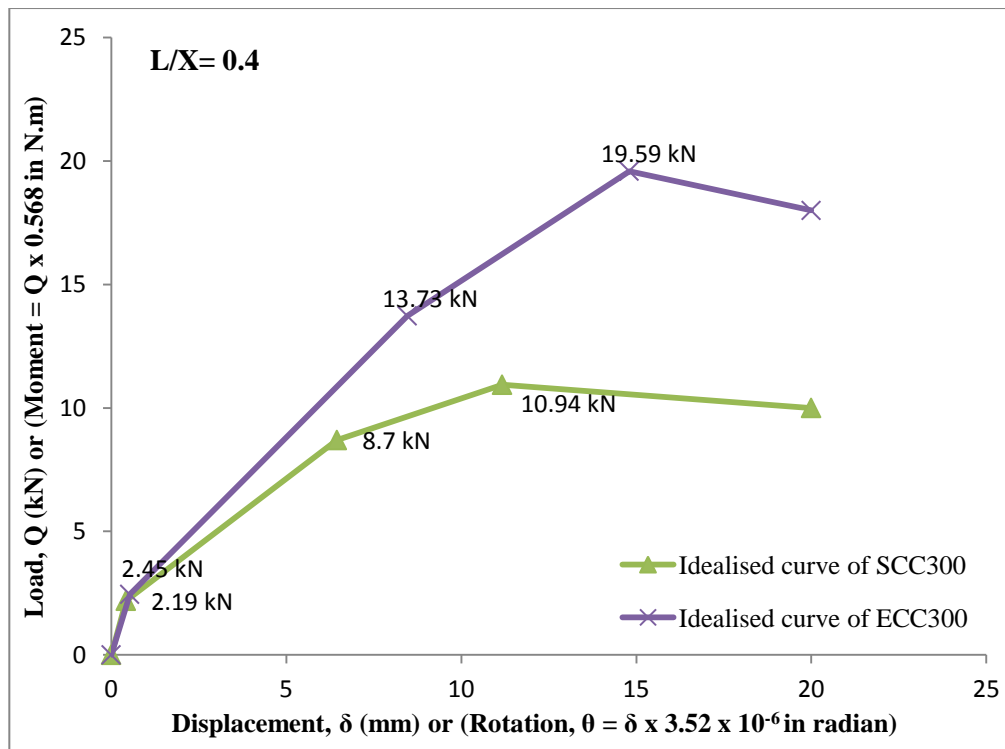


Figure 5.3: Idealized load-displacement and moment-rotation curves of ECC and SCC models

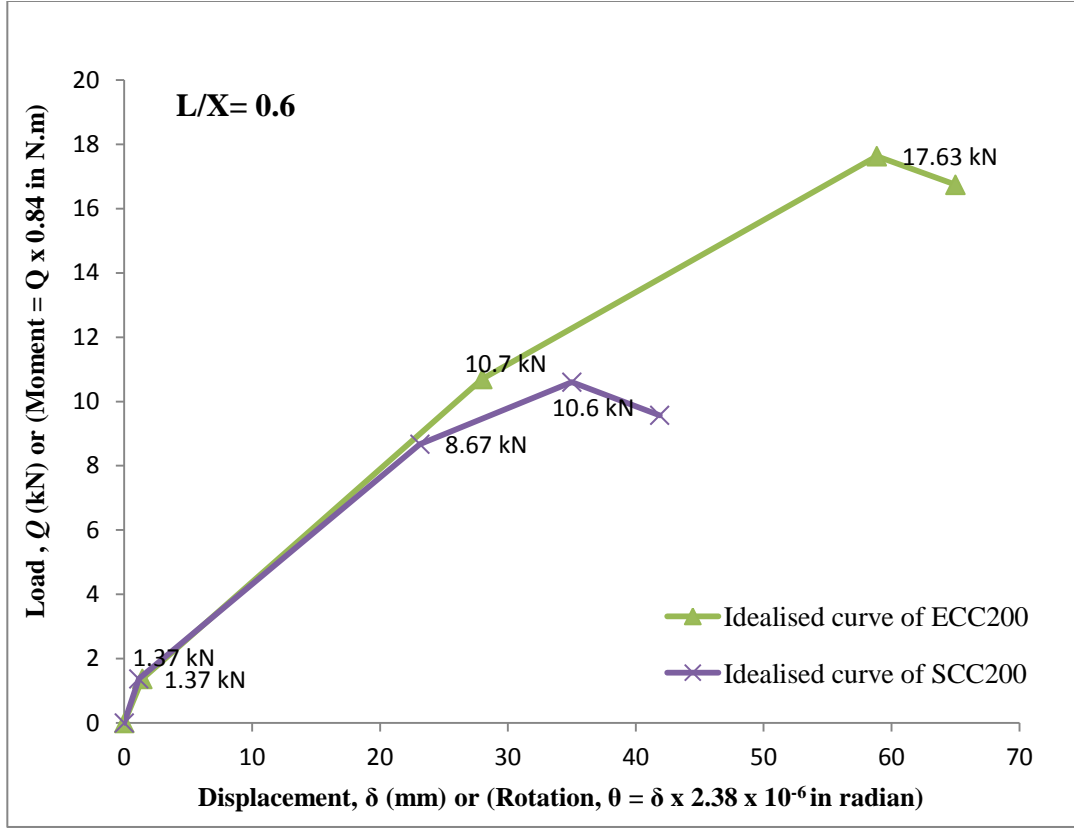


Figure 5.4: Idealized load-displacement and moment-rotation curves of ECC and SCC models

Bending stiffness values and associated data are presented in Table 5.2 for all CSW model specimens are presented in Table 5.2. Bending stiffness values clearly indicates that $k_o > k_{cr} > k_p$ which means bending stress decreases as model specimens pass through pre-cracking, cracking and post-yielding stages irrespective of type of concrete (ECC or SCC) and geometric parameters). For example, for ECC350: k_o (27.353) $>$ k_{cr} (7.306) $>$ k_p (4.744) while SCC350, also k_o (24.538) $>$ k_{cr} (6.058) $>$ k_p (2.733).

Table 5.2: Bending stiffness in pre-cracking, cracking and post-yielding stages

Model No	Y/X	L/X	Pre- cracking Stage			
			Load	Deflection	Moment	Bending stiffness (k_o)
			Q	δ	M_{cr}	
			kN	mm	kN m	
ECC350	0.6	0.3	3.09	0.23	1.32	27.353
SCC350			2.40	0.15	1.02	24.538
ECC300		0.4	2.45	0.53	1.39	16.368
SCC300			2.19	0.42	1.24	14.217
ECC200		0.6	1.37	1.41	1.15	7.524
SCC200			1.35	1.13	1.13	7.124
Model No		L/X	Cracking Stage			
			Load	Deflection	Moment	Bending stiffness (k_{cr})
			Q	δ	M_y	
			kN	mm	kN m	
ECC350	0.6	0.3	21.89	5.35	9.33	7.306
SCC350			8.76	1.76	3.73	6.058
ECC300		0.4	13.73	8.46	7.80	5.037
SCC300			8.70	6.45	4.94	2.943
ECC200		0.6	10.70	27.89	8.99	2.729
SCC200			8.67	23.12	7.28	1.985
Model No		L/X	Post-yielding Stage			
			Load	Deflection	Moment	Bending stiffness (k_p)
			Q	δ	M_u	
			kN	mm	kN m	
ECC350	0.6	0.3	27.10	8.61	11.54	4.744
SCC350			11.60	4.55	4.94	2.733
ECC300		0.4	19.59	14.80	11.13	4.283
SCC300			10.94	11.17	6.21	2.350
ECC200		0.6	17.63	58.58	14.81	2.002
SCC200			10.60	35.00	8.90	1.503

The degradation of stiffness indicates that model specimens suffered damage to reach a particular stage of the load-displacement response. Let us say, if the structure is loaded to cracking

at the first time, the structure is damaged and the residual stiffness is $(1-k_o)$. Next time, when cracked structure is reloaded, the stiffness of the structure will be $(1-k_o)$.

Once the bending stiffness in various stages (k_o , k_{cr} , k_p) are calculated, they can be substituted in Eq. 2.8 (Chapter 2) presented as Eq. 5.2 in this chapter to calculate pre-cracking effective width (Y_{eo}), cracking effective width (Y_{ecr}) and post-yielding effective width (Y_{ep}).

$$\frac{Y_e}{Y} = \frac{k}{6(1-\nu^2)} \left(\frac{L}{Y}\right) \left(\frac{L}{L+W}\right)^2 \quad (5.2)$$

Table 5.3 summarizes geometric parameters, bending stiffness and effective width of all CSW model specimens in pre-cracking, cracking and post-yielding stages. Bending stiffness and effective width from previous research studies by Hossain (2003); Coull & Wong (1981) and Qadeer and Smith (1969) are also presented for comparison.

Table 5.3: Summary of geometric parameters, bending stiffness and effective width

Model	Parameters			Bending Stiffness (k)			Effective Width			Stiffness Ratio	
	Author										
	Y/X	L/X	L/Y	k_o	k_{cr}	k_p	Y_{eo}/Y	Y_{ecr}/Y	Y_{ep}/Y	k_{cr}/k_o	k_p/k_o
SCC350	0.60	0.30	0.50	24.54	6.06	2.73	0.45	0.11	0.05	0.25	0.11
SCC300		0.40	0.67	14.22	2.94	2.35	0.53	0.11	0.09	0.21	0.17
SCC200		0.60	1.00	7.12	1.98	1.50	0.68	0.19	0.14	0.28	0.21
ECC350	0.60	0.30	0.50	27.35	7.31	4.74	0.50	0.13	0.09	0.27	0.17
ECC300		0.40	0.67	16.37	5.04	4.28	0.61	0.19	0.16	0.31	0.26
ECC200		0.60	1.00	7.52	2.73	2.00	0.72	0.26	0.19	0.36	0.27
	Hossain (2003)										
SW63	0.60	0.30	0.50	20.61	5.90	1.83	0.38	0.11	0.03	0.29	0.09
SW64		0.40	0.67	12.56	2.93	1.14	0.47	0.11	0.04	0.23	0.09
SW66		0.60	1.00	6.05	1.51	0.75	0.58	0.15	0.07	0.25	0.12
			Qadeer & Smith (1969)	21.5		Coull & Wong (1981)	0.38				
				10.6			0.47				
				5.4			0.58				

5.2 Design Curves for Effective Width and Bending Stiffness

Figs. 5.5, 5.6, 5.7 and 5.8 present design curves for the calculation of effective widths (Y_{eo} , Y_{ecr} , Y_{ep}) of the coupling slabs in the pre-cracking, cracking and post-yielding stages. Effective widths are plotted as a function of L/X for a particular value of $Y/X = 0.6$ (Figs. 5.5 and 5.6). The polynomial trend shows that the effective width increases with the increase of L/X . The same behaviour was observed when effective widths are plotted as a function of L/Y at particular value of $Y/X = 0.6$ (Figs. 5.7 and 5.8). It is also found that the effective widths gradually decrease as the material passes through pre-cracking, cracking and post-yielding stages.

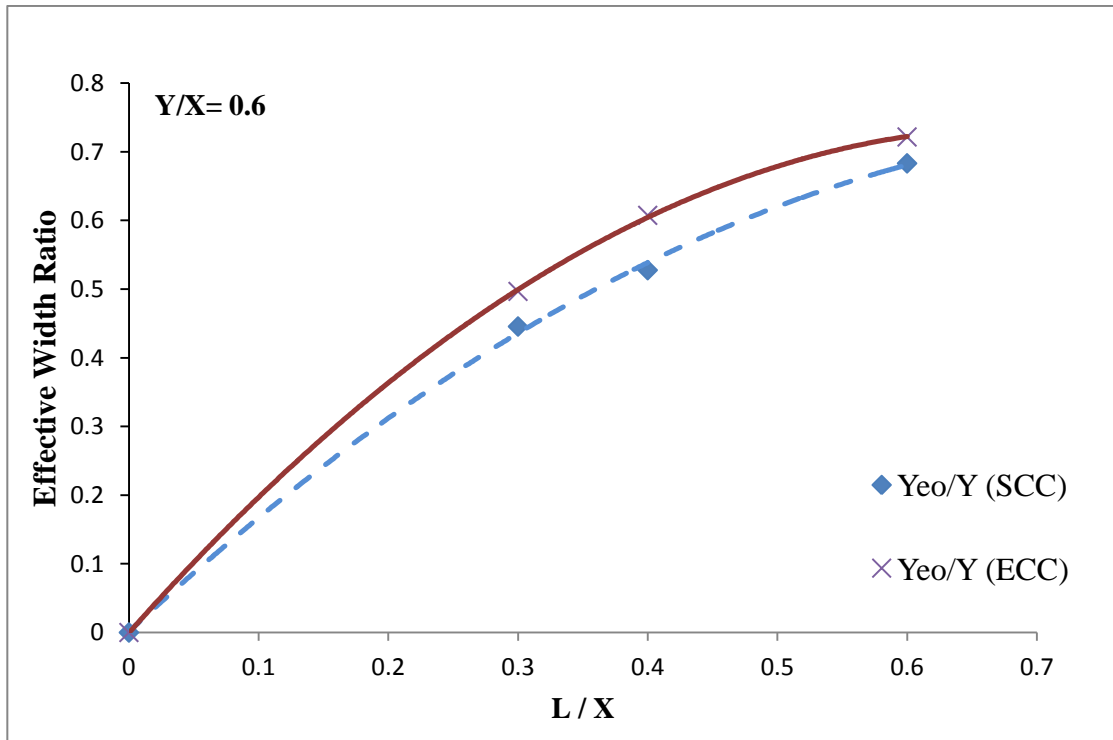


Figure 5.5: Comparison of effective width of ECC/ SCC slab at pre-cracking stage as function of L/X

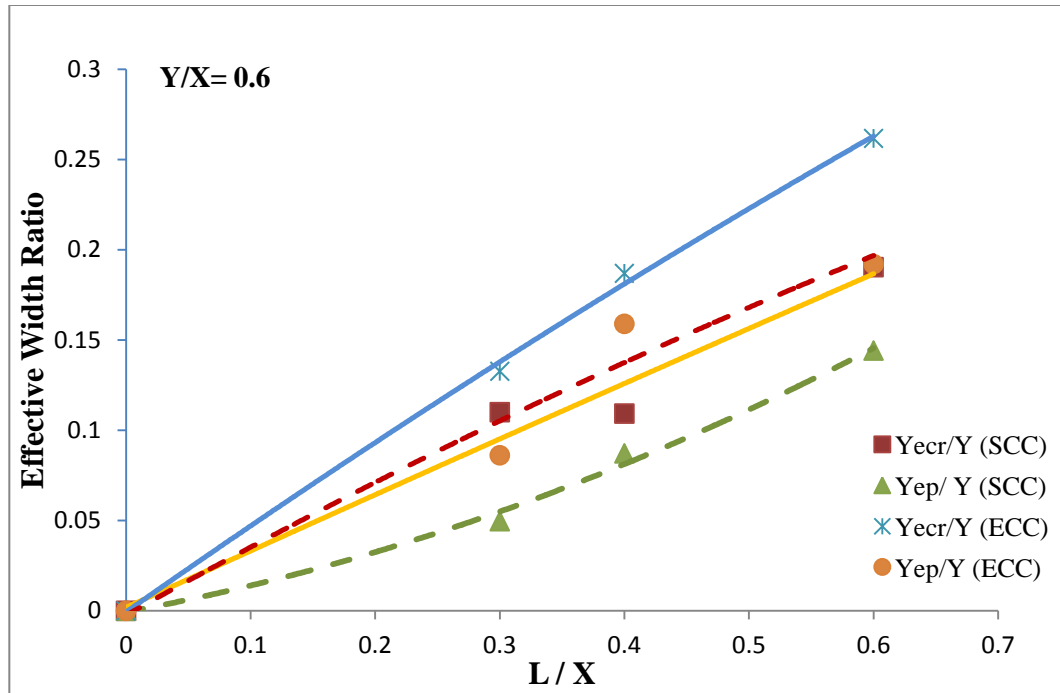


Figure 5.6: Comparison of effective width of ECC/SCC slab at cracking and post-yielding stages as function of L/X

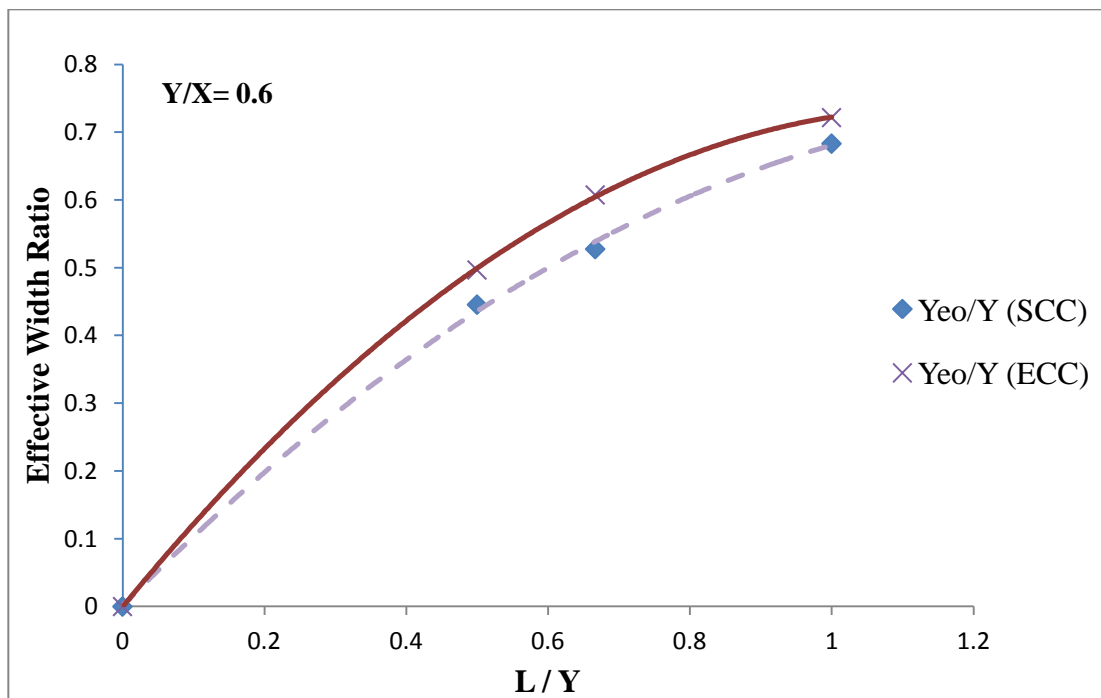


Figure 5.7: Comparison of effective width of ECC/SCC slab at pre-cracking stage as function of L/Y

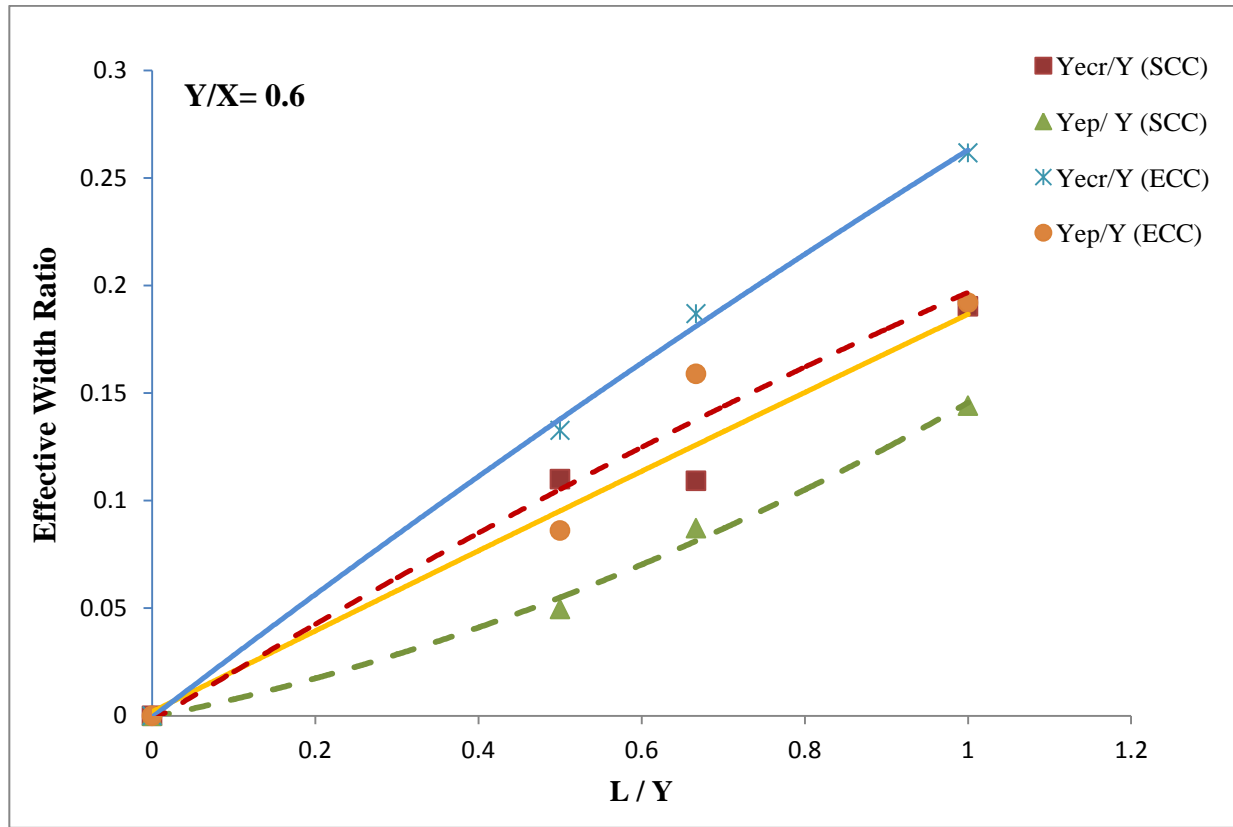


Figure 5.8: Comparison of effective width of ECC/ SCC slab at cracking and post-yielding stages as function of L/Y

Design curves for bending stiffness in the linear and non-linear stages as a function of L/X are developed based on actual test data points and are presented in Figs. 5.9 and 5.10. Bending stiffness increases with the decrease of L/X . Also bending stiffness decreases as the model specimens passes through pre-cracking, cracking and post-yielding.

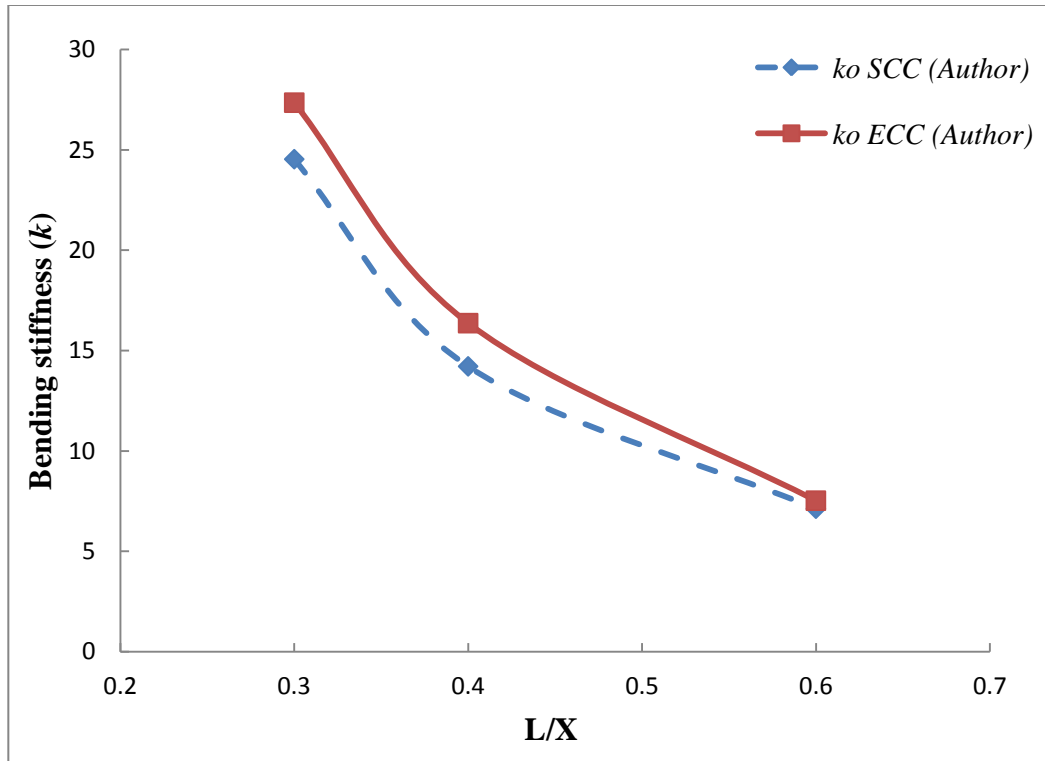


Figure 5.9: Comparison of flexural stiffness at pre-cracking stage (Y/X 0.6)

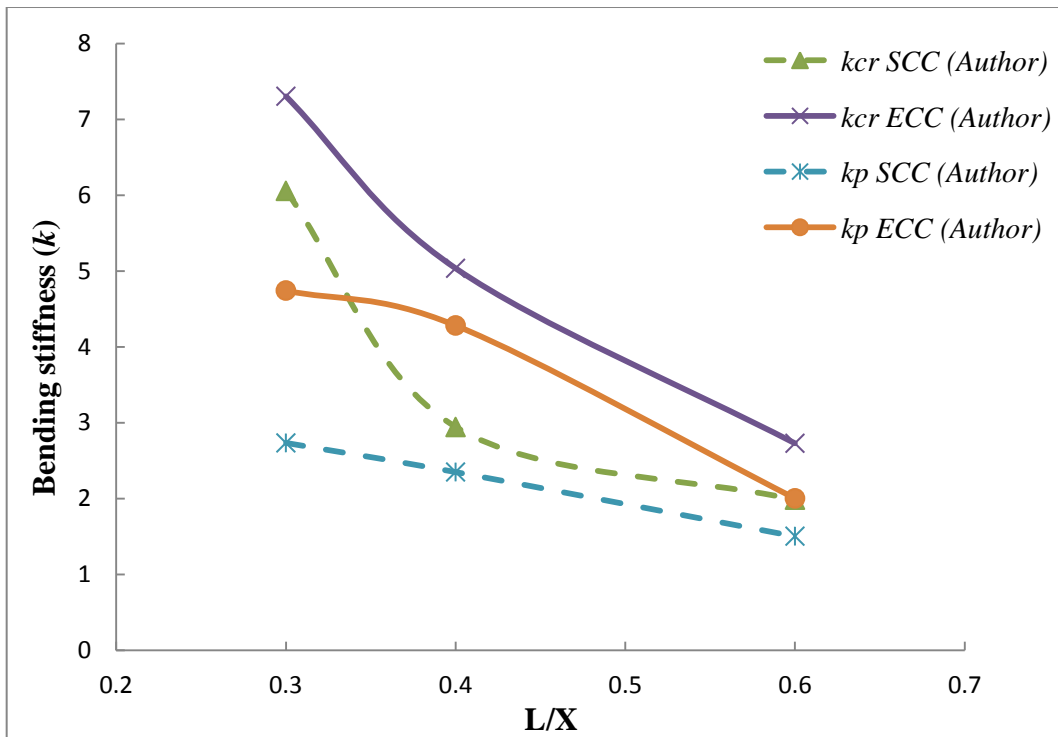


Figure 5.10: Comparison of flexural stiffness at pre-cracking stage ($Y/X=0.6$)

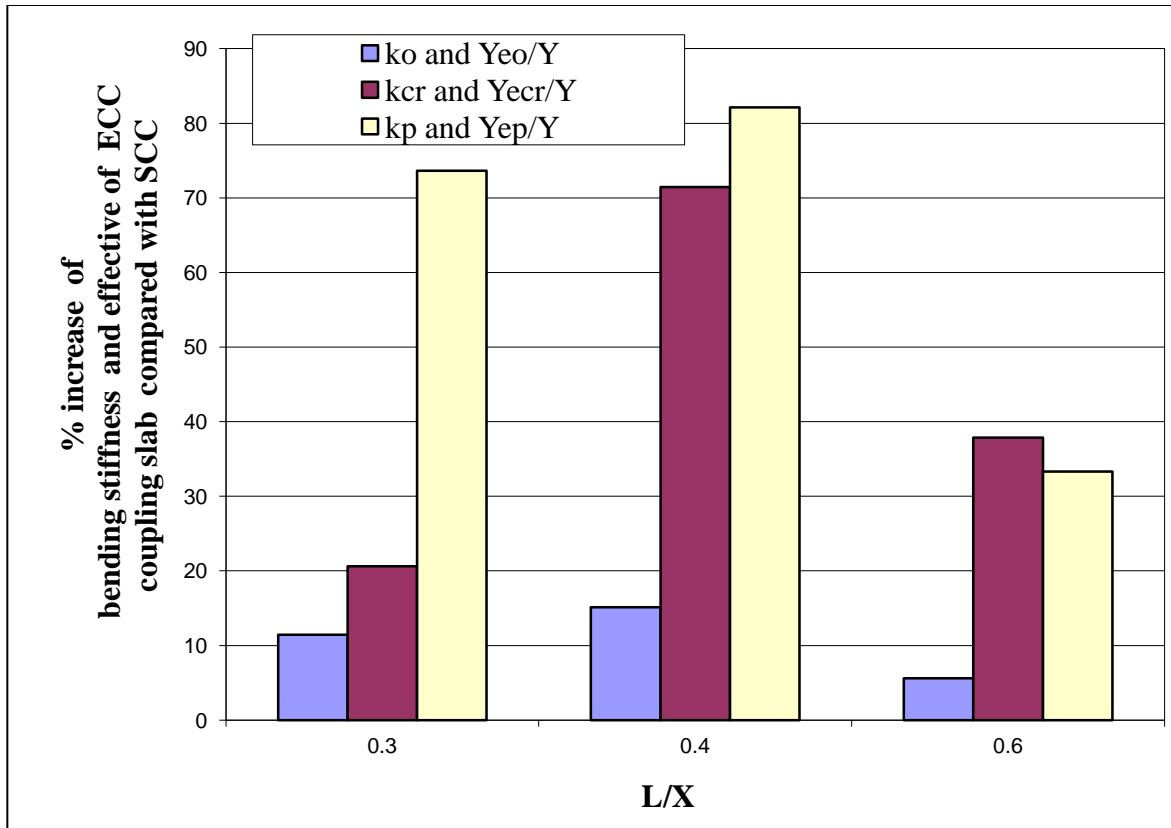


Figure 5.11: Bending stiffness and effective width of ECC coupling slab compared with SCC

In general, model specimens with ECC showed higher effective width and bending stiffness in pre-cracking, cracking and post-yielding stages compared with their SCC counterparts (Fig. 5.11). ECC coupling slabs showed higher (an increase of between 6% and 15% with a mean value of 11%), cracking stiffness/effective width (an increase of between 21% and 71% with a mean value of 43%), and post-yielding stiffness/effective width (an increase of between 33% and 83% with a mean value of 63%) compared to their SCC counterparts. This signifies that reinforced ECC is more effective than SCC especially in the cracking and post-yielding stages due to its superior strain hardening and crack resisting capabilities. Hence ECC coupling slab will provide more resistance against damage propagation in cracking and post-yielding stages.

5.3 Relationship Between Bending Stiffness in Various Stages

It is attempted to develop a relationship between non-linear stiffness (k_{cr} and k_p) to its linear equivalent k_o . The variation of k_{cr}/k_o as a function of L/X at $Y/X = 0.6$ is shown in Fig. 5.12. k_{cr}/k_o ranges between 0.215 and 0.32 for SCC and 0.27 and 0.36 for ECC model showing almost similar behaviour for both materials at $Y/X = 0.6$.

Figure 5.12 also shows the variation of k_p/k_o as a function of L/X for $Y/X = 0.6$. All numerical data show that the k_p/k_o ranges between 0.11 and 0.21 for SCC specimens and between 0.17 and 0.27 for ECC specimens.

In terms of k_{cr}/k_o and k_p/k_o , SCC specimens have shown higher stiffness degradation compared to pre-cracking stiffness at cracking and post-yielding stages. In general, k_{cr}/k_o and k_p/k_o are found to increase with the increase of L/X which means stiffness degradation will be lower for coupling slab with higher L/X .

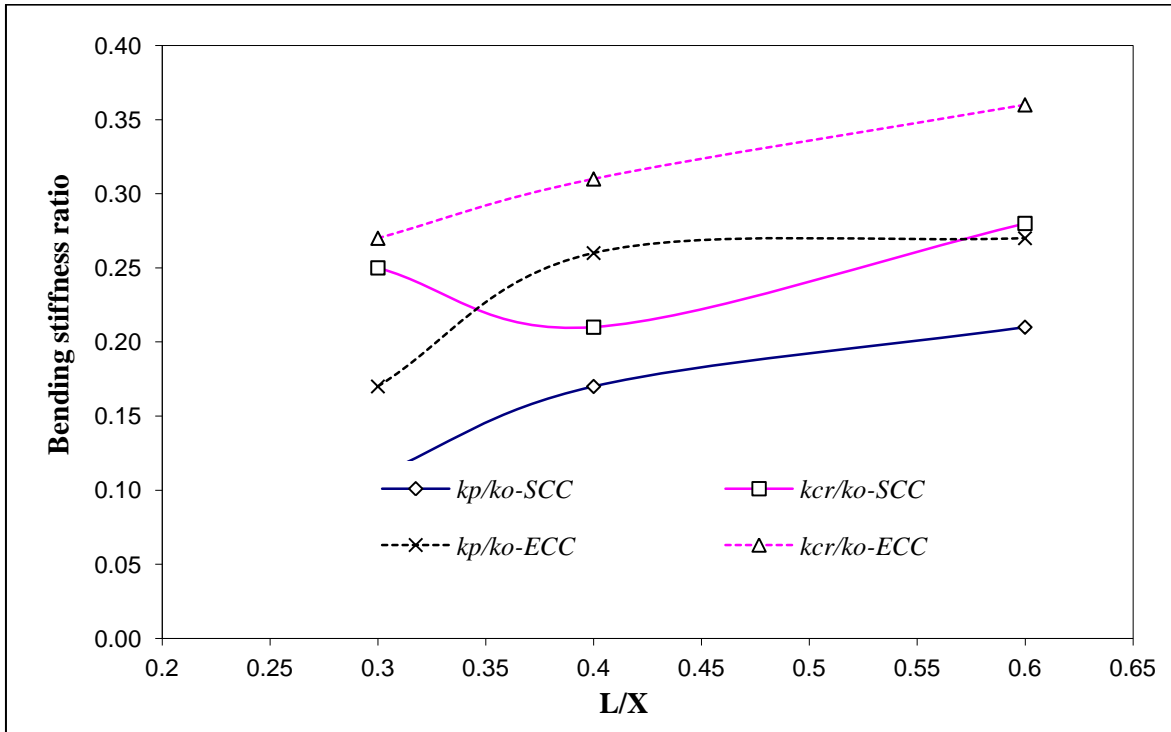


Figure 5.12: Relationship between k_o , k_{cr} and k_p in ECC and SCC specimens

5.4 Comparison of Bending Stiffness and Effective Width

Bending stiffness and effective width of coupling slabs from models tests are compared with those obtained from previous research studies. The pre-cracking stiffness and effective width obtained from model tests should agree with those obtained from Hossain (2003); Coull & Wong (1981) and Qadeer & Smith (1969).

5.4.1 Comparison Pre-cracking Stiffness/Effective Width and Effect of Concrete Types

The pre-cracking stiffness and effective width obtained from model tests should agree with those obtained from Hossain (2003); Coull and Wong (1981) and Qadeer and Smith (1969).

Figure 5.13 compares the pre-cracking stiffness (k_o) obtained from Hossain (2003) and Qadeer & Smith (1969) with those obtained from model tests by the Author. Pre-cracking stiffness from Hossain (2003) showed close agreement with those obtained from Qadeer & Smith (1969) as the variation ranges between 2% and 15%. Bending stiffness gradually decrease as the material passes through pre-cracking, cracking and post-yielding stages. It can be noted from Fig. 5.13 that the pre-cracking bending stiffness (k_o) of ECC is 19.6% to 24.65% higher and of SCC is 11.65% to 16.01% higher than normal concrete (NC) used in Hossain's experimental study. Pre-cracking bending stiffness of ECC coupling slab is 21.40% to 35.24% higher and of SCC is 12.38% to 25.44% higher than their NC counterparts used in Qadeer & Smith study.

Figure 5.14 shows a comparison of the variation of pre-cracking effective width (Y_{eo}/Y) with L/X for constant value of Y/X obtained from author, Hossain (2003) and Coull & Wong (1981). Comparative study shows the same trend of variation of increase of pre-cracking effective width with the increase of L/X . Good agreement is found between Hossain (2003) and Coull & Wong (1981) as the variation in pre-cracking effective of NC coupling slab ranges between 1.0% and 8%. However, pre-cracking effective width of ECC coupling slab is 19.63% to 23.50% higher than their NC counterparts from Hossain and Coull & Wong study. SCC coupling slabs also show on average 13.59% higher pre-cracking effective width compared NC counterparts of Hossain and Coull & Wong.

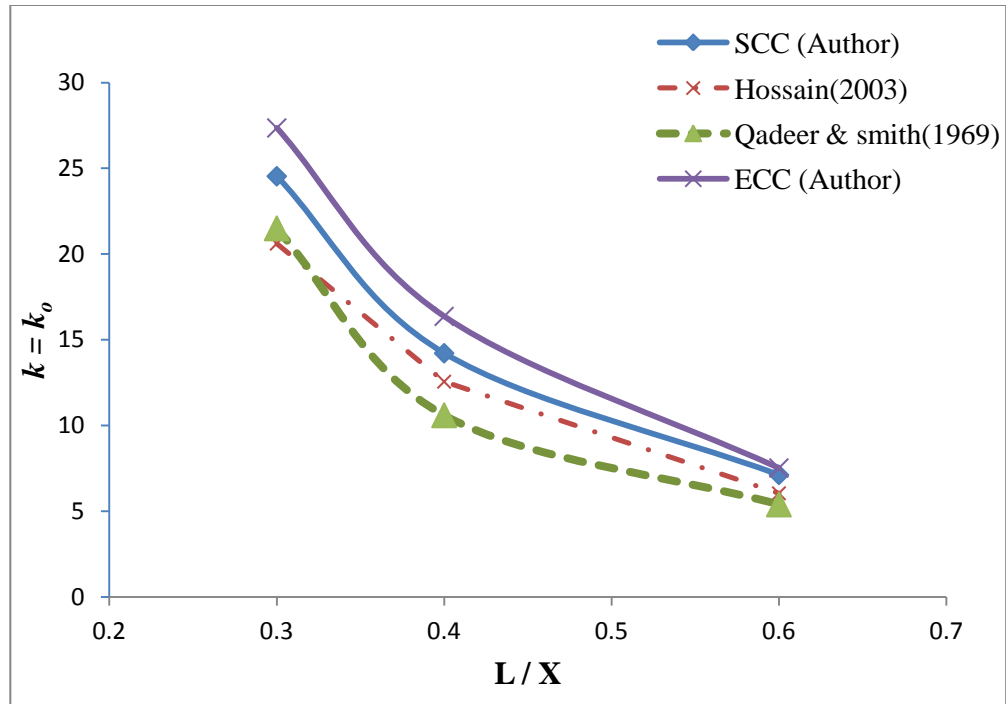


Figure 5.13: Comparison of pre-cracking stiffness of coupling slabs with normal concrete, ECC and SCC

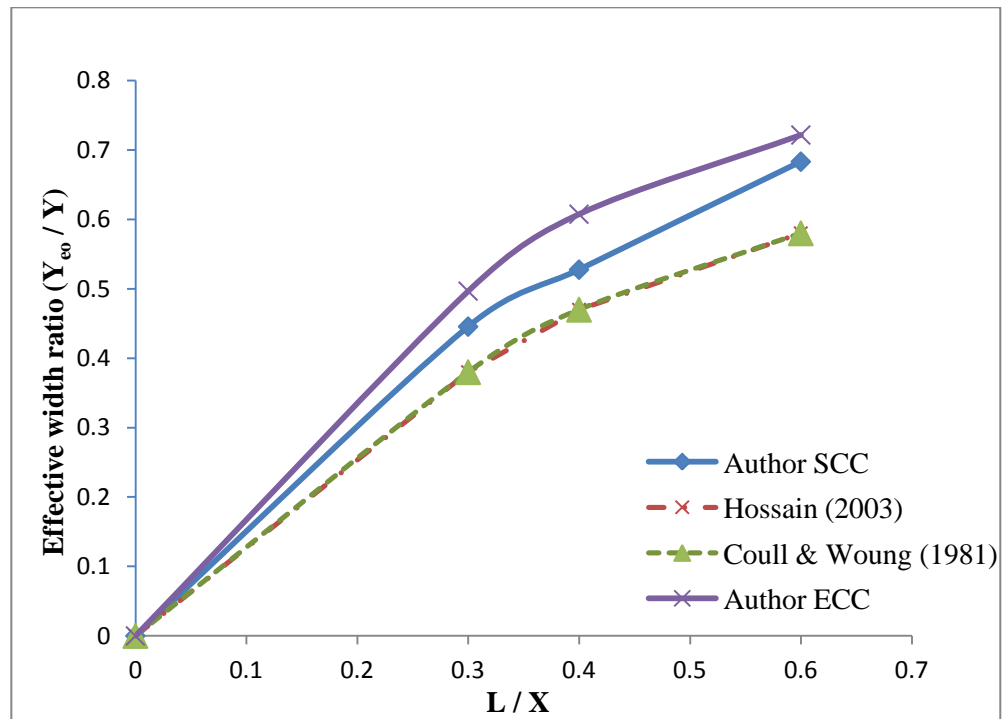


Figure 5.14: Comparison of pre-cracking effective width for different concrete types

Overall, ECC coupling slab exhibited higher pre-cracking stiffness and effective width compared to SCC and NC, NC showing the lowest values.

5.4.2 Comparison Cracking (k_o)/Post-yielding (k_p) and Effect of Concrete Types

Figure 5.15 compares cracking and post-yielding stiffness of ECC and SCC coupling slabs from current study with those of NC counterparts of Hossain (2003). In general, ECC coupling slabs show higher cracking and pre-cracking stiffness compared with their SCC and NC counterparts with NC showing the lowest stiffness. This is attributed to ECC's high strain hardening capacity and higher damage resistance due to micro-cracking as well as fiber bridging that reduces strain/stress in the reinforcing steel in the cracking and post-yielding stages.

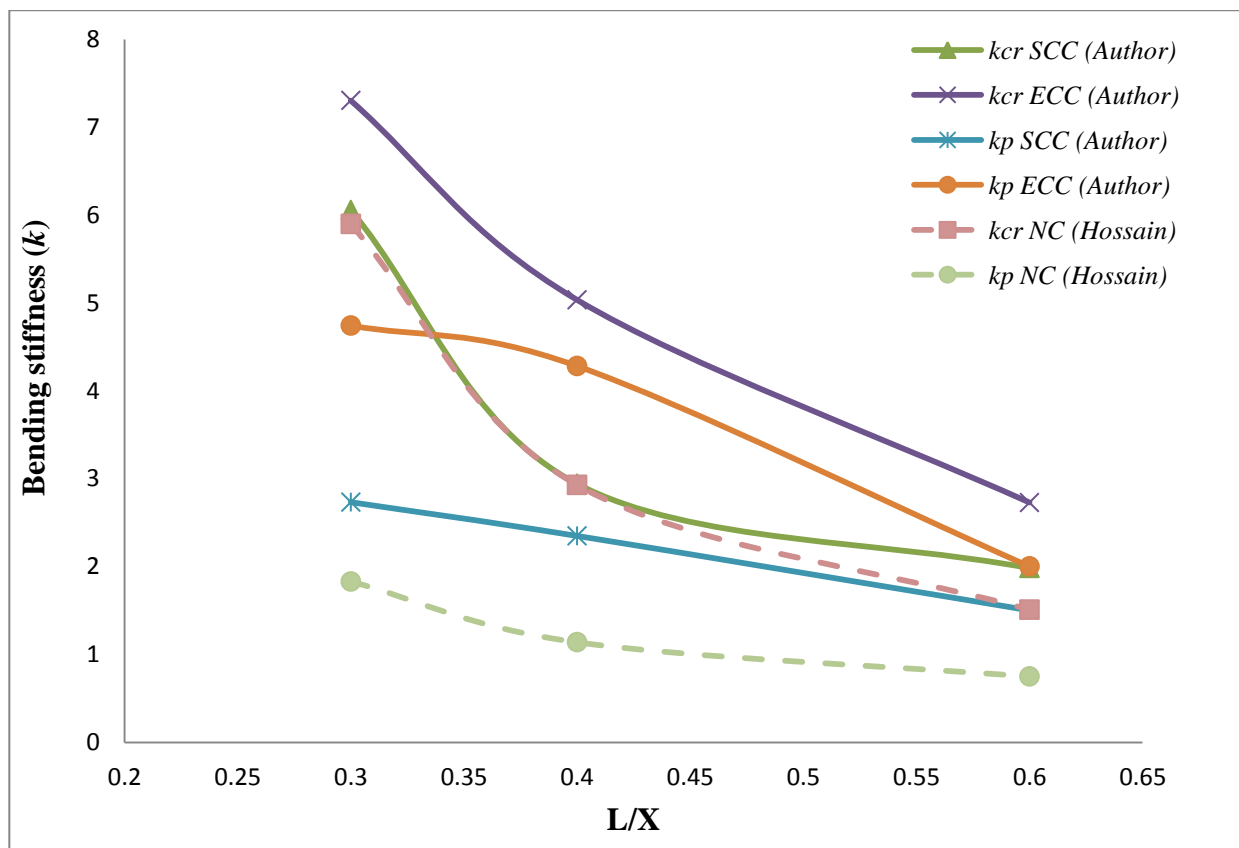


Figure 5.15: Comparison of cracking and post-yielding stiffness and effect of concrete types

5.5 Chapter Summary

Bending stiffness and effective width of coupling slabs in pre-cracking, cracking and post-yielding stages are described. The effect of concrete types (ECC, SCC and NC) on bending stiffness and effective is described based on current and previous research studies. Charts and tables are provided for the prediction of bending stiffness and effective width at various stages ranging from pre-cracking to post-yielding stages. Stiffness and effective width decreases as material passes from pre-cracking and to post yielding stages and also with the increase of L/X (for constant Y/X). ECC coupling slabs showed superior performance compared to SCC, and SCC counterparts in terms of higher bending stiffness and effective width from pre-cracking to post -yielding stage. The bending stiffness and effective width presented in this study are used to analyze the stress, deflection and load carrying capacity of a full-scale coupled shear wall building having varying geometric dimension and materials (ECC and SCC) in the pre-cracking, cracking and post-yielding stages next chapter.

CHAPTER 6

ANALYSIS OF COUPLED SHEAR WALL BUILDING IN PRE-CRACKING, CRACKING AND POST-YIELDING STAGES BY CONTINUOUS MEDIUM METHOD

6.0 General

This chapter presents load, stress and deflection analyses of full-scale 20-storey ECC and SCC coupled shear wall buildings (replicating the 1/12th scale models used in experiments) by using continuous medium method. The performance of ECC and SCC buildings is described based on stress/moment generation in shear walls, laminar shear flow development and lateral deflection along the height of the building at pre-cracking, cracking and post-yielding stages. The wind load resistance and associated lateral deflection of ECC and SCC building at yielding stages are also compared to illustrate ductility and strength characteristics.

6.1 Full-scale Prototype 20-storey Coupled Shear Wall Building with Geometric Dimensions and other Specifications

Full-scale prototype 20-storey building used for the theoretical analysis by continuous medium method (Choudhury 1967a,b; Hossain 2003) is an exact replica of 1/12th scale model specimens, tested experimentally in this study. The prototype building is analyzed for three geometric configurations similar to model specimens with Y/X of 0.6 and L/X of 0.3, 0.4 and 0.6 as shown in Table 6.1. The three prototype buildings have identical symmetric planar shear walls. The dimensions of the full-scale building with geometric parameters are shown in Table 6.1. The length (X) and width (Y) of the coupling slab are 12 m and 7.2 m, respectively. The thickness of wall (t_w), storey height (h) and thickness of coupling slab (t) are 0.9 m, 3 m and 0.72 m, respectively. The plan and elevation of the 60 m high 20-storey coupled shear wall building is presented in Fig. 6.1.

Two types of analyses are performed to investigate the comparative performance of ECC and SCC building. They are:

- Load, stress and deflection analysis under an assumed wind load applied to the building at pre-cracking, cracking and post-yielding stages.
- Determination of wind load and deflection capacities of yielded buildings.

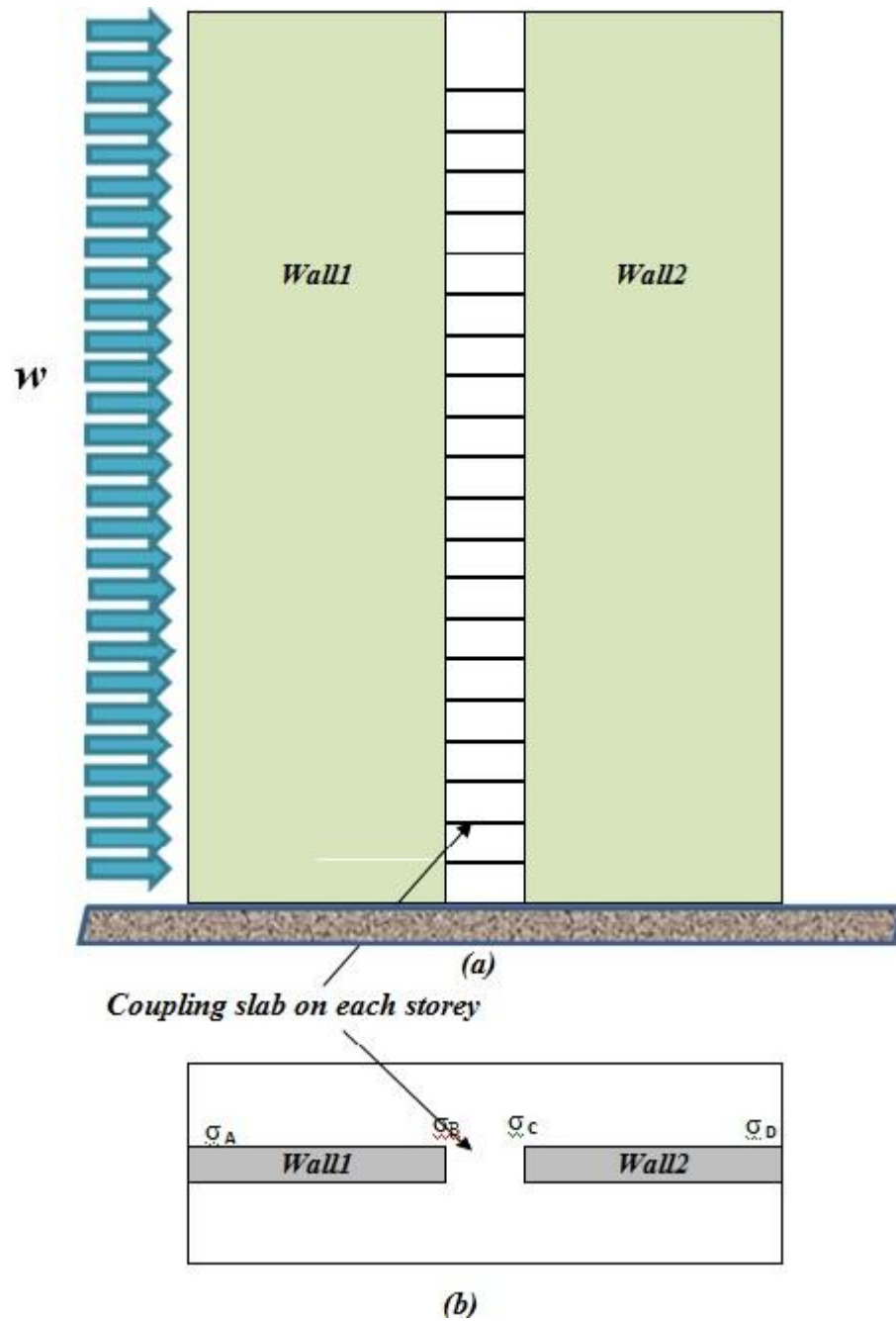


Figure 6.1: (a) Side view of the 20 storey building with uniformly distributed static wind load
(b) Cross-section floor plan of the building

The equations and charts (presented in Chapter 2) for analysis of coupled shear wall building using continuous medium method are used.

Table 6.1: Geometrical parameters of full-scale prototype coupled shear wall building

Building	Design Parameters			Corridor Opening	(L+W)	Width of the slab	Effective Width (Y_e)		
	Y/X	L/X	L/Y	L or b	l	Y	Y_{eo}	Y_{ecr}	Y_{ep}
				m	m	m	m	m	m
SCC-1	0.6	0.30	0.50	3.60	7.80	7.20	3.21	0.79	0.36
SCC-2		0.40	0.67	4.80	8.40	7.20	3.80	0.79	0.63
SCC-3		0.60	1.00	7.20	9.60	7.20	4.92	1.37	1.04
ECC-1	0.6	0.30	0.50	3.60	7.80	7.20	3.58	0.96	0.62
ECC-2		0.40	0.67	4.80	8.40	7.20	4.37	1.35	1.14
ECC-3		0.60	1.00	7.20	9.60	7.20	5.20	1.88	1.38

6.2 Load, Stress and Deflection Analysis of 20-Storey Building

The SCC and ECC buildings are analyzed for stresses in shear walls, wall moments, shear flow (q) and lateral deflection (y) at various storeys' height of the building at pre-cracking, cracking and post-yielding stages of the building. Table 6.1 also presents effective of the coupling slab (Y_e) of the prototype building found from the model tests and design charts presented in previous chapters at pre-cracking (Y_{eo}), cracking (Y_{ecr}) and post-yielding stages (Y_{ep}).

The pre-cracking, cracking and post-yielding stages of the building are simulated by performing analyses using Y_{eo} , Y_{ecr} and Y_{ep} from Table 6.1. Due to similarity of the behaviour of building under lateral load, analysis is performed on SCC and ECC building with L/X of 0.3. An equivalent wind load (w) of 20 kN/m was applied along the height of the building as lateral load. The material properties of SCC and ECC used in the analysis are derived from the experiments.

6.2.1 Stresses in Shear Walls

Based on Eqs. 2.18, 2.19 and 2.20, stresses (σ) developed at various locations of the shear walls as indicated in Fig. 6.1 (Points A, B, C and D) are calculated.

Generally, points near the inner edges of the shear wall (B and C) will be subjected to higher stresses compared with those at A and D. Figs. 6.2 and 6.3 show the stress development at the inner edges (σ_B and σ_C) of the walls at each storey level at pre-cracking, cracking and post-

yielding stages of ECC and SCC buildings, respectively. Stresses in shear walls increase from top storey to the ground floor and shear walls at lower floors are subjected to higher stresses compared to upper ones (Figs. 6.2 and 6.3). Shear walls in ECC building slabs exhibit lower stress compared with their SCC counterparts in all pre-cracking, cracking and post-yielding stages. This is associated with the higher effective width of ECC coupling slabs at various stages as a consequence of its higher resistance to damage compared with SCC.

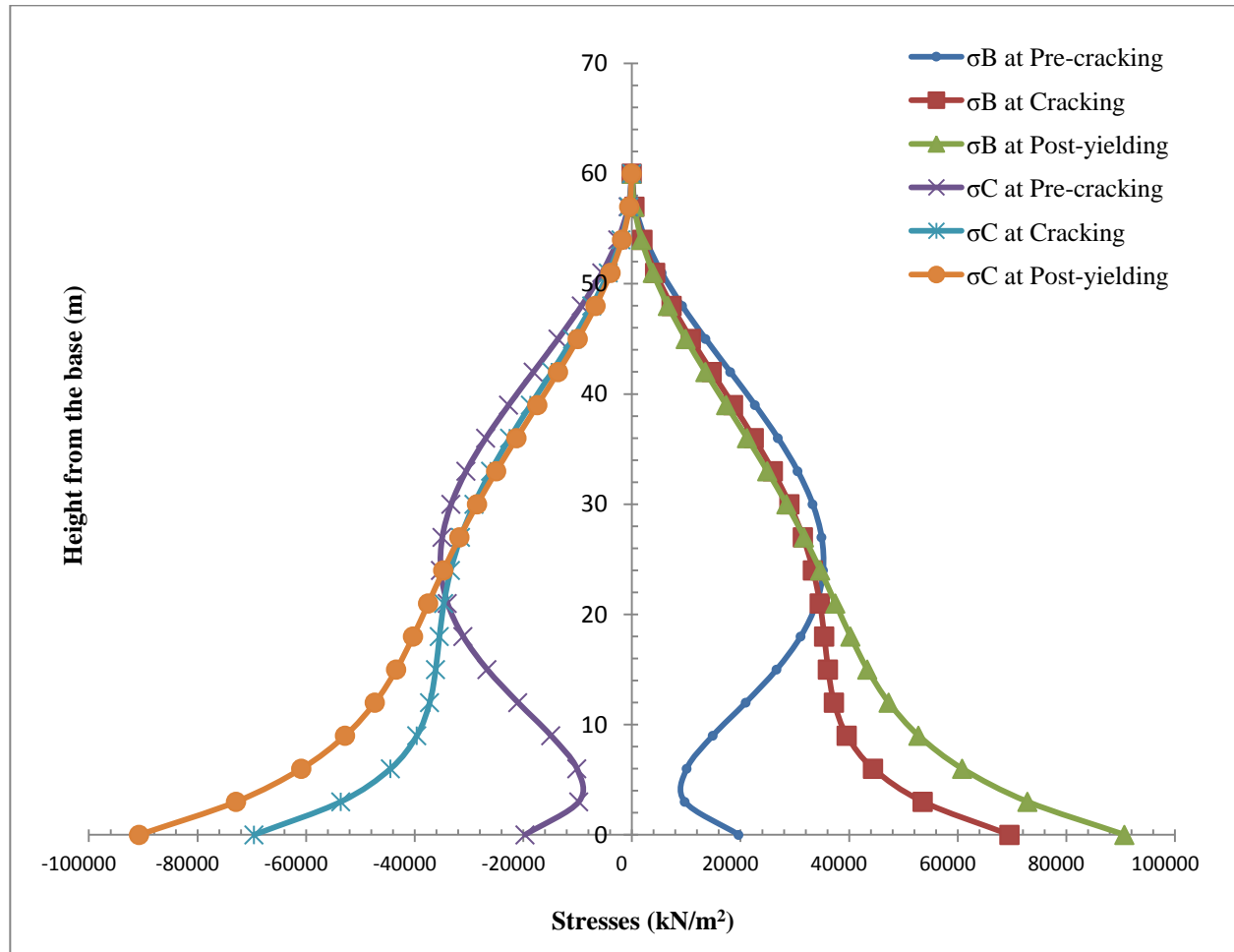


Figure 6.2: Stresses at inner edges of the shear walls at each storey (ECC, $L/X = 0.3$)

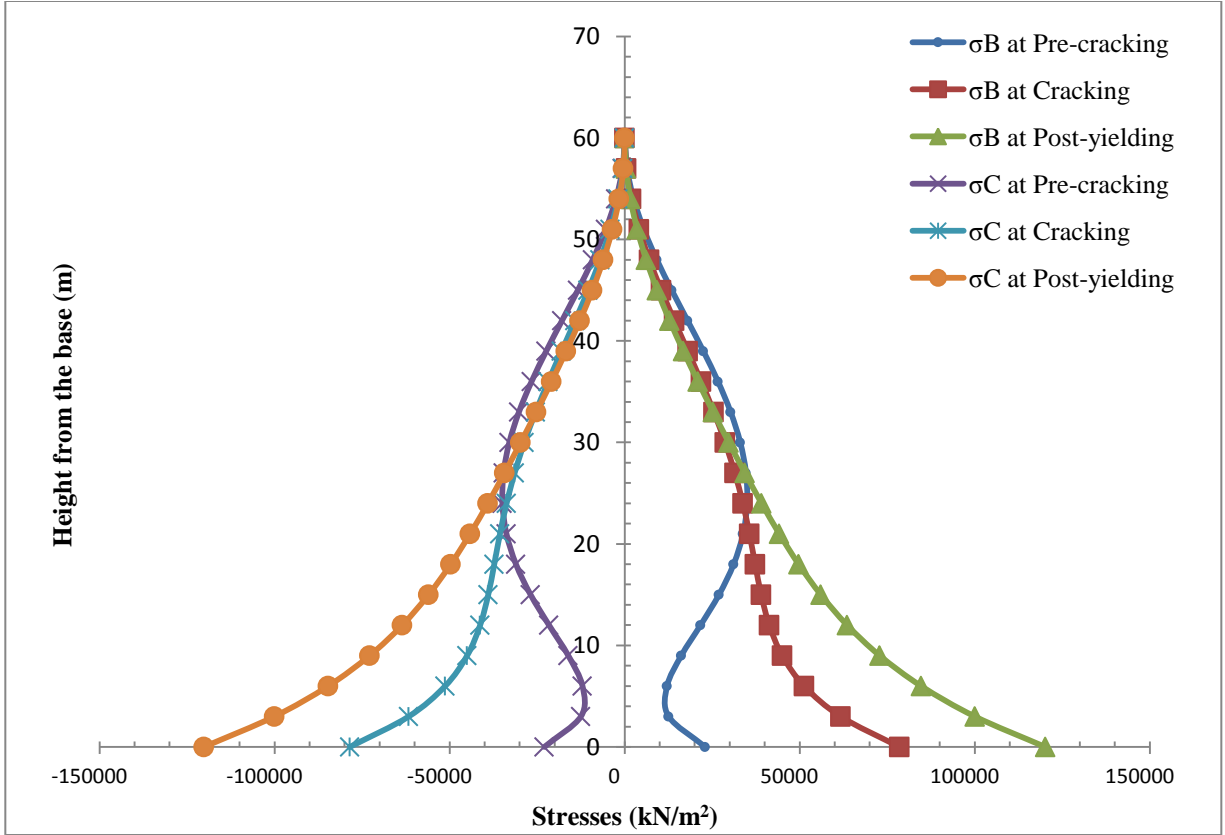


Figure 6.3: Stresses at inner edges of the shear walls at each storey (SCC, $L/X = 0.3$)

6.2.2 Moments in Shear Walls

From Equation 2.17, induced moments M_1 and M_2 of the Wall1 and Wall2, respectively are calculated by using Eq. 2.17 (presented in Chapter 2) and results are plotted in Figs. 6.4 and 6.5 for ECC and SCC building, respectively. ECC and SCC building show similar trend of variation of moment development in the shear walls along the height. The top storey shows also the development of negative moment. The point of zero moment is found to move towards the lower floor (14th floor at the pre-cracking stage to around 10th floor at the post-yielding stage). Shear walls in SCC building develop higher moments compared with their ECC counterparts, which is expected. Wall moment also increases because of weaker beams in the cracking and post-yielding stages.

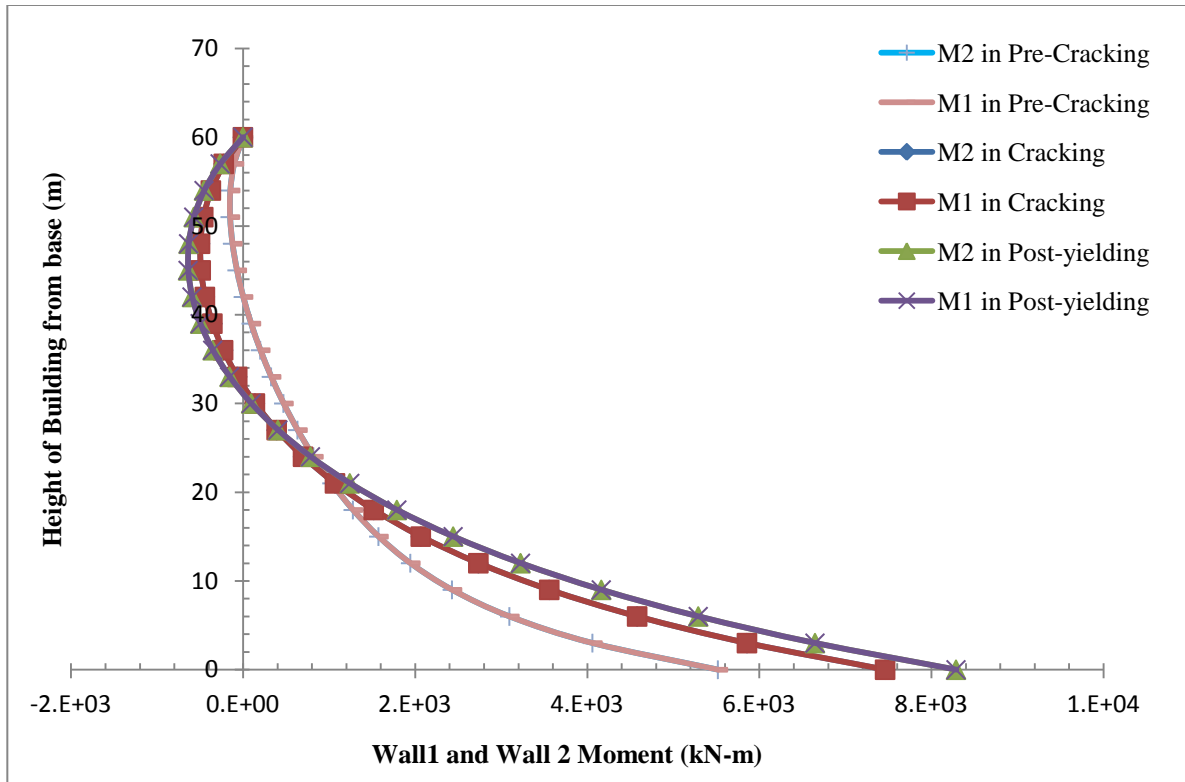


Figure 6.4: Moment developed at walls 1 and 2 at each storey (ECC: $L/X = 0.3$)

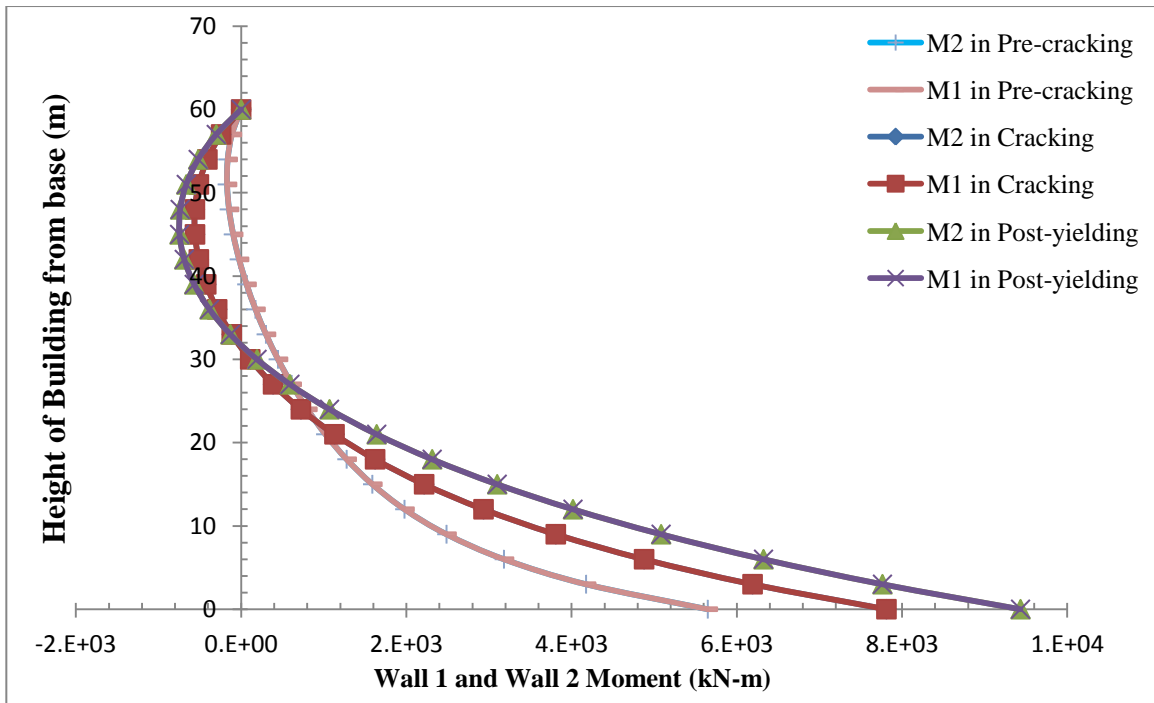


Figure 6.5: Moment developed at walls 1 and 2 at each storey (SCC: $L/X = 0.3$)

6.2.3 Shear Flow Development

The shear flow (q) in ECC and SCC building is derived based on Eq. 2.22 and using factor K_3 from Eq. 2.22a. The shear flow is then multiplied by storey height to obtain storey shear load (Q) at each storey. Figs. 6.6 and 6.7 show the variation of shear flow along the height for ECC and SCC building, respectively and compared in Fig. 6.8 for post-yielding stage. The maximum shear flow occurs at 5th storey level of the buildings at pre-cracking stage. The maximum shear flow level moves towards the base from pre-cracking (from 5th floor) to post-yielding stages of the building (to 8th floor). The shear floor development is higher in ECC building compared to SCC in all the stages. At post-yielding stage, the maximum shear flow in ECC building is 87.31 kN/m compared to 85.92 kN/m of SCC (showing an increase of 2%). At cracking stage, the maximum shear flow in ECC building is 65.39 kN/m compared to 61.83 kN/m of SCC (showing an increase of 5.44%) while in post-yielding stage, the maximum shear flow in ECC is 57.38 kN/m compared to 47.55 kN/m of SCC (showing an increase of 17%). The location of maximum shear flow move towards the top of the building as cracking and yielding continues. The shear flow is lower in yielding stage compared to pre-cracking stage except near the top of the building.

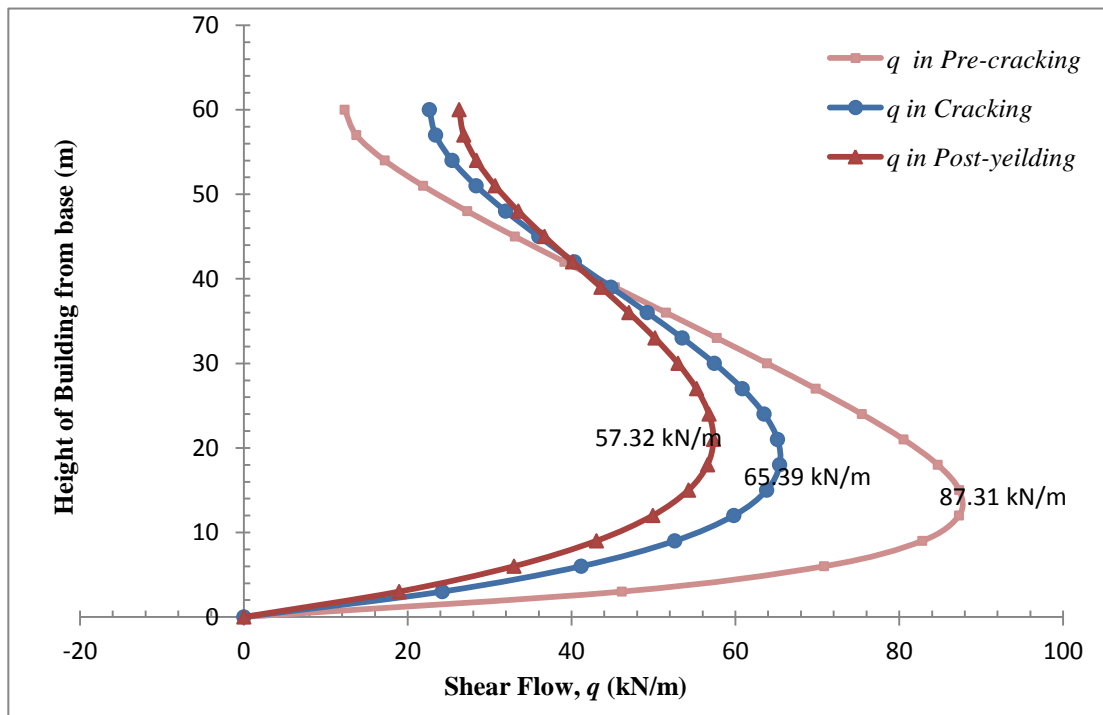


Figure 6.6: Laminar shear flow (q) at each storey (ECC: $L/X = 0.3$)

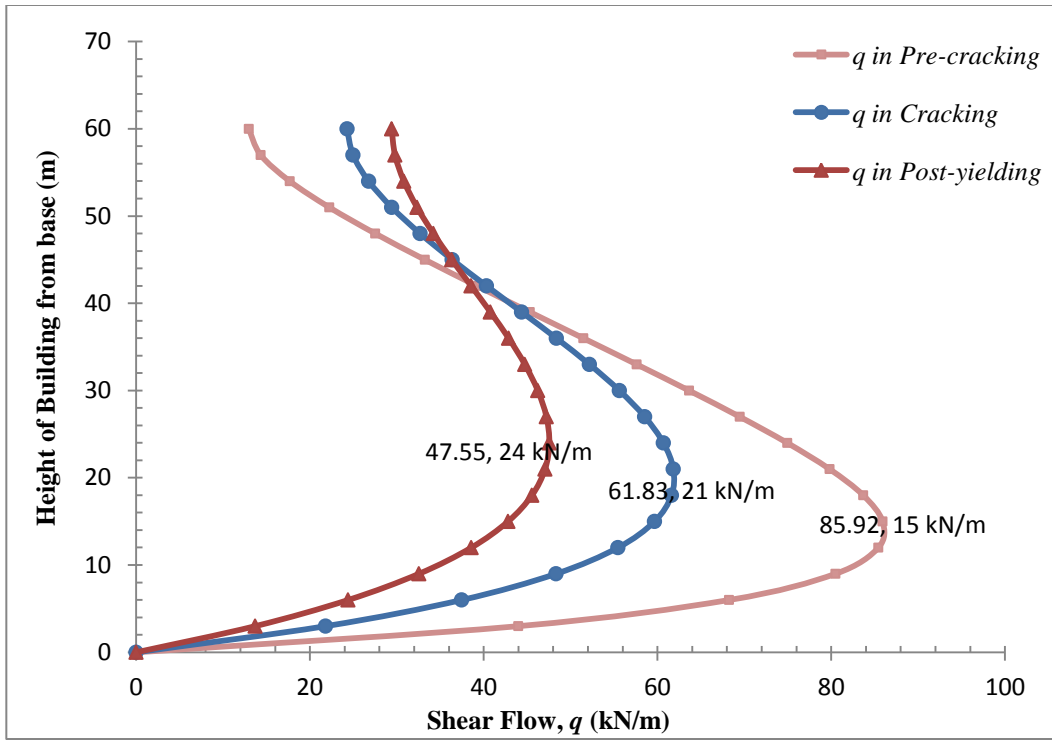


Figure 6.7: Laminar shear flow at each storey (SCC: $L/X = 0.3$)

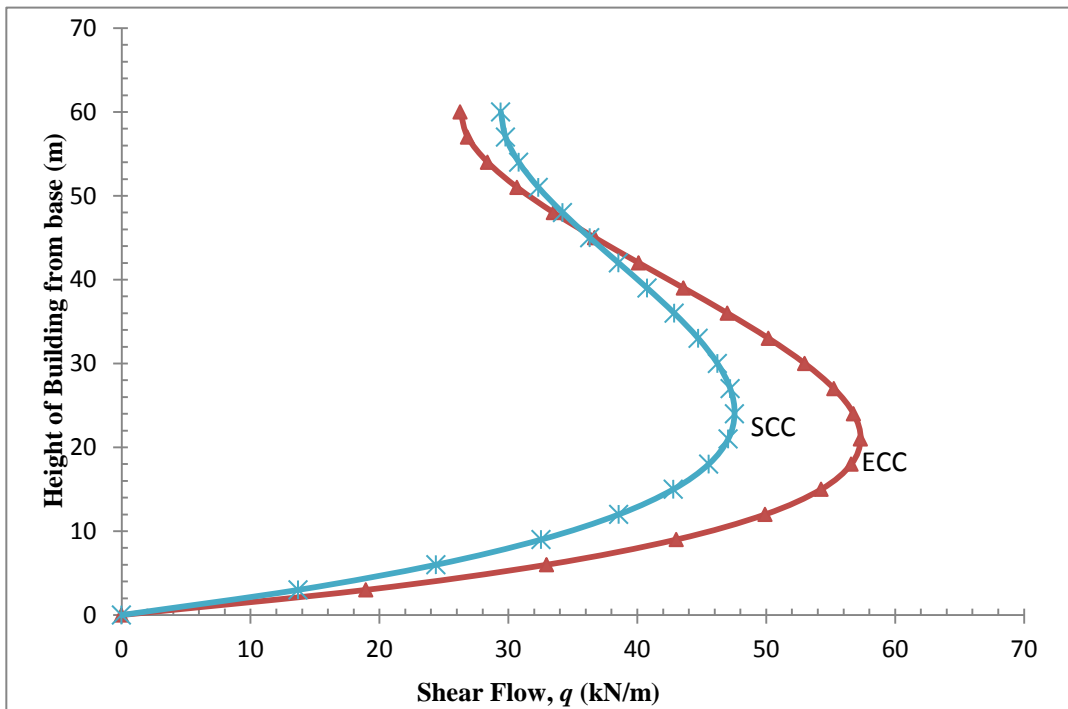


Figure 6.8: Comparison of shear flow at each storey for ECC and SCC ($L/X = 0.3$)

6.2.4 Lateral Deflection of the Building

Lateral deflection (y) of the building subjected to wind load is calculated using Eq. 2.23a at each storey level and maximum deflection (y_{max}) at the top is calculated using Eq. 2.23b or using the factor K_4 from the chart shown in Fig. 2.12 at pre-cracking, cracking and yielding stages.

The variation of lateral deflection along the height of the ECC and SCC building is shown in Figs. 6.9 and 6.10, respectively. Both ECC and building show similar trend of variation. In general, ECC building shows higher deflection compared with SCC at all stages. At post-yielding stage, ECC building deflects 16.2 mm (at the top) compare to 15.2 mm of SCC (Figs. 6.9 and 6.10)

The maximum deflections at the top for ECC building in pre-cracking, cracking and post-yielding stages are 11 mm, 14.2 mm and 16.2 mm compared to 8.6 mm, 11.6 mm and 15.2 of SCC counterparts, respectively. ECC building shows better ductility compared to SCC ones in terms of higher maximum deflection (28% higher in pre-cracking, 23% higher in cracking and 7% higher in post-yielding stage).

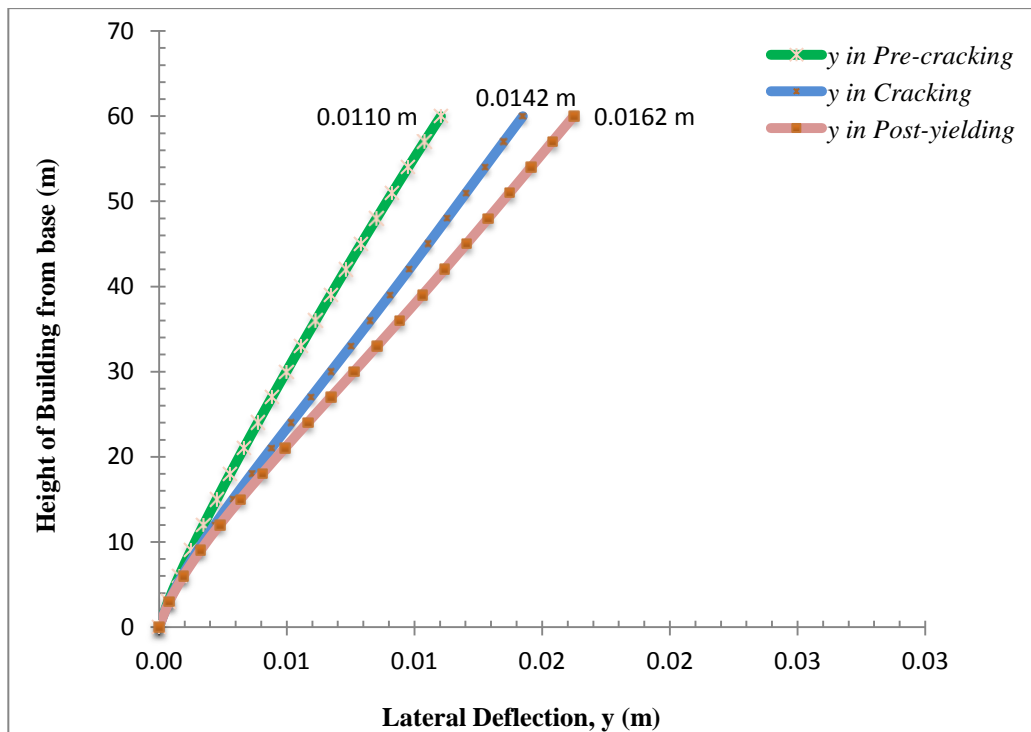


Figure 6.9: Lateral deflection along the height of building at each stage (ECC: $L/X= 0.3$)

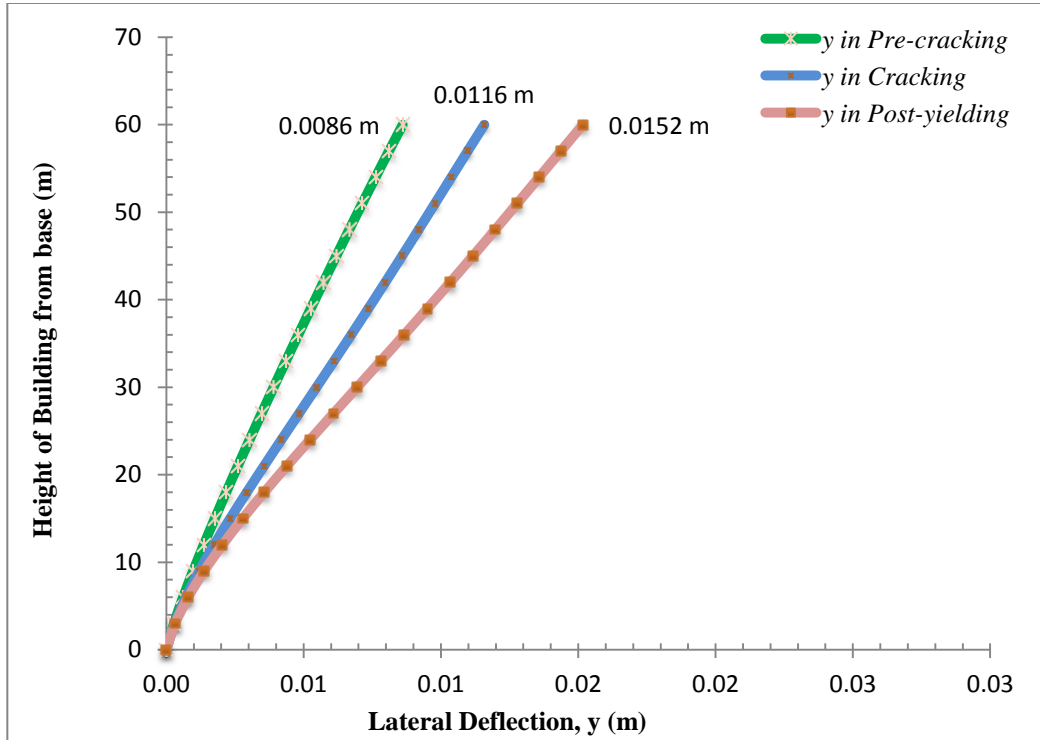


Figure 6.10: Lateral deflection along the height of building at each stage (SCC: $L/X= 0.3$)

Analysis has also been conducted to compare the lateral deflection along the height of both ECC and SCC building with L/X of 0.3, 0.4 and 0.6 at pre-cracking, cracking and post-yielding stages. Fig. 6.11 compares the lateral deflection of ECC and SCC building at post-yielding stages from such analyses for illustration. ECC building shows more ductile behaviour in terms of deflection compared to SCC counterparts at all L/X while other geometric parameters are kept constant.

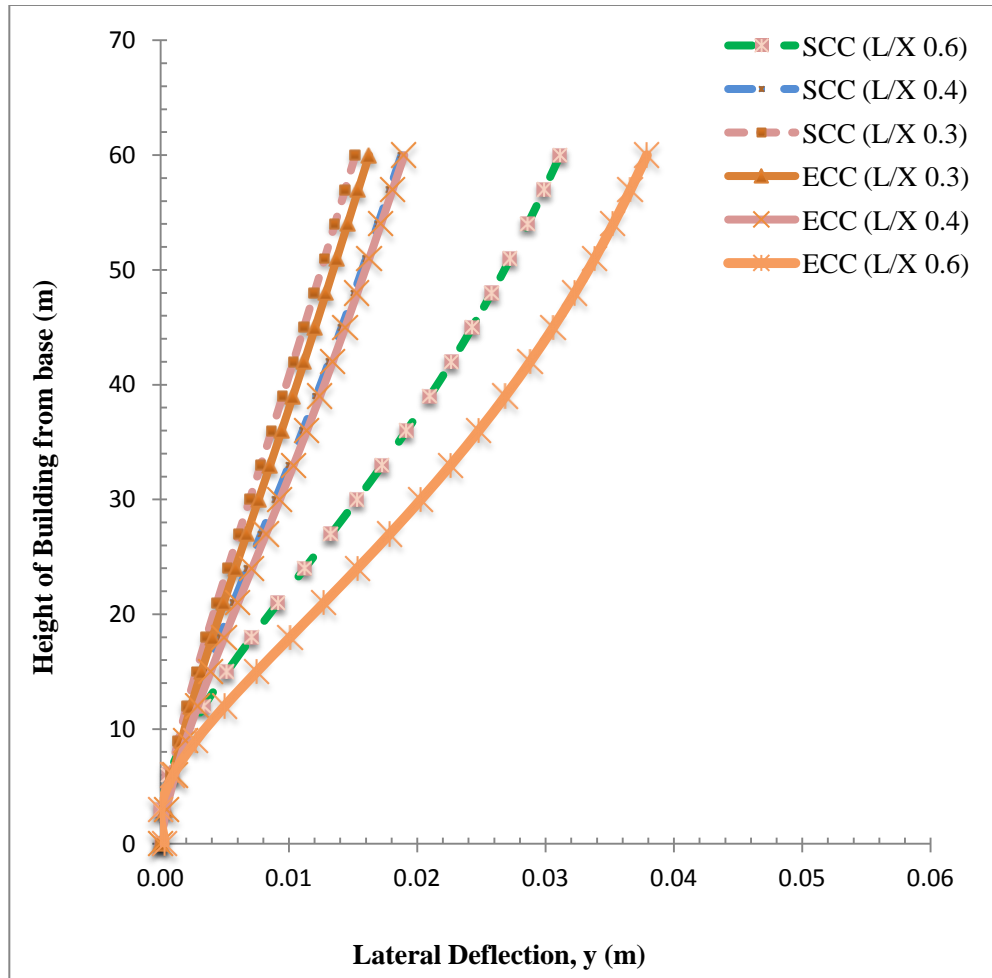


Figure 6.11: Post-yielding lateral deflection of ECC and SCC building with different L/X

6.3 Wind Load and Deflection Capacity Analyses of Yielded Coupled Shear Wall Building

Wind load and deflection capacities of ECC and SCC coupled shear wall buildings are determined by using experimental load capacity and by analysis using continuous medium methods. A total of six prototype 20-storey yielded buildings (three ECC and three SCC) as shown in Table 6.1 with different L/X (0.3, 0.4 and 0.6) with constant L/X (0.6) are analyzed.

A yielded building is analyzed based on consumed effective width ($Y_{ep\ cal}$) as defined in Eq. 6.1 to bring up to the yielding stage. The effective widths ($Y_{ep\ cal}$) of the buildings are presented in Table 6.1.

$$Y_{ep\ cal} = Y(1 - Y_{ep}/Y) \quad (6.1)$$

The ultimate load (Q_{exp}) obtained from experimental SCC and ECC model tests are used to calculate ultimate load (Q_a) and shear flow (q_a) of 20-storey full-scale prototype buildings. All the loads and shear flow values are summarized in Table 6.1.

Extensive trial analyses of all six ECC and SCC building are conducted using continuous medium method to find out the ultimate wind load carrying capacity (collapse load) of the building that generates a shear flow equal to the maximum shear flow ' q_a '. It is assumed that the failure of the building occurs in coupling slabs. The wind load carrying capacity (w) of ECC and SCC yielded buildings are summarized in Table 6.1. The maximum deflections at the top of the building when subjected to ultimate wind load (w) are also calculated and presented in Table 6.1.

Table 6.2: Geometrical parameters and results of wind load capacity & deflection at yielded point

Model No	Y/X	L/X	Ultimate load from experimental models	20-storey full-scale coupled shear wall building					
				Ultimate load of prototype building based on expt.	Max shear flow based on expt.	Yielded Stage			
						Effective Storey	Effective width	Wind load carrying capacity	Deflection at the top
			Q_{exp}	Q_{exp}	q_{exp}		$Y_{ep\ cal}$	w	y_{max}
			kN	kN	kN/m		m	kN/m	Mm
SCC-1	0.6	0.3	11.6	139.2	46.4	4	6.84	9.67	3.86
SCC-2		0.4	10.94	131.28	43.76	4	6.57	9.64	4.49
SCC-3		0.6	10.6	127.2	42.4	4	6.16	9.62	6.68
ECC-1	0.6	0.3	27.1	325.2	108.4	4	6.58	22.67	11.78
ECC-2		0.4	19.59	235.08	78.36	4	6.06	17.48	10.71
ECC-3		0.6	17.63	211.56	70.52	3	5.82	14.76	14.02

It can be noted that the maximum wind load capacity of SCC building is about 9.7 kN/m which is very close to the design wind load of 8.8 kN/m for prototype building of small scale tests. It is found from Table 6.2 and Fig. 6.12 that the wind load required to 'yield' an ECC building is much higher than SCC building which signifies that ECC buildings are more stronger than their

SCC counterparts. Wind load (w) needed to yield ECC buildings is 1.5 to 2.4 times higher than its SCC counterparts when L/X increases from 0.3 to 0.6 (Fig. 6.13). The maximum deflection at the top of the yielded ECC building is 2.1 to 3.1 times higher than its ECC counterparts (Fig. 6.13). It is found that wind load carrying capacity decreases and deflection at the top increases with the increase of L/X when Y/X is kept constant (Figs. 6.12 and 6.14). ECC buildings are found to be 1.5 to 2.4 times stronger and at the same time, 2 to 3 times more ductile than their SCC counterparts.

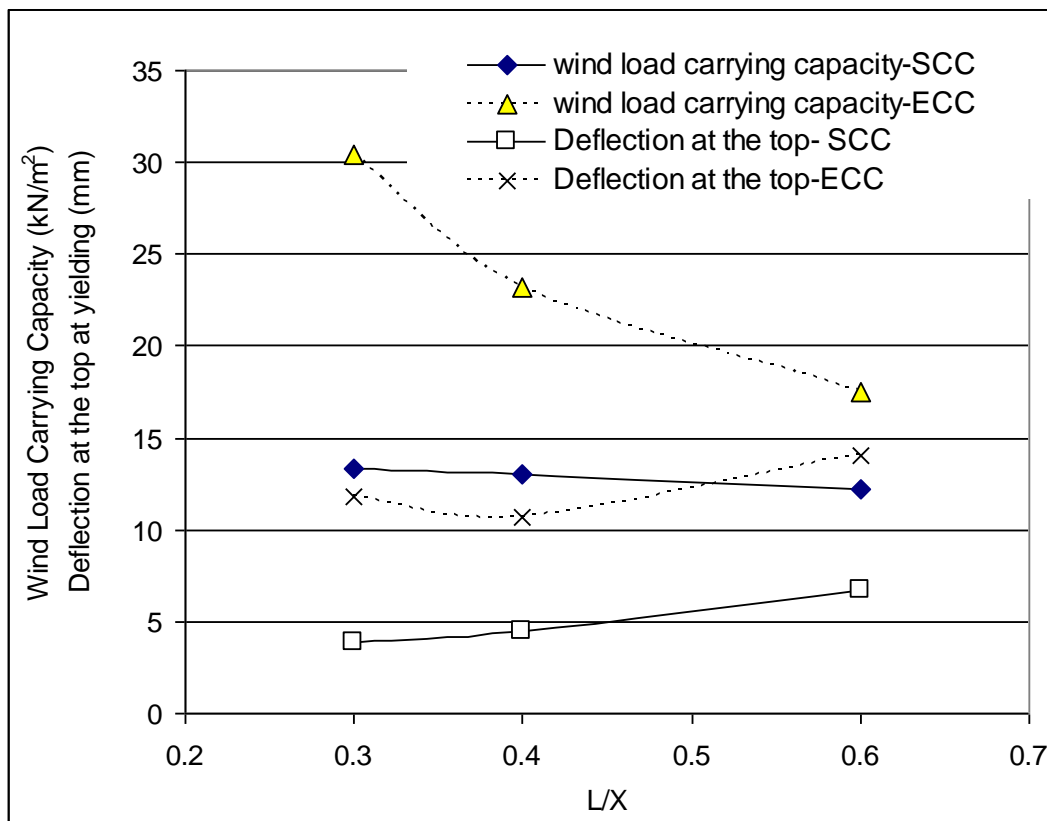


Figure 6.12: Required wind load for yielding and the top deflection at yielding

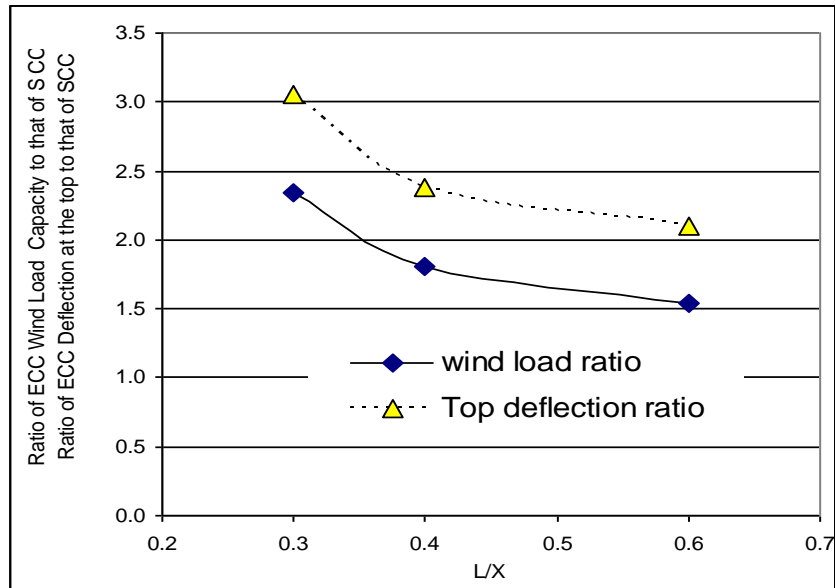


Figure 6.13: Comparative performance of ECC and SCC building in terms of load and deflection capacity

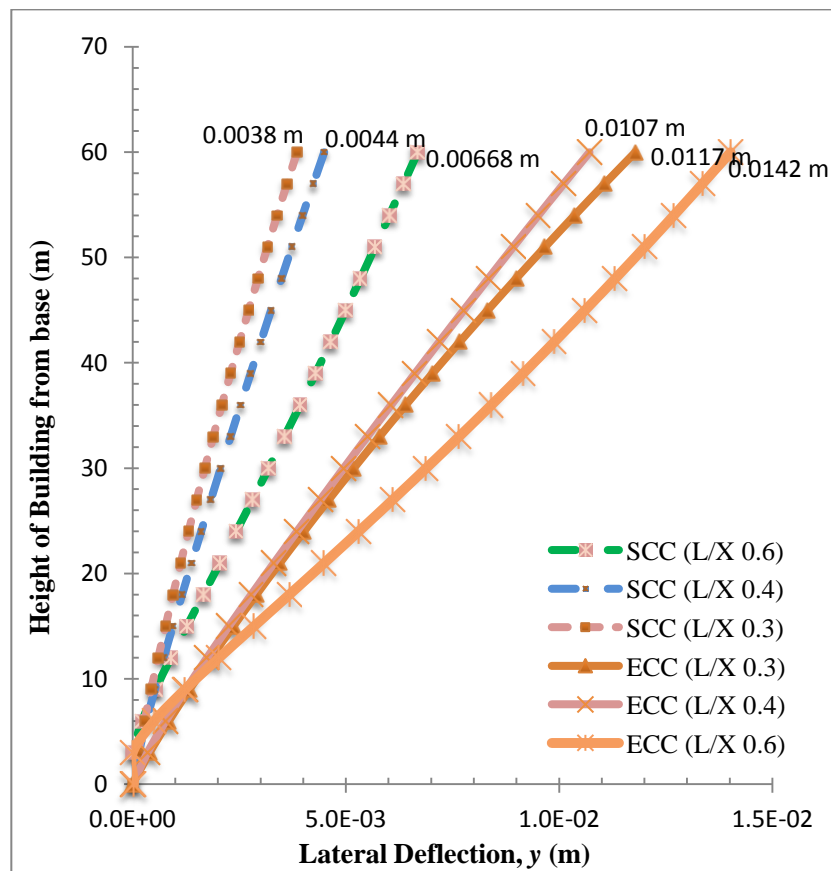


Figure 6.14: Deflection of buildings under calculated design wind load by different L/X

6.4 Chapter Conclusion

This chapter provides an insight into the wind load carrying capacity of ECC and SCC buildings at various stages from cracking to yielding. ECC buildings show much better performance in terms of ductility and strength compared to their SCC counterparts.

CHAPTER 7

CONCLUSIONS

7.0 Introduction

This research is intended to study the non-linear bending/flexural behaviour of slabs in Coupled Shear Wall (CSW) structures through experimental and theoretical investigations. Analysis of CSW system can be performed using existing techniques if the bending stiffness and effective width of coupling slab is known. Small scale CSW models of approximately 1/12th scale made of reinforced High Performance Concrete (HPC) such as Engineered Cementitious Composite (ECC) and Self-Consolidating Concrete (SCC) are tested under monotonic loading. The performance ECC and SCC coupling slabs is compared based on load-deflection/moment-rotation response, stress-strain development in steel/HPC, strength, ductility, cracking characteristics and failure modes. It is expected that the application of ECC (with high strain hardening capacity and capability of forming micro-cracking) will greatly enhance the strength, stiffness and ductility of the CSW system compared to SCC and Normal Concrete (NC).

Bending stiffness and effective width of coupling slabs in pre-cracking, cracking and post-yielding stages are determined from moment-rotation response (from model tests) by applying theoretical equations and compared with previous research studies. Influence of geometric parameters (such as L/X and Y/X) and HPC types on bending stiffness/effective width is critically analyzed and design aids in the form charts for the determination of bending stiffness/effective width are produced. The stress, force distribution, lateral deflection and wind load carrying capacity of full-scale 20-storey ECC/SCC coupled shear wall buildings having varying geometric parameters are analyzed at pre-cracking, cracking and post-yielding stages (simulated by using pre-cracking, cracking and post-yielding effective width determined from current research) by continuous medium method.

7.1 Conclusions

The following conclusions are drawn from this research:

- Literature review reveals that to date, no research has been conducted on the effect of HPC especially ECC on the strength, stiffness and ductility of the CSW system.
- Model tests have proved the basic concept of the existence of point of contra-flexure in the middle of the coupling slabs in shear wall structures illustrating the fact that the test set-up has realistically simulated coupling slab behaviour under lateral load.
- ECC coupling slabs have developed significantly higher tensile/compressive strain compared to its SCC counterparts. All model CSW specimens have failed due to the failure of coupling slabs along a transverse line passing through the interior edge of the shear wall where tension reinforcement is yielded. Failure of the ECC specimens is characterized by the formation large number of very fine micro-cracks compared to one or two major cracks (with large crack width) in SCC specimens.
- Cracking, yielding and ultimate loads are higher for ECC specimens compared to SCC specimens. ECC slabs exhibits 1.89 times more ductility and 2.33 times higher ultimate load compared to their SCC counterparts. The bigger load-displacement/moment-rotation envelops also demonstrates higher energy absorbing capacity of ECC CSW specimens compared to their SCC counterparts.
- Canadian Code (CSA A23.3-04, 2009) has predicted load capacity of SCC coupling slabs reasonably well with a mean ratio of experimental to theoretical/Code predicated load of 1.10. On the other hand, (CSA A23.3-04, 2009) under-predicts load capacity of ECC coupling slabs with a mean ratio of experimental to theoretical/Code predicated load of 2.06.
- Design charts for the calculation of effective widths and bending stiffness of coupling slabs in the pre-cracking, cracking and post-yielding stages as function of geometric parameters are developed. The effective width increases and bending stiffness decreases with the increase of L/X . Both effective width and bending stiffness decrease as the CSW specimens passes through pre-cracking, cracking and post yielding stages.
- In general, ECC coupling slabs have shown higher effective width and bending stiffness in pre-cracking (11% higher), cracking (43% higher) and post-yielding (63% higher) stages

compared with their SCC counterparts. This signifies that reinforced ECC with its superior strain hardening and crack resisting capabilities will provide more resistance against damage propagation in cracking and post-yielding stages.

- Based on analysis of full-scale 20-storey buildings subjected to wind load using continuous medium method:
 - ECC building shows better ductility compared to their SCC counterparts in terms of higher maximum deflection at the top storey level (28% higher in pre-cracking, 23% higher in cracking and 7% higher in post-yielding stage).
 - ECC buildings are found to be 1.5 to 2.4 times stronger (based on wind load required to reach yielding stage) and 2.0 to 3.0 times ductile (based on lateral deflection at yielding) than their SCC counterparts.

This research confirms the viability of constructing reinforced ECC coupled shear wall building with enhanced strength, stiffness and ductility. Use of such shear wall system will be highly effective for high rise buildings located in areas with high seismic risk.

7.2 Recommendations for Future Research

The following recommendations are suggested for further research studies:

- Experimental and numerical investigations on coupled shear wall system with different shapes of shear walls, varying geometrical parameters of building and HPC types (such as ECC and other fiber reinforced concrete) to investigate the behaviour under monotonic, cyclic and impact loading.
- Experimental and numerical investigations on HPC coupled shear wall system with multiple-bay of opening and using coupled beam-slab system under monotonic, cyclic and impact loading.
- Development of Code based specifications for the design of CSW system with HPCs.

REFERENCES

- ASTM Standard A36, (1986). “Steel Construction Manual”, *8th Edition, second revised edition*, American Institute of Steel Construction, ch-1, 1–5.
- ASTM Standard C1017, (2007). “Standard Specification for Chemical Admixtures for Use in Producing Flowing Concrete”. *West Conshohocken, PA., ASTM International*.
- ASTM Standard C109/C109 M (2011). “Standard Test Method for Compressive Strength of Hydraulic Cement Mortars (using 2-in. Or [50mm] cube specimens).” *West Conshohocken, PA., ASTM International*.
- ASTM Standard C494, (2011). “Standard Specification for Chemical Admixtures for Concrete.” *West Conshohocken, PA., ASTM International*.
- CSA Standard A23.3-04, (2009). “Concrete Design Handbook.” *Canadian Portland Cements Association Handbook, 2nd edition. Canada*.
- Barnard, P.R., and Schwaighofer, J. (1967), “The Interaction of Shear Walls Connected Solely Through Slabs.” *Proc., Symposium on the tall Building (University of Southampton, April) Pergamon Press, Oxford, England, 157-180*.
- Bari, M.S., (1987), “Design of Shear Wall Floor Slab Connections using Shear Reinforcement.” *Ph. D. Thesis, University of Glasgow*.
- Bouzoubaâ, N. and Lachemi, M. (2001), “Self-Compacting Concrete Incorporating High Volumes of Class F Fly Ash: Preliminary Results.” *Cement and Concrete Research*, 31(3), 413–420.
- Chitty, L., (1947), “On the Cantilever Composed of a Number of Parallel Beams Interconnected by Cross-bars.” *Philosophical Magazine and Journal of Science (London), Edinburgh and Dublin*, 38(10), 685-699.

- Choudhury, J.R. (1968), “Analysis of Plane and Spatial System of Interconnected Shear Walls.” *Ph. D. Thesis, University of Southampton*.
- Coull, A. and Choudhury, J.R. (1967a). “Stresses and Deflection in Coupled Shear Walls.” *Proc., ACI Journal*, 64(2), 65-72.
- Coull, A. and Choudhury, J.R. (1967b). “Analysis of Coupled Shear Walls.” *Proc., ACI Journal*, 64(9), 587-593.
- Coull, A. and A.W. Irwin (1969). “Design of Connecting Beams in Coupled Shear Wall Structures.” *Proc., ACI Journal*, 66(3), 205-209.
- Coull, A. and El-Hag. A.A. (1975). “Effective Coupling of Shear Walls by Floor Slabs.” *Proc., ACI Journal*, 72(8), 429-431.
- Coull, A. and Wong, Y.C. (1981), “Bending Stiffness of Floor Slabs in Cross-Wall Structure.” *Proc., Institution of Civil Engineering, Part-2*, 71(3), 17-35.
- Coull, A. and Wong, Y.C. (1983). “Design of Floor Slabs Coupling Shear Walls.” *Proc., Journal of Structural Engineering, ASCE*, 109(1), 109-125.
- Coull, A. and Wong, Y.C. (1984). “Coupling Action of Slabs in Hull core Structures.” *Proc., Journal of Structural Engineering, ASCE*, 110(2), 213–227.
- Coull, A. and Wong, Y.C. (1990). “Cracked Coupling Slabs in Shear Wall Buildings.” *Proc., Journal of Structural Engineering, ASCE*, 116(6), 1744-1748.
- Hayakawa, M., Matsuoka, Y. and Shindoh, T. (1993), “Development and Application of super Workable Concrete.” *Proc. of an International RILEM Workshop on special concrete: Workability and Mixing, Paisley, Scotland*, 2(3), 183–190.
- Hossain. K. M. A. (2003). “Non-linear Performance of Slabs in Coupled Shear Wall Structures.” *Advances in Structural Engineering, ASCE*, 6(4), 341-354.

- Hossain, K.M.A. and Lachemi M. (2010), “Fresh, Mechanical, and Durability characteristics of Self-Consolidating Concrete incorporating volcanic ash.” *Journal of Materials in Civil Engineering, ASCE*, 22(7), 651-657.
- Huq, M. M. (1974), “Flexural Stiffness of floor slabs in Shear wall Structures.” *MASc. Thesis, BUET, Dhaka*.
- Khayat, K.H. (1999), “Workability, Testing, and Performance of Self-Consolidating Concrete.” *ACI Materials Journal*, 96(3), 346–353.
- Kunieda, M., and Rokugo, K. (2006), “Recent Progress on HPFRCC in Japan: Required Performance and Applications.” *Journal of Advances in Concrete Technology*, 4(1), 19–33.
- Kojima, S., Sakata, N., Kanda, T. and Hiraishi, T. (2004). “Application of Direct Sprayed ECC for Retrofitting Dam Structure Surface - Application for Mitaka-Dam.” *Concrete Journal*, 42(5), 135-139.
- Kotsovos, M.D., and Newman, J.B. (1977), “Behaviour of Concrete under Multi-axial Stress.” *Proc., ACI Journal*, 74(9), 443-446.
- Kotsovos, M.D., and Newman, J.B. (1979), “A Mathematical Description of the Deformational Behaviour of the Concrete under Complex Loadings.” *Magazine of Concrete Research*, Issue No. 107, 31(6), 77-90.
- Kotsovos, M.D., (1979), “A Mathematical Description of the Strength Properties of Concrete under Generalized stress.” *Magazine of concrete Research*, Issue No. 108, 31(9), 151-158.
- Kotsovos, M.D., (1984), “Concrete. A Brittle Fracturing Material.” *Material and structures, RILEM*, Issue No. 98, 17(3), 107-115.
- Kong, H.J., Bike, S. G. And Li, V. C., (2003). “Development of Self Consolidating Engineered Cementitious Composite Employing Electrostatic Dispersion/Stabilization.” *International Journal of Cement Composite and light weight Concrete*, 25(3), 301-309.

- Lachemi, M., Hossain, K.M.A., Lambros, V. and Bouzoubaâ, N. (2003), “Development of Cost-Effective Self-Consolidating Concrete Incorporating Fly Ash, Slag Cement, or Viscosity-Modifying Admixtures.” *ACI Materials Journal*, 100(5), 419–425.
- Lepech, M., Keoleian, G.A., V.C. Li (2007), “Integrated Structure and Materials Design for Sustainable Concrete Transportation Infrastructure.” *International Society for Industrial Ecology Conference 2007*, Toronto, 17-20.
- Lepech, M. and Li, V. C. (2007a), “Large Scale Processing of Engineered Cementitious Composites.” *Accepted for publication in American Concrete Institute Materials Journal. ACI Materials Journal*, 105(4), 358-366.
- Lepech, M. D., Li, V.C., Robertson, R. E., and Keoleian, G. A. (2007b), “Design of Ductile Engineered Cementitious Composites for Improved Sustainability.” *ACI Material Journal*, 105(6), 567-575.
- Li, V.C. (1993), “From Micromechanics to Structural Engineering: The Design of Cementitious Composites for Civil Engineering Applications.” *Journal of Structural Mechanics and Earthquake Engineering*, 10(2), 37–48.
- Li, V.C. (1997), “Engineered Cementitious Composites - Tailored Composites Through Micromechanical Modeling in Fiber Reinforced concrete: Present and the Future.” *Canadian Society of Civil Engineers*, Montreal, 64-97.
- Li, V. C., Wang, S. and Wu, C. (2001), “Tensile Strain-hardening Behaviour of PVAECC.” *American Concrete Institute Materials Journal*, 98(6), 483-492.
- Li, V. C. (2003), “On Engineered Cementitious Composites (ECC) A Review of the Material and Its Applications.” *Journal of Advanced Concrete Technology*, 1(3), 215-230.
- Li, V. C. and Lepech, M. (2004). “Crack Resistant Concrete Material for Transportation Construction.” *In TRB 83rd Annual Meeting, Washington, D.C., Compendium of Papers CD ROM*, 04-4680.

- Li, V. C. and Yang, E. H. (2007), “Self-Healing In Concrete Materials. In Self-Healing Materials.” *An Alternative Approach to 20 Centuries of Materials Science, Van der Zwaag, Sp. Edition*, New York, 161–193.
- Li, V.C., Lepech, M., Wang, S., Weimann, M., and Keoleian, G., (2004), “Development of Green ECC for Sustainable Infrastructure Systems.” *Proc., International Workshop on Sustainable Development and Concrete Technology*, Beijing, China, 181-192.
- Li, V.C. (2011), “Highly Ductility Concrete for Resilient Infrastructures.” *Journal of Advanced and Highly performance Materials*, winter, University of Michigan, 16-21.
- Lin, Z., Kanda, T. and Li, V. C. (1999), “On Interface Property Characterization and Performance of Fiber Reinforced Cementitious Composites.” *Concrete Science and Engineering*, RILEM, Issue No. 3, 1(9), 173-184.
- Maruta, M., Kanda, T., Nagai, S. and Yamamoto, Y. (2005), “New High-Rise RC Structure Using Pre-Cast ECC Coupling Beam.” *Concrete Journal*, 43(11), 18-26.
- Mavani, M., (2012), “Fresh Mechanical, Durability and Structural Performance of Engineered Cementitious Composite (ECC).” *MASc Thesis, Ryerson University*, 134 p.
- Michael, D. (1969), “Discussion on the Bending Stiffness of the Slabs Connecting Shear Walls.” by A. Qadeer and B. Stafford Smith, *Proc., ACI Journal*, 66(12), 10-21.
- Mitamura, H., Sakata, N., Shakushiro, K., Suda, K. and Hiraishi, T. (2005), “Application of Overlay Reinforcement Method on Steel Deck Utilizing Engineered Cementitious Composites – Mihara Bridge.” *Bridge and Foundation Engineering*, 39(8), 88-91.
- Mirza, M.S., and Lim, A.K.W. (1989), “Behaviour and Design of Coupled Slab Shear Wall System.” *Proc. Canadian Pre-stressed Concrete structures Concrete Conference, CSCE and Canadian Pre-stressed Concrete Association*.
- Nawy, E.G. (2008), “Concrete Construction Engineering Handbook.” 2nd Edition, *Taylor & Francis Group, CRC Press*, 1584 p.

- Paulay, T., and Taylor, R.G. (1981), “Slab Coupling of Earthquake Resisting Shear Walls.” *Proc., ACI Journal*, 78(2), 130-140.
- Qadeer, A., and Smith, B.S. (1969), “The Bending Stiffness of the Slabs Connecting Shear walls.” *Proc., ACI Journal*, 66(6), 464-473.
- Rokugo, K., Kunieda, M. and Lim, S. C. (2005), “Patching repair with ECC on Cracked Concrete Surface.” *Proc. of ConMat*, August, Vancouver, Canada, 22-24.
- Rosman, R., (1964), “Approximate Analysis of Shear Walls Subjected to Lateral Load.” *Proc., ACI Journal*, 61(6), 717-734.
- Şahmaran, M., Lachemi, M., Hossain, K.M.A., and Li, V.C. (2009), “Influence of aggregate type and size on the ductility and mechanical properties of ECC.” *ACI Materials Journal*, 106(3), 308-316.
- Şahmaran, M., Özbay, O., Yüce, H.E., Lachemi, M., and Li, V.C. (2011), “Effect of Fly Ash and PVA Fiber on Micro-structural Damage and Residual Properties of Engineered Cementitious Composites Exposed to High Temperatures.” *Journal of Materials in Civil Engineering*, 23(12), 1735-1745.
- Schwaighofer, J., and Collins, M.P., (1977). “Experimental study of the Behaviour of Reinforced Concrete coupling Slabs.” *Proc., ACI Journal*, 74(3), 123-127.
- Sherir, M. A. A, (2012), “Fracture Energy Fatigue and creep properties of Engineered Cementitious Composites incorporating Fly Ash/Slag with different aggregates.” *MASc Thesis, Ryerson University*, 120 p.
- Subedi, N. K. (1991a). “RC-Coupled Shear Wall Structures I - Analysis of coupling Beams.” *Journal of Structural Engineering*, 117(3), 667-680.
- Subedi, N. K, (1991b). “RC-Coupled Shear Wall Structures II- Ultimate Strength Calculation”, *Journal of Structural Engineering*, 117(3), 681-698.

- TSO, W.K., and Mahmoud, M.A. (1977), “Effective Width of Coupling slabs in Shear Wall Buildings.” *Journal Structure division. ASCE*, 103(3), 573-586.
- Wang, S. and Li, V. C. (2003), “Materials Design of Lightweight PVA-ECC.” *Proc. of the Fourth International RILEM Workshop on High-Performance Fiber-Reinforced Cement Composites (HPFRCC 4)*, Naaman, A. E. and Reinhardt, H. W., Eds., RILEM, Paris, 379 –390.
- Wang, S. and Li, V.C. (2006), “High-Early-Strength Engineered Cementitious Composites.” *ACI Materials Journal*, 103(2), 97-105.
- Weimann, M.B. and Li, V. C. (2003). “Hygral Behaviour of Engineered Cementitious Composites (ECC).” *International Journal for Restoration of Buildings and Monuments*, 9(5), 513-534.
- Yang, Y., Lepech, M., and Li, V. C. (2005), “Self-Healing of Engineered Cementitious Composites under Cyclic Wetting and Drying.” *Proc. of The International Workshop on The Durability of Reinforced Concrete under Combined Mechanical and Climatic Loads (CMCL)*, Qingdao, China, October, 231–242.